



The ALCHEMI Atlas: Principal Component Analysis Reveals Starburst Evolution in NGC 253

Nanase Harada^{1,2,3}, David S. Meier^{4,5}, Sergio Martín^{6,7}, Sébastien Muller⁸, Kazushi Sakamoto², Toshiki Saito¹, Mark D. Gorski^{8,9}, Christian Henkel^{10,11}, Kunihiko Tanaka¹², Jeffrey G. Mangum¹³, Susanne Aalto¹⁴, Rebeca Aladro¹⁰, Mathilde Bouvier¹⁵, Laura Colzi¹⁶, Kimberly L. Emig^{13,23}, Rubén Herrero-Illana^{6,17}, Ko-Yun Huang¹⁵, Kotaro Kohno¹⁸, Sabine König⁸, Kouichiro Nakanishi^{1,3}, Yuri Nishimura^{18,19,20}, Shuro Takano²¹, Víctor M. Rivilla¹⁶, Serena Viti¹⁵, Yoshimasa Watanabe²², Paul P. van der Werf¹⁵, and Yuki Nishimura¹⁸

¹ National Astronomical Observatory of Japan, 2-21-1 Osawa, Mitaka, Tokyo 181-8588, Japan
² Institute of Astronomy and Astrophysics, Academia Sinica, 11F of AS/NTU Astronomy-Mathematics Building, No.1, Sec. 4, Roosevelt Road, Taipei 10617, Taiwan

³ Astronomical Science Program, Graduate Institute for Advanced Studies, SOKENDAI, 2-21-1 Osawa, Mitaka, Tokyo 181-1855, Japan

⁴ New Mexico Institute of Mining and Technology, 801 Leroy Place, Socorro, NM 87801, USA

⁵ National Radio Astronomy Observatory, P.O. Box O, 1003 Lopezville Road, Socorro, NM 87801, USA

⁶ European Southern Observatory, Alonso de Córdoba, 3107, Vitacura, Santiago 763-0355, Chile

⁷ Joint ALMA Observatory, Alonso de Córdova, 3107, Vitacura, Santiago 763-0355, Chile

⁸ Department of Space, Earth and Environment, Chalmers University of Technology, Onsala Space Observatory, SE-439 92 Onsala, Sweden

⁹ Center for Interdisciplinary Exploration and Research in Astrophysics (CIERA) and Department of Physics and Astronomy, Northwestern University, Evanston, IL 60208, USA

¹⁰ Max-Planck-Institut für Radioastronomie, Auf dem Hügel 69, D-53121 Bonn, Germany

¹¹ Astronomy Department, Faculty of Science, King Abdulaziz University, P. O. Box 80203, Jeddah 21589, Saudi Arabia

¹² Department of Physics, Faculty of Science and Technology, Keio University, 3-14-1 Hiyoshi, Yokohama, Kanagawa 223-8522, Japan

¹³ National Radio Astronomy Observatory, 520 Edgemont Road, Charlottesville, VA 22903-2475, USA

¹⁴ Department of Space, Earth and Environment, Chalmers University of Technology, SE-412 96 Göteborg, Sweden

¹⁵ Leiden Observatory, Leiden University, P.O. Box 9513, 2300 RA Leiden, The Netherlands

¹⁶ Centro de Astrobiología (CAB), CSIC-INTA, Ctra. de Ajalvir Km. 4, Torrejón de Ardoz, E-28850 Madrid, Spain

¹⁷ Institute of Space Sciences (ICE, CSIC), Campus UAB, Carrer de Magrans, E-08193 Barcelona, Spain

¹⁸ Institute of Astronomy, Graduate School of Science, The University of Tokyo, 2-21-1 Osawa, Mitaka, Tokyo 181-0015, Japan

¹⁹ Department of Astronomy, The University of Tokyo, 7-3-1 Hongo, Bunkyo-ku, Tokyo 113-0033, Japan

²⁰ ALMA Project, National Astronomical Observatory of Japan, 2-21-1, Osawa, Mitaka, Tokyo 181-8588, Japan

²¹ Department of Physics, General Studies, College of Engineering, Nihon University, Tamura-machi, Koriyama, Fukushima 963-8642, Japan

²² Materials Science and Engineering, College of Engineering, Shibaura Institute of Technology, 3-7-5 Toyosu, Koto-ku, Tokyo 135-8548, Japan

Received 2023 October 3; revised 2023 December 7; accepted 2023 December 9; published 2024 March 15

Abstract

Molecular lines are powerful diagnostics of the physical and chemical properties of the interstellar medium (ISM). These ISM properties, which affect future star formation, are expected to differ in starburst galaxies from those of more quiescent galaxies. We investigate the ISM properties in the central molecular zone of the nearby starburst galaxy NGC 253 using the ultrawide millimeter spectral scan survey from the Atacama Large Millimeter/submillimeter Array Large Program ALCHEMI. We present an atlas of velocity-integrated images at a 1.⁶ resolution of 148 unblended transitions from 44 species, including the first extragalactic detection of HCNH⁺ and the first interferometric images of C₃H⁺, NO, and HCS⁺. We conduct a principal component analysis (PCA) on these images to extract correlated chemical species and to identify key groups of diagnostic transitions. To the best of our knowledge, our data set is currently the largest astronomical set of molecular lines to which PCA has been applied. The PCA can categorize transitions coming from different physical components in NGC 253 such as (i) young starburst tracers characterized by high-excitation transitions of HC₃N and complex organic molecules versus tracers of on-going star formation (radio recombination lines) and high-excitation transitions of CCH and CN tracing photodissociation regions, (ii) tracers of cloud-collision-induced shocks (low-excitation transitions of CH₃OH, HNCO, HOCO⁺, and OCS) versus shocks from star formation-induced outflows (high-excitation transitions of SiO), as well as (iii) outflows showing emission from HOC⁺, CCH, H₃O⁺, CO isotopologues, HCN, HCO⁺, CS, and CN. Our findings show these intensities vary with galactic dynamics, star formation activities, and stellar feedback.

Unified Astronomy Thesaurus concepts: Astrochemistry (75); Starburst galaxies (1570); Interstellar medium (847); Interstellar molecules (849)

1. Introduction

The physical properties of molecular gas determine where and how future stars will form. A powerful way to investigate the gas properties is via the study of molecular line emission; the physical properties and processes taking place during star formation affect rates of various chemical reactions and thus leave an imprint on the chemical properties of molecular clouds, star-forming regions, and protoplanetary systems.

²³ Jansky Fellow of the National Radio Astronomy Observatory.

Original content from this work may be used under the terms of the [Creative Commons Attribution 4.0 licence](#). Any further distribution of this work must maintain attribution to the author(s) and the title of the work, journal citation and DOI.

While the Milky Way provides a good example of a galaxy with a relatively quiescent star formation activity, it is of great interest to extend molecular inventories to extragalactic sources and to probe the effects of extreme starbursts and active galactic nuclei (AGNs), which cannot be studied in our Galaxy due to the absence of such extreme activities (Meier & Turner 2005; Martín et al. 2006, 2011; Aladro et al. 2015; Nakajima et al. 2018; Takano et al. 2019). The Atacama Large Millimeter/submillimeter Array (ALMA) has enabled high-angular-resolution astrochemical observations targeting regions with extreme activity in the AGN-host NGC 1068 (Takano et al. 2014) and NGC 1097 (Martín et al. 2015), the starburst galaxies NGC 253 (Meier et al. 2015) and M83 (Harada et al. 2019), AGN-starburst composite NGC 4945 (Henkel et al. 2018; Bellocchi et al. 2023), and the ultra/luminous infrared galaxies (U/LIRGs) NGC 4418 (Costagliola et al. 2015), NGC 3256 (Harada et al. 2018), and Arp 220 (Sakamoto et al. 2021).²⁴

Previous observations found that the center of NGC 253 is particularly chemically rich (e.g., Martín et al. 2006, 2021; Aladro et al. 2015; Meier et al. 2015; Ando et al. 2017). It is a barred spiral galaxy at a distance of 3.5 Mpc (Rekola et al. 2005). It hosts $\sim 2 M_{\odot} \text{ yr}^{-1}$ of star formation within the central molecular zone (CMZ) extending to several hundred parsecs in size (Bendo et al. 2015; Leroy et al. 2015). The CMZ of NGC 253 is rich in molecular gas (Sakamoto et al. 2011; Leroy et al. 2015, 2018). It also hosts outflows launched from the energetic starburst (Turner 1985; Bolatto et al. 2013; Walter et al. 2017; Krieger et al. 2019; Levy et al. 2021).

To investigate further the physical and chemical properties of the CMZ in NGC 253, and build upon its molecular richness, we conducted wide-frequency coverage observations as an ALMA large program: ALMA Comprehensive High-resolution Extragalactic Molecular Inventory (ALCHEMI; Martín et al. 2021, hereafter MMH21). Thanks to ALCHEMI, a strong influence of cosmic rays has been found by Holdship et al. (2021) from the CCH fractional abundance, by Harada et al. (2021) from the HOC^+ fractional abundance and $\text{HCO}^+/\text{HOC}^+$ abundance ratio, by Holdship et al. (2022) using the $\text{H}_3\text{O}^+/\text{SO}$ ratio, and by Behrens et al. (2022) to explain the low HCN/HNC ratio even in high-temperature regions. Further findings from ALCHEMI show evidence for strong photodissociation regions (PDRs) in the star-forming regions (Harada et al. 2021), as well as the presence of shocks at the orbital intersections by Humire et al. (2022) from Class I methanol masers, by Harada et al. (2022) from HOCO^+ , and by Huang et al. (2023) with HNCO and SiO . This survey also made the first extragalactic detection of a phosphorus-bearing molecule, phosphorus nitride (Haasler et al. 2022). Tanaka et al. (2024) make use of the multitransition and multimolecule data to accurately map the physical conditions (gas densities, temperatures, and molecular column densities) using hierarchical Bayesian analysis and found high densities compared to those in the center of our own Galaxy.

In addition to the chemical richness, chemical differentiation (i.e., variation of chemistry) within galactic centers provides useful information. Such chemical differentiation illuminates the changing physical conditions, variations in dynamics, energetics, and evolution of the interstellar medium (ISM). Correlations between the chemistries and these conditions

establish their relationships. Such data of spatially resolved chemistry tend to have very large data sets. For their interpretation, statistical methods such as principal component analysis (PCA) are useful in reducing the data size into a handful of components that still retain most of the information. PCA has been used widely in astronomical studies including the interpretation of molecular line intensities from multiple species, although they are relatively limited in terms of the number of transitions observed and included in their analysis (e.g., Ungerechts et al. 1997; Meier & Turner 2005; Costagliola et al. 2011, 2015; Gratier et al. 2017; Saito et al. 2022; Gorski et al. 2023).

In this paper, we conduct a PCA on the ALCHEMI data to derive dominant components within the plethora of lines detectable in the ISM of NGC 253. We aim to find a set of molecular transitions that trace physical conditions such as column densities, excitation conditions, star formation activities, and shocks through this analysis. To the best of our knowledge, this is currently the largest collection of molecular lines in a given astrophysical object to which PCA has been applied. The data set is also characterized by a high degree of homogeneity, in terms of observations and calibration procedures, angular and velocity resolutions, and sensitivity, all of which make the ALCHEMI data set a perfect statistical sample to run PCA. This type of analysis allows for a comprehensive understanding of the ALCHEMI data set while previous ALCHEMI papers mostly focused on a few particular species.

This paper is organized as follows. In Section 2, we describe the observations, line identification, and data products. In Section 3, we report features in the velocity-integrated images. The results of PCA are discussed in Section 4. The implications of results are discussed in Section 5. Section 6 summarizes the main outcome of the work.

2. Observations and Data Products

The ALCHEMI survey (project codes: 2017.1.00161.L, 2018.1.00162.S) includes all the ALMA Bands 3–7 frequency coverage (84–375 GHz; $\lambda = 3.6\text{--}0.8 \text{ mm}$) except for the small spectral regions affected by telluric absorption lines. The observed area extends over $50'' \times 20''$ ($830 \times 330 \text{ pc}^2$ on the sky), which covers most of the CMZ. The data products are convolved into a common $1''.6$ beam ($=27 \text{ pc}$), and the maximum recoverable scale is equal to or greater than $15''$. The rms noise levels for a 10 km s^{-1} channel are $\sim 20 \text{ mK}$, but the exact values for each spectral window can be found in MMH21 where a complete description of this survey, as well as the details on calibration and imaging, is provided.

2.1. Line Identification

In order to identify spectral transitions in the data set, we extracted the spectra from a single pixel at position $\alpha_{J2000} = 0^{\text{h}}47^{\text{m}}33\rlap{.}^s33$, $\delta_{J2000} = -25^{\circ}17'15\rlap{.}''73$. This corresponds to GMC 6 in Leroy et al. (2015; see Figure 1 for the location) and is the position with the brightest molecular emission of most detected species (Haasler et al. 2022). This position has the most complex emission spectra and therefore is used as the reference position for the purposes of line-blending evaluation. Line identification was done by fitting simulated spectra under the assumption of local thermodynamic equilibrium (LTE) from all the commonly observed species, based

²⁴ See Table 1 of Martín et al. (2021) for the references of extragalactic spectral line scan studies.

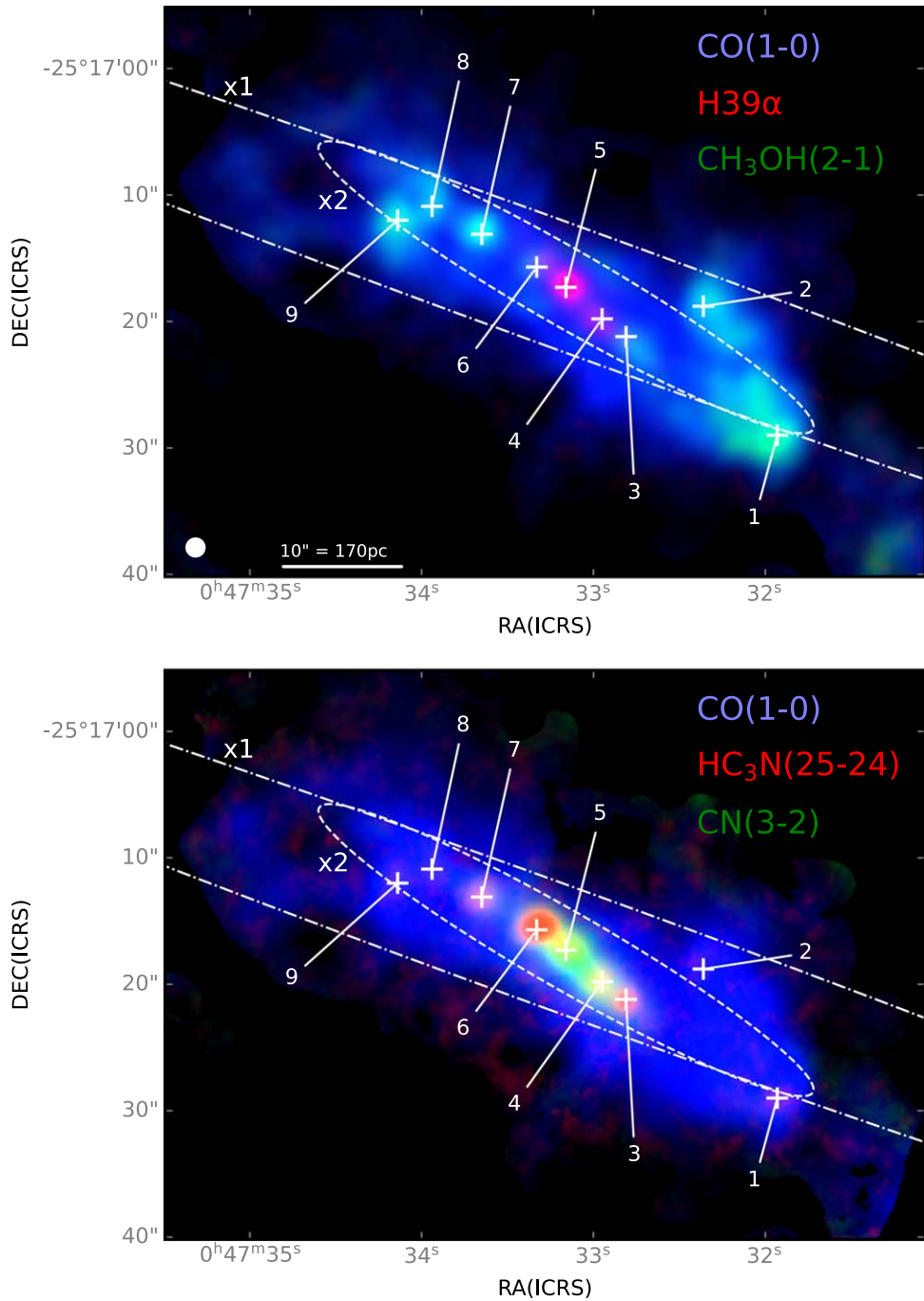


Figure 1. Top: Velocity-integrated images of CO(1-0) in blue, H39 α in red, and CH₃OH(2-1) in green around the rest frequency of 96.7 GHz in green. Rough positions of parts of the x_1 orbits and the full x_2 orbits farther inside are shown with dashed-dotted and dashed lines, respectively. Note that these are just some examples of the presumably large families of possible x_1 and x_2 orbits. There likely exists another x_2 orbit connecting GMCs 3–6 or 3–7 (see Levy et al. 2022) almost fully edge-on. The synthetic beam size is shown at the left bottom corner as a white circle. Bottom: The same as the top panel, but with HC₃N(25–24) in red, and CN(3–2) in green. Intensities are scaled so that faint lines have similar dynamic ranges as other lines. We employed the algorithm by Lupton et al. (2004) to produce RGB images.

on previous extragalactic and Galactic surveys, using MAD-CUBA²⁵ (Martín et al. 2019). The model on which this line identification is based includes a total of 330 entries, including the most common rare isotopologues (¹³C, ¹⁸O, ¹⁷O, ¹⁵N, ³⁴S, ³³S, ³⁶S, ²⁹Si, ³⁰Si, ³⁷Cl), vibrationally excited modes for relevant species, as well as hydrogen and helium recombination lines. In total, 134 species are detected. A line identification

using the resolution of the Atacama Compact Array was already presented by MMH21, but a full presentation of the line identification including the 12 m array and new detections in the extragalactic ISM will be provided in dedicated papers.

2.2. Velocity-integrated Images

From the list of all transitions included in the modeled spectra used for the line identification, we produced velocity-integrated images of isolated lines. A transition is considered isolated if it meets one of the following two criteria. (1) A line

²⁵ Madrid Data Cube Analysis on ImageJ, a software program developed at the Center of Astrobiology in Madrid; <https://cab.inta-csic.es/madcuba/>.

has less than 10% contamination compared with its intensity in fitted models assuming LTE. (2) A line has its line center separated by more than 210 km s^{-1} , 3 times the maximum line width, from other detected lines close in frequency. This level of contamination is negligible considering the $\sim 15\%$ calibration uncertainty (MMH21). We also considered a transition as isolated if blended by the same molecule (e.g., CCH, CH_3CCH , CN), but used masks to include all the transitions as we describe in the next paragraph (see Appendix A for the list of transitions). Our criterion for detection was having $>3\sigma_{\text{ch}}$ intensity at their peak, where σ_{ch} is the rms value of a single channel. Our line identification was done at the most molecule-rich position, and the contamination is likely less than 10% in other positions. We also eliminated the lines with heavy contamination from unidentified lines through the visual inspection of spectra. Spectroscopic information that is used in this paper is listed in Appendix B. We note that these criteria for isolated lines may be too strict in some cases, and some transitions not included in this study may contain only very little contamination. It is the reason this study omits some transitions used in prior ALCHEMI papers, in which the individual transitions were more thoroughly checked for contamination.

To create velocity-integrated (moment 0) images, we applied a 3D mask created from a reference transition with threshold cutoffs to a cube of each isolated transition. It is to exclude contamination from other transitions close in frequency in a similar way as in Harada et al. (2021). We choose a reference transition with strong emission and determine the threshold cutoff based on the reference transition, then apply this cutoff to cubes of other transitions. We use the $^{12}\text{CO}(J=1-0)$ image cube as a reference image to create masks for transitions that are not ^{12}CO but have relatively strong emission (HCN, HCO^+ , HNC, CS, CCH, and CN). For other species, we used HCN ($J=1-0$) as a reference transition. The ^{12}CO transitions have the highest signal-to-noise ratio (S/N) in our data set, and emission is detected in larger volumes of their cubes than for any other line. Therefore, a ^{12}CO mask is suitable for collecting weak extended emission in transitions such as HCN. On the other hand, the HCN($1-0$) mask is more suitable for weak lines to eliminate contamination from neighbors, because there is one location (GMC 6) where the CO line is very broad.

To create the binary 0/1 masks, we first convolved the reference cubes to a lower angular resolution of $3''.2$ to capture faint extended emission in the masks. We then set the mask value to 1 only at locations in the cubes with a $>15\sigma_{\text{ch}}$ detection for the CO($1-0$) mask or $>5\sigma_{\text{ch}}$ detection for the HCN($1-0$) mask, where σ_{ch} is the single-channel rms value in the $3''.2$ resolution reference cube. A $1''.6$ resolution integrated-intensity map is created as the input line cube multiplied by the mask cube on the same grid and integrated over velocity. The above cutoffs for the masks may seem unnecessarily high, but these masks should still include all regions with significant emission, because all the transitions except those of ^{12}CO are more than 10 times weaker than CO($1-0$) in extended regions, and HCN($1-0$) has more than 3 times higher S/N compared to the transitions to which the HCN mask was applied. We confirmed that our masking did not exclude the target emission by visually inspecting the original and masked cubes. This high cutoff for CO($1-0$) also helps to exclude nitrogen sulfide (NS) transitions at the rest frequency $f_{\text{rest}} = 115.154 \text{ GHz}$ near CO($1-0$), whose rest frequency is at 115.271 GHz . We applied

Table 1
GMC Positions and Their Properties

GMC	R.A. (ICRS) ^a $0^{\text{h}}47^{\text{m}}$	Decl. (ICRS) $-25^{\circ}17'$	Remarks
1	$31^{\circ}93$	$29.^{\prime}0$	Class I methanol maser ^b
2	$32^{\circ}36$	$18.^{\prime}8$	Class I methanol maser ^b
3	$32^{\circ}81$	$21.^{\prime}2$	Clumps 1–3 ^c
4	$32^{\circ}95$	$19.^{\prime}8$	Clumps 4–7 ^c
5	$33^{\circ}16$	$17.^{\prime}3$	Clumps 8–13 ^c
6	$33^{\circ}33$	$15.^{\prime}7$	Clump 14 ^c
			Line ID position ^d
7	$33^{\circ}65$	$13.^{\prime}1$	Class I methanol maser ^b
8	$33^{\circ}94$	$10.^{\prime}9$	Class I methanol maser ^b
9	$34^{\circ}14$	$12.^{\prime}0$	Class I methanol maser ^b

Notes.

^a The International Celestial Reference System.

^b Humire et al. (2022).

^c Leroy et al. (2018).

^d Position of the brightest molecular emission.

our masked integration to images within 400 km s^{-1} from the systemic velocity of 258 km s^{-1} . The effective range of integration is narrower than 800 km s^{-1} because of the masking.

For ^{12}CO transitions, we created the masks from themselves (e.g., using CO 3–2 as the reference cube for CO 3–2). We again convolved the reference cubes to $3''.2$, twice the original beam size, and kept the positions with emission brighter than $2\sigma_{\text{ch}}$. These masks were applied to the original $1''.6$ resolution cubes.

For the transitions blended with the same species (e.g., CCH), we first made cubes with their velocity coordinates defined from one of the transitions (a velocity reference line), with enough width to cover all the detectable transitions of interest. Then, we created masks to include emissions from multiple transitions from the same species, using the known velocity shifts from the velocity reference line. The list of such transitions can be found in Appendix A.

In addition to the 3D masking applied above, we also applied a threshold cutoff of 3σ to the integrated-intensity images. The rms σ of the integrated intensities is estimated as

$$\sigma = \sigma_{\text{ch}} \Delta v \sqrt{N}, \quad (1)$$

where σ_{ch} is the rms for one channel in the cube, Δv is the channel width (10 km s^{-1}), and N is the number of channels used for integration.

After removing the transitions with peak intensities less than 10 K km s^{-1} and Band 5 transitions with channels affected by severe artifacts (SiO 4–3, N_2H^+ 2–1; see also Section 3), we use 148 transitions of molecules or radio recombination lines (RRLs) from 44 species and two continuum images (one representative of synchrotron/free-free emission at the lower frequency range and the other representative of dust thermal emission at the higher frequency range) for PCA. The velocity-integrated images, original cubes, and masked cubes will be made public as a part of the high level data products to be made available through the ALMA science archive for large programs.²⁶ In addition, a matrix of standardized intensities is also publicly available at doi:[10.5281/zenodo.1040838](https://zenodo.1040838).

²⁶ <https://almascience.nao.ac.jp/alma-data/lp>

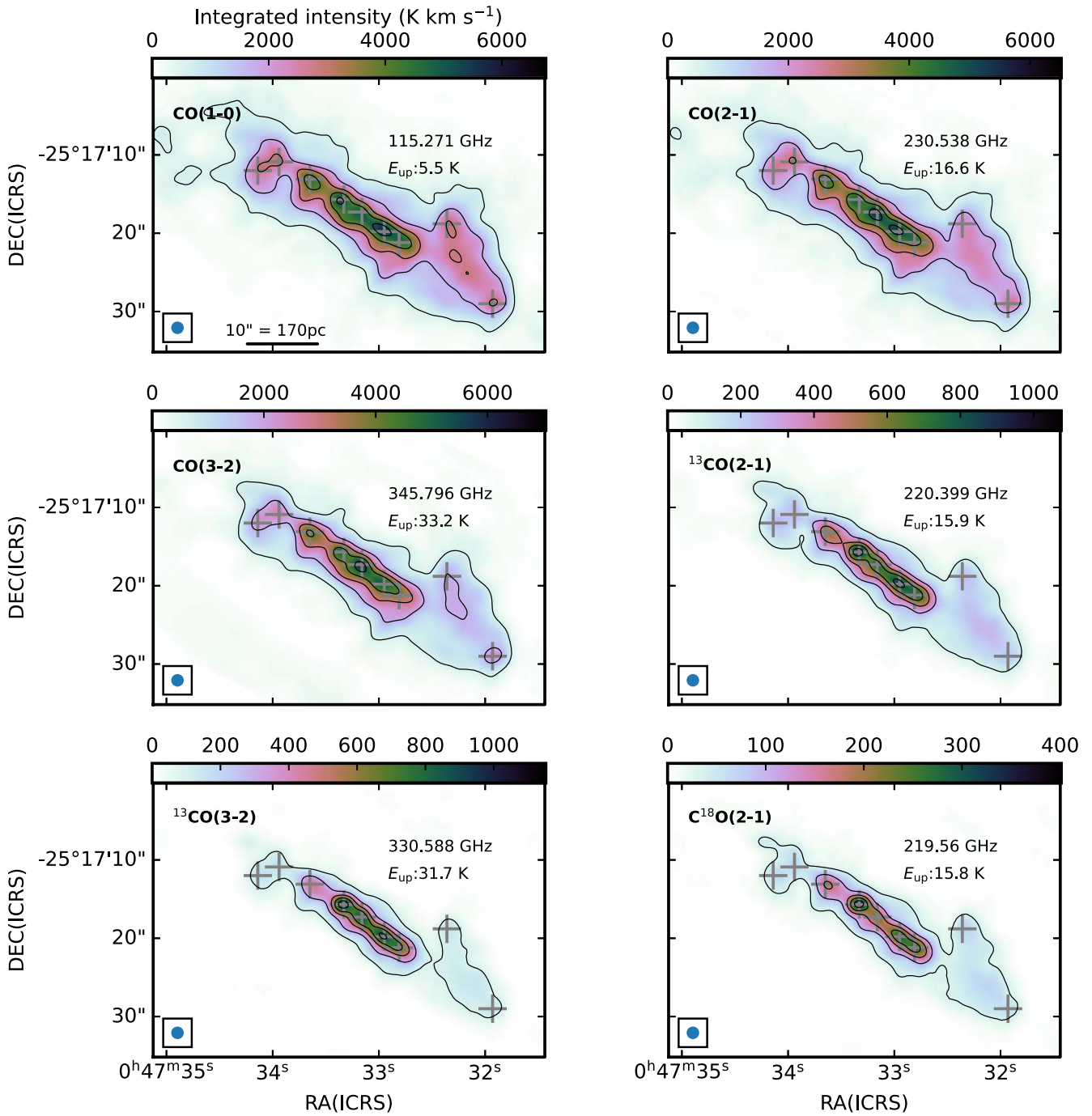
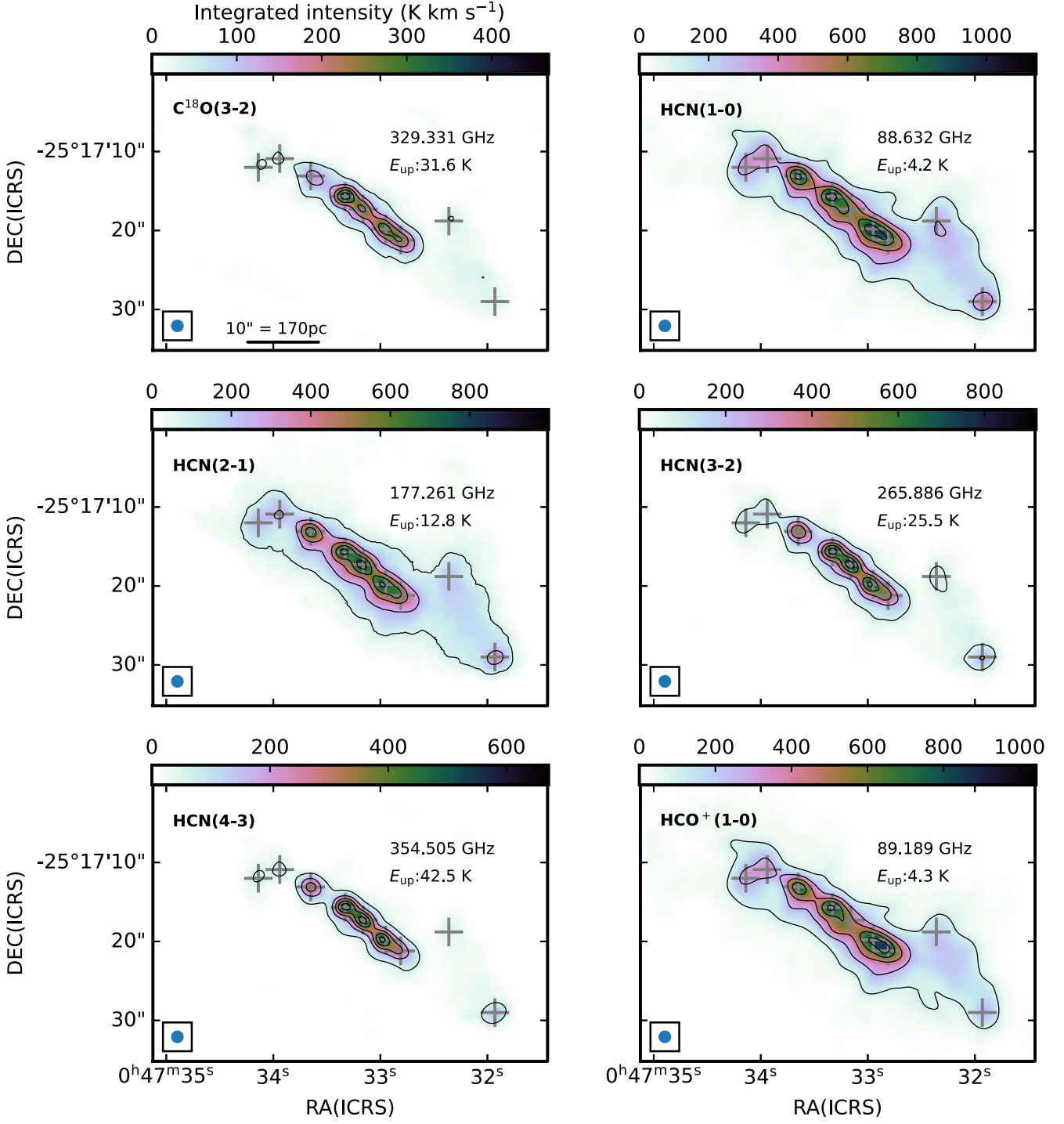


Figure 2. Velocity-integrated images integrated from within 400 km s^{-1} of the systemic velocity with masking as described in Section 2.1. Contour levels are set at 10%, 30%, 50%, 70%, and 90% of their peak values. Maximum values of color scales are set for 120% of their peak values. We show more commonly observed species first, and transitions are in ascending order of frequency within the same species. The transition names are in the upper left corner, and the line rest frequency and the energy level in the upper state are also in each panel. The $1''.6$ beam is in the bottom left corner. The plus signs indicate GMC locations. The images are corrected for the primary beam response patterns of the ALMA antennas.

3. Distribution of Transition Intensities

We first describe locations in the CMZ of NGC 253 using the two color-composite (red, green, and blue; RGB) images of selected transitions in Figure 1. They show the contrast between images of CO(1-0), H39 α , CH₃OH(2 K -1 K), HC₃N(25-24), and CN(3-2). This choice of lines for the RGB channels is justified by the results of the PCA, from which we select these five representative lines as highlighting the extreme variance in the data set, hence giving the RGB

images a high contrast. As we discuss later in Section 4.3, these transitions represent the first three principal components (PC1, positive and negative PC2, positive and negative PC3). In this figure, we show the positions of giant molecular clouds (GMCs) that we refer to throughout the paper. They are close to the GMCs discussed in Leroy et al. (2015), but slightly modified to better match the molecular emission peaks in most species. Because the GMC peaks are hard to pinpoint from bright, ubiquitous, and extended transitions such as CO and

**Figure 3.** Same as Figure 2.

HCN, we identified the peaks from species that trace more specific locations such as SiO (GMCs 1, 7, 8, and 9), HC₃N(GMCs 3, 4, 6), and H39 α (GMC 5). These positions are listed in Table 1.

Some of these clouds reside at orbital intersections of bar orbits (the x_1 orbits) and central orbits (the x_2 orbits) resulting from the stellar bar potential in NGC 253 (Sorai et al. 2000; Das et al. 2001). The gas on the bar orbits flows in from the northeast and southwest directions. GMCs 1, 2, 7, 8, and 9 have signs of shocks detected from Class I methanol masers (Humire et al. 2022). Other clouds are locations of young

massive star-cluster formation. An RRL, H40 α , has been detected in GMCs 3–6 (Bendo et al. 2015; Mills et al. 2021). We note that the RRL in GMC 3 is not obvious in our $1''.6$ beam. Only high-angular-resolution observations ($\sim 0''.2$) by Mills et al. (2021) found weaker and narrower H40 α in GMC 3 compared with GMCs 4–6.

Figures 2–22 show the integrated-intensity images created using the procedure described in the previous section. Continuum images at 95 GHz (3.2 mm) and 361.5 GHz (0.83 mm) are also included in the last two panels of Figure 22. As already illustrated by Meier et al. (2015),

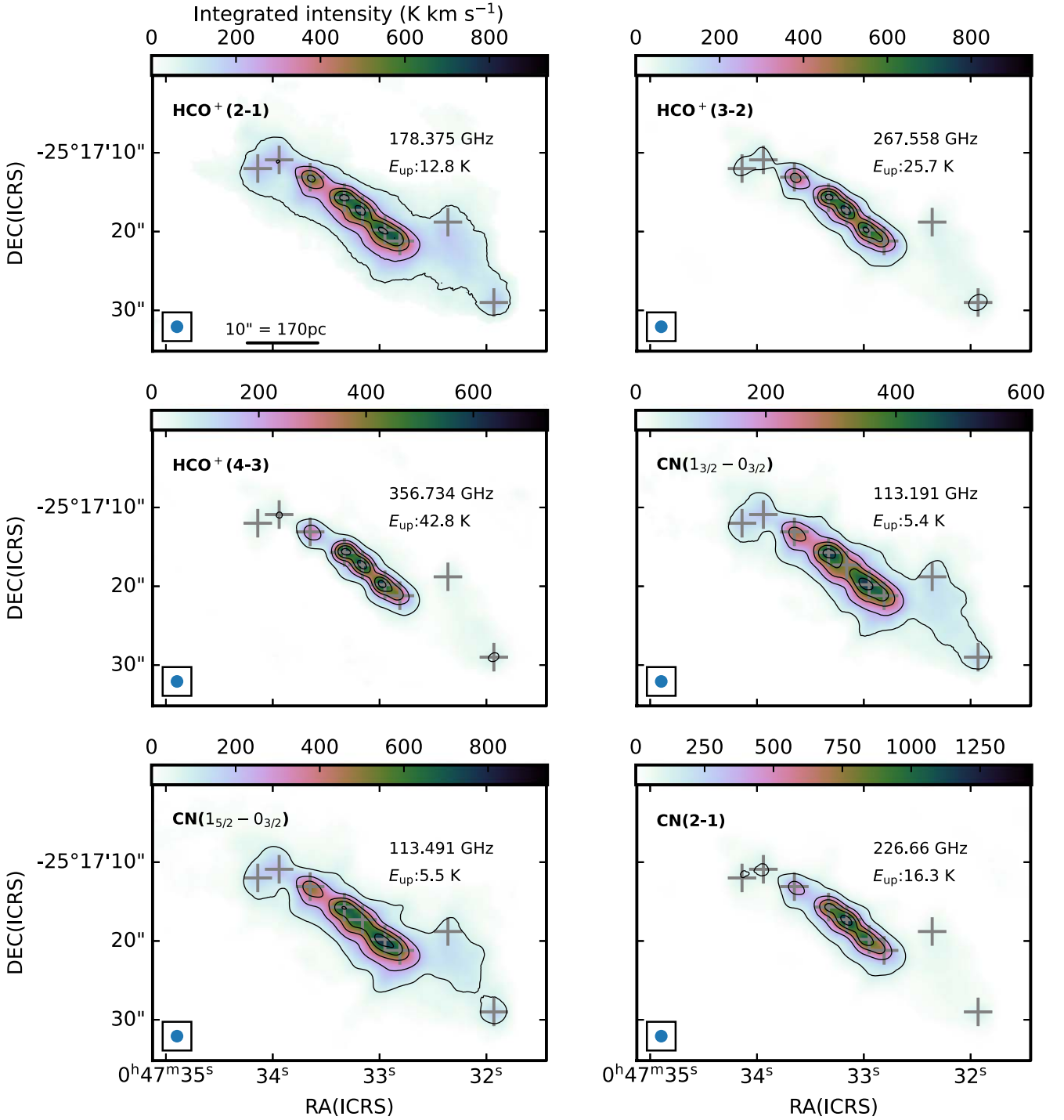


Figure 4. Same as Figure 2.

morphological differences are obvious from simple visual inspection. While distributions of some transitions are more extended, some are more concentrated around the central parts, and others are enhanced in the outskirts of the CMZ (GMCs 1, 2, 8, and 9) in NGC 253.

In general, CO isotopologues (¹²C¹⁶O, ¹³C¹⁶O, ¹²C¹⁸O, and ¹²C¹⁷O, hereafter ¹²CO, ¹³CO, C¹⁸O, and C¹⁷O) exhibit more extended emission than other species. Higher-*J* transitions are slightly more compact than *J* = 1–0 transitions, likely because the gas is more excited near active star-forming regions. The rarer isotopologues of CO show more compact emission than

the main isotopologue (¹²C¹⁶O) both due to the lower optical depths and lower S/N.

The transitions of species with high critical densities ($n_{\text{crit}} > 10^4 \text{ cm}^{-3}$ in optically thin cases) such as HCN, HCO⁺, CS, N₂H⁺, and CCH also show significantly extended emission in their *J* = 1–0 transition, but the higher-*J* transitions are more compact, some of which have already been shown in our previous literature (Harada et al. 2021; Holdship et al. 2021; Behrens et al. 2022). We see this trend in CO isotopologues as well, but it is more prominent in these transitions with high critical densities. Similar to CO

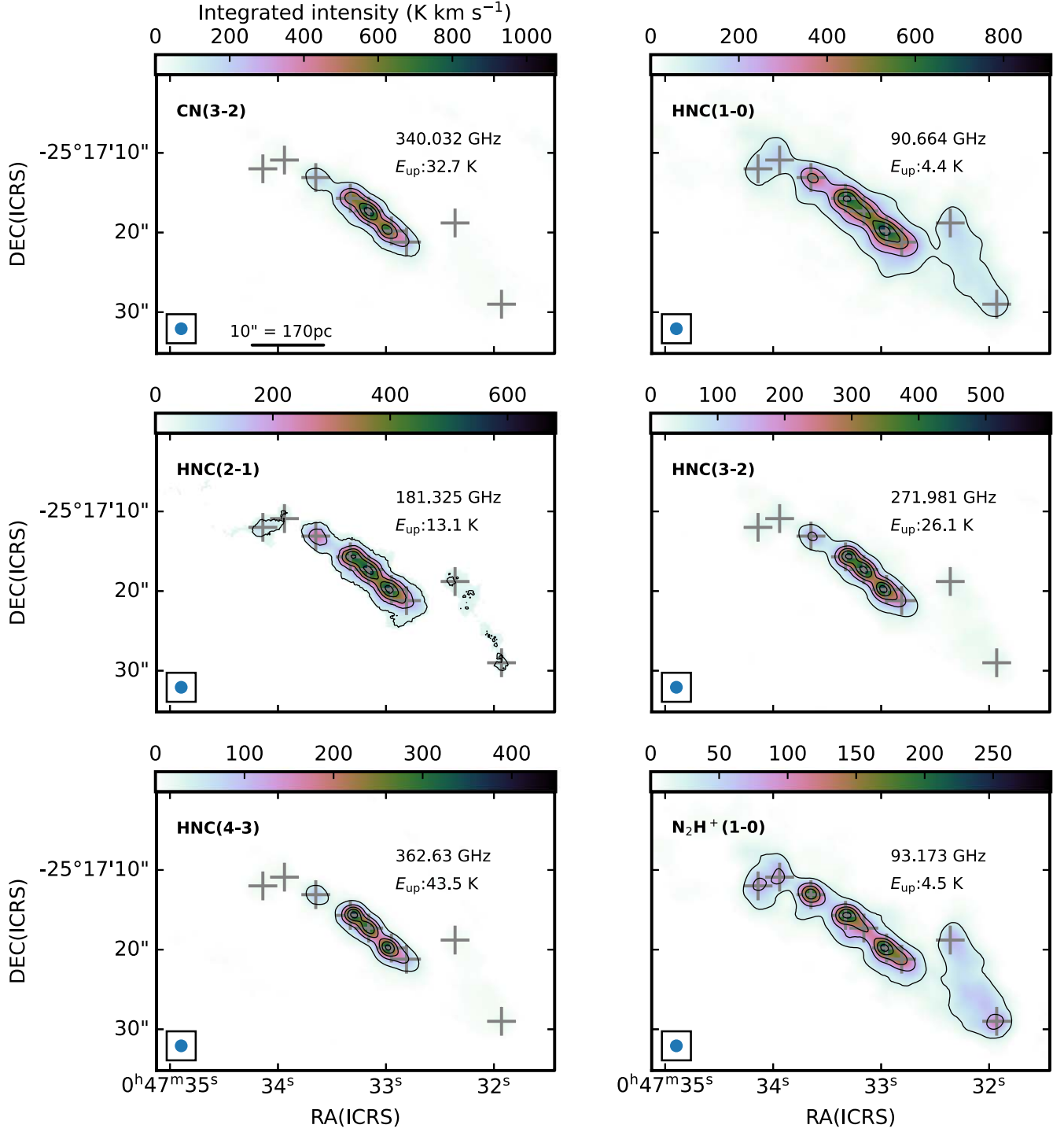


Figure 5. Same as Figure 2.

isotopologues, the emission from rarer isotopologues of other molecules is more compact than from their main counterparts.²⁷

²⁷ Sakamoto et al. (2021) reported similar size variations among various sub/mm emissions from their ALMA imaging spectral scans toward the nuclei of luminous infrared galaxies NGC 4418 and Arp 220. Taken together, these observations caution against the assumption of a common beam-filling factor in the excitation analysis of molecular lines for unresolved galactic nuclei.

We find somewhat compact distributions in the 3 mm continuum emission, most of which should originate from free-free emission, and RRLs compared with other transitions mentioned above. They are expected to arise from the ionized gas, tracing the ongoing star formation (e.g., Bendo et al. 2015). These types of emission and transitions such as HCN, HCO^+ , CCH, and CN with higher upper-state energies emit strongly in similar locations (see also Holdship et al. 2021, for CCH).

On the other hand, CH_3OH , HNCO, and HOCO^+ transitions with low upper-state energies are enhanced in the outskirts of

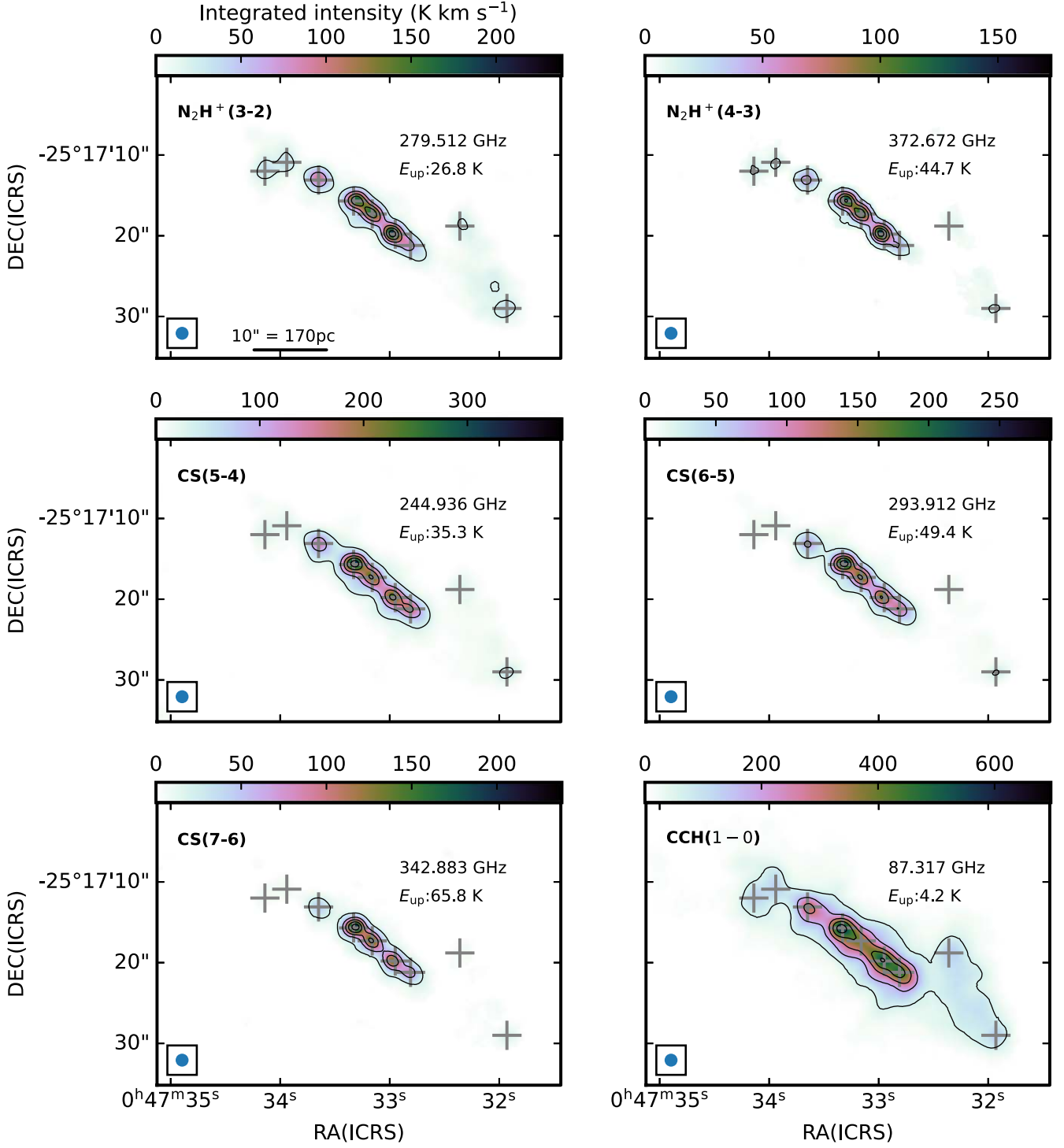


Figure 6. Same as Figure 2.

the NGC 253 CMZ (Figures 11–15). Out of these species, CH₃OH and HNCO are known as tracers of slow shocks,²⁸ and their enhancements are likely attributed to widespread shocks in those regions (Meier et al. 2015; Huang et al. 2023). Harada et al. (2022) argued that HOCO⁺ should be tracing shock-evaporated CO₂, and its relation with shocks is suggested by

²⁸ Fast shocks could enhance methanol as well according to some modeling results, although there is also an observational result that suggests methanol destruction in fast shocks (Suutarinen et al. 2014).

the similarity with these species. A tracer of fast shocks, SiO, also shows some emission at the outskirts of the CMZ. Unlike weaker shock tracers, SiO transitions emit strongly near the starburst regions as well (Figures 10–11).

To the best of our knowledge, we also present the first extragalactic detection and/or first extragalactic interferometric images for certain species. For example, HCNH⁺ (Figure 21), protonated HCN or HNC (see Figures 3 and 5), is detected for the first time outside the Milky Way. It shows a similar distribution as that of HCN (Figure 3). One production pathway

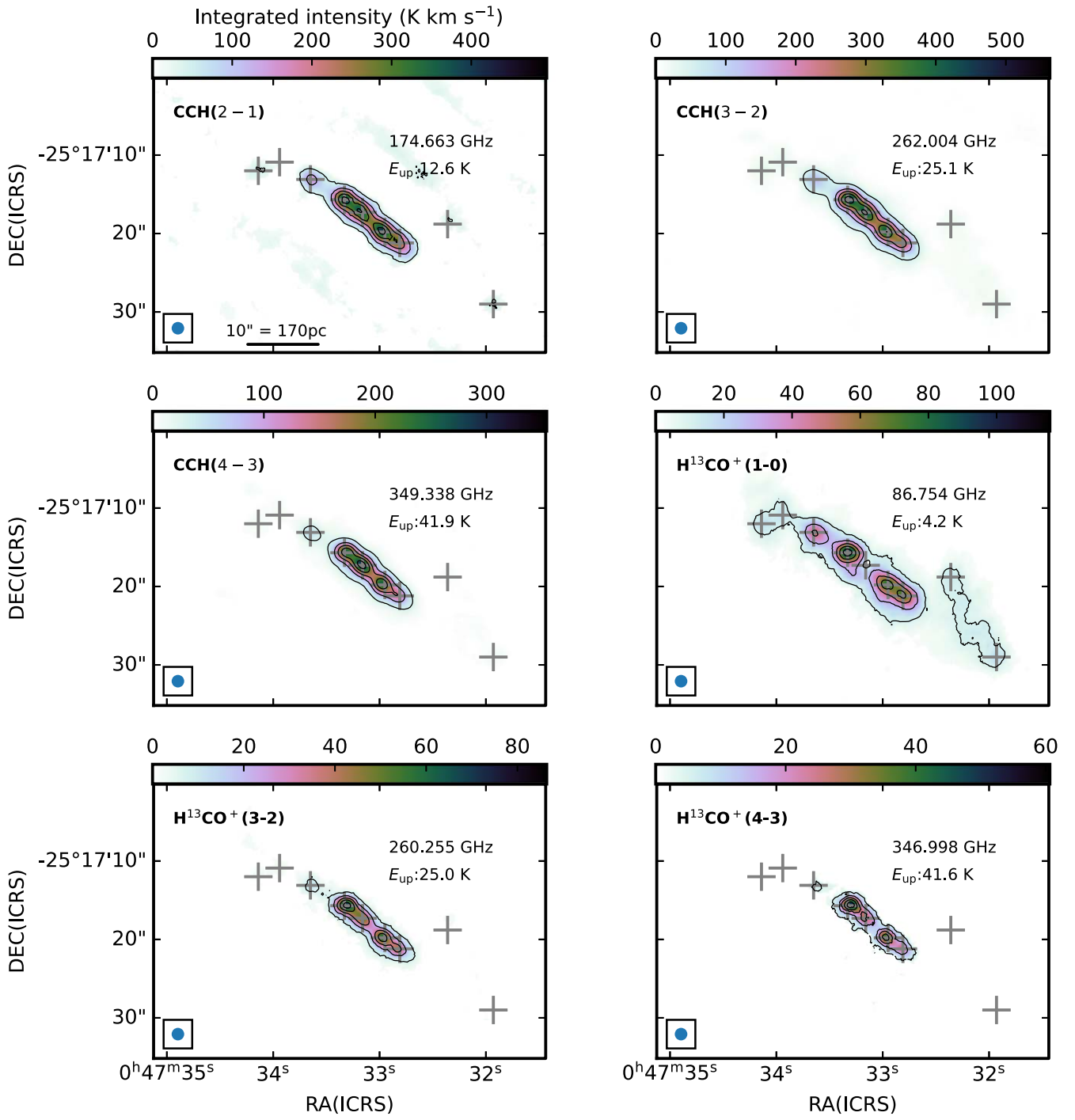


Figure 7. Same as Figure 2.

of HCNH^+ is via protonation of HCN or HNC by proton exchange reactions with H_3^+ or HCO^+ . Another formation route is through HNC^+ or HCN^+ reacting with molecular hydrogen. A survey of high-mass star-forming regions suggested that HCNH^+ is more abundant in cold starless cores compared with more evolved sources (Fontani et al. 2021). $\text{HCNH}^+(2-1)$ in the CMZ of NGC 253 has a similar distribution as that of HCN (1-0), but with a lower S/N (compare Figures 3 and 21). It is distributed widely in the entire CMZ rather than being concentrated around the starburst region. This is consistent with the picture that HCNH^+ is more abundant in cold clouds.

We also obtained the first extragalactic images of C_3H^+ , NO , and HCS^+ . C_3H^+ (Figure 20) is a tracer of PDRs, and was first detected by Pety et al. (2012) in a PDR of the Horsehead nebula. With a lower fractional abundance, this species was also detected in TMC-1 (Cernicharo et al. 2022). The first extragalactic detection of this species was made toward a molecular absorber at $z = 0.89$ (Tercero et al. 2020). Interstellar NO has been detected already several decades ago (Liszt & Turner 1978). Its first extragalactic detection was made in NGC 253 by Martín et al. (2003). Protonated CS, HCS^+ was detected for the first time by Thaddeus et al. (1981) rather

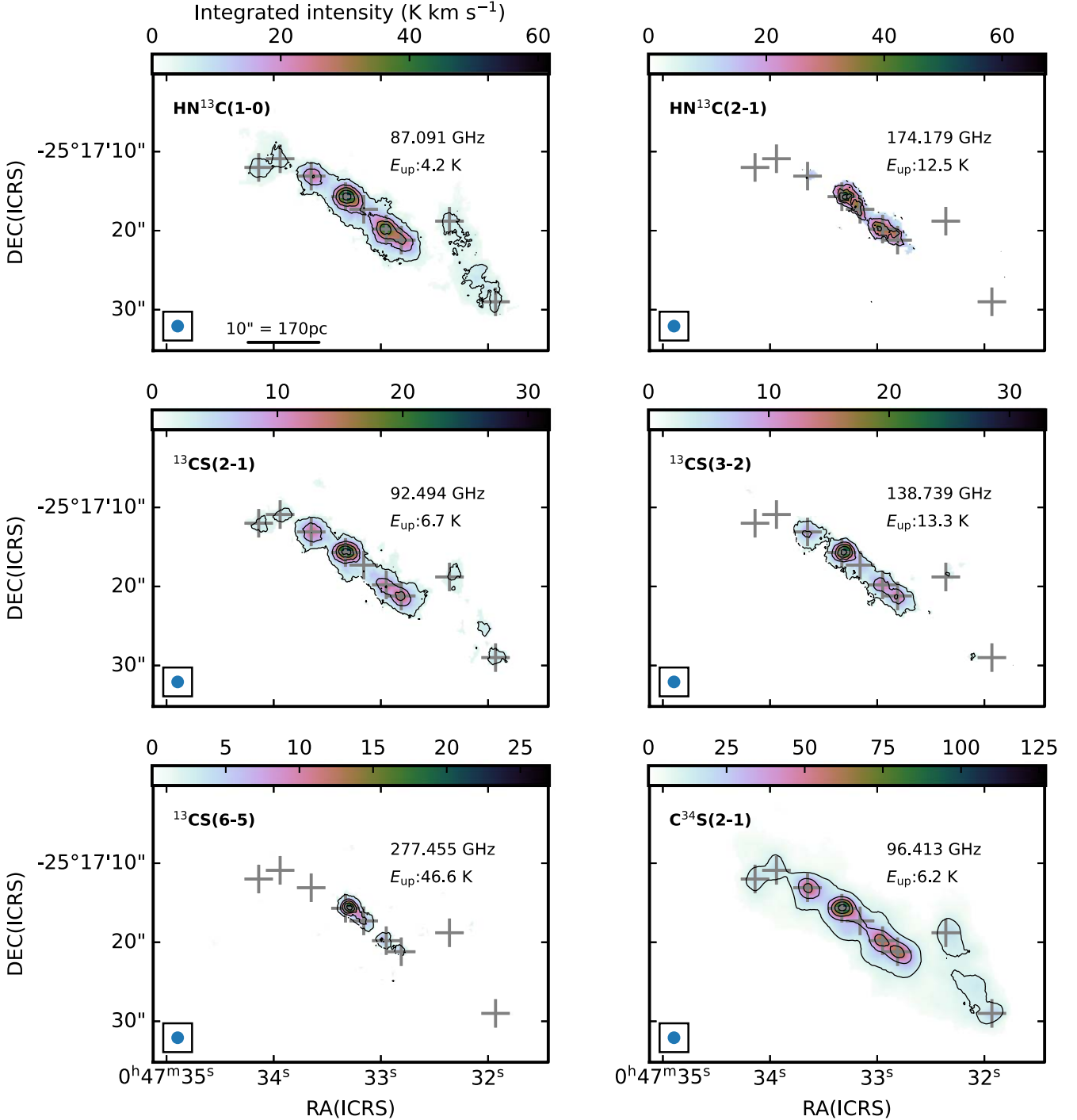


Figure 8. Same as Figure 2.

ubiquitously in hot cores and cold clouds. Its first extragalactic detection was also in a molecular absorber at $z = 0.89$ (Muller et al. 2013).

There are some moment 0 images that are used in PCA, but not shown in this paper because they will be included in dedicated publications, as indicated in Table 3. This is the case for the maps of sulfur-bearing species since Bouvier et al. (2024), which will provide a comprehensive presentation to investigate the origin of the emission of various sulfur-bearing species and discuss the physical processes that dominate their release/presence onto the gas phase. Other transitions of CO,

HCN , and HCO^+ contain rarer isotopologues such as ^{13}C , ^{18}O , ^{17}O , and ^{15}N . Butterworth et al. (2024) discusses isotopic ratios through the lens of these isotopologues in order to investigate the possible relation between these ratios and the ages of super star clusters (SSCs) observed in NGC 253. These images that are currently not included in this version of paper will be included later in the arXiv preprints after the above papers are accepted.

We note that some of the transitions in Band 5 have poor image qualities influenced by artifacts (e.g., $\text{H}^{13}\text{CO}^+ 2-1$, $\text{HOC}^+ 2-1$). These transitions come from the data sets that

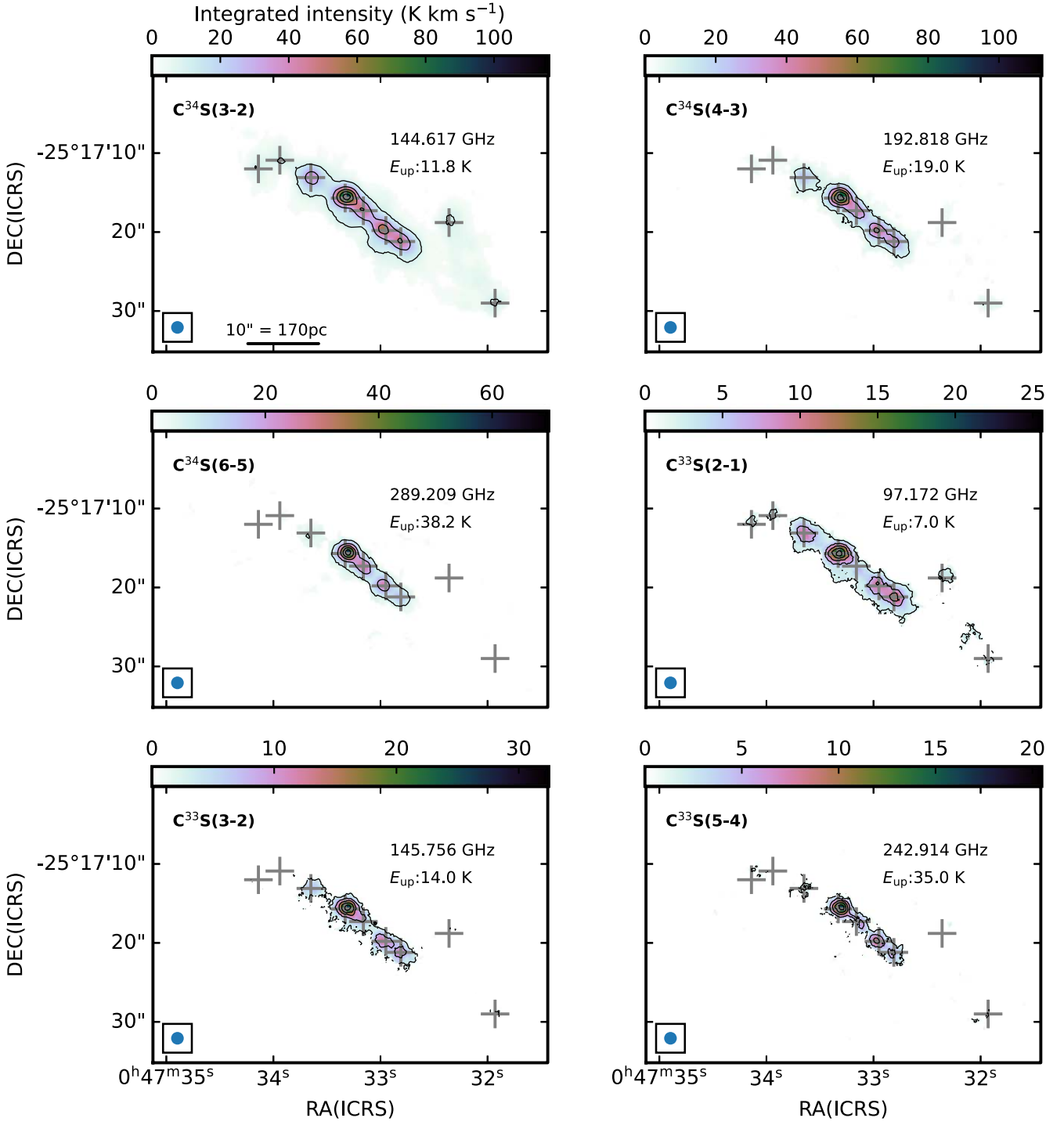


Figure 9. Same as Figure 2.

were not fully observed and did not meet the homogeneous sensitivity requested in this survey (see Section 3.2 of MMH21). This band has a water absorption line near the middle of the band, and the transitions nearby are prone to increased noise levels. PCA results for these transitions are less certain.

4. Principal Component Analysis

Astronomical data sets often have a large number of variables that are correlated to some degree. It is a challenge

to extract information from such data, and there is a need for a somewhat automatized statistical investigation. Dimensionality reduction is especially a useful technique in this regard, deriving a small number of components to reproduce most of the variations within the data. Multiple methods of dimensionality reduction have been developed so far, including PCA, nonnegative matrix factorization, and independent component analysis. PCA is one of the oldest and most commonly used with more than a century-old history (Pearson 1901). As mentioned in Section 1, PCA has been most widely used for molecular line studies (see references in Section 1). Moreover,

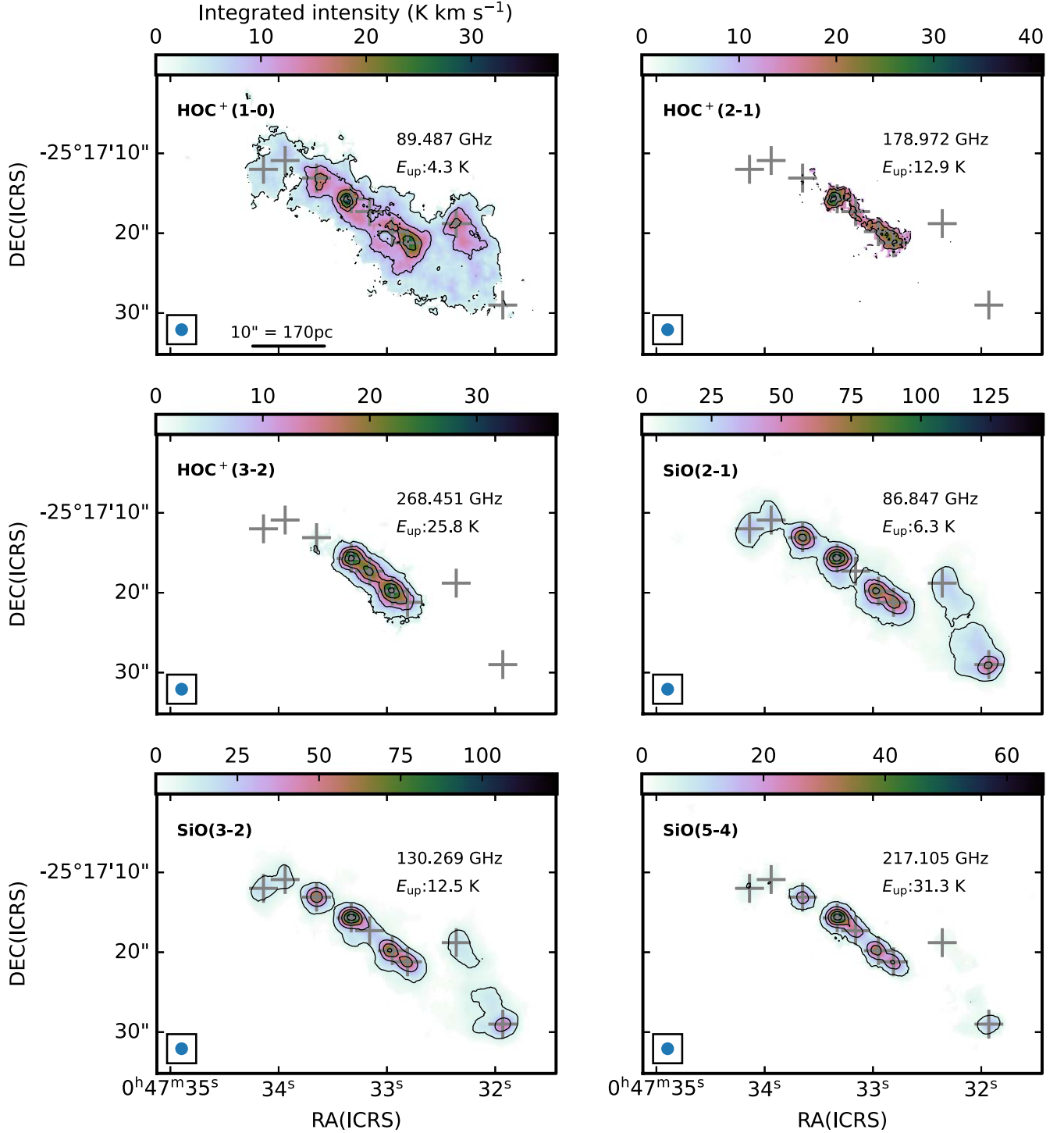


Figure 10. Same as Figure 2.

this work aims to push the PCA analysis to the next step by applying it to a much larger set of molecular lines.

4.1. The Basics of PCA

We begin by briefly describing the basics of PCA relevant to this work, leaving details and proofs to textbooks (e.g., Jolliffe 2002). A data set of p variables measured at n targets (e.g., intensities of p emissions at each of the n sky positions) can be viewed as n data points in a p -dimensional data space. PCA sets up an orthogonal coordinate system in the data space

with the origin at the centroid of the data points and the first coordinate axis (PC1 axis) in the direction of the largest variance of the data point positions along the axis. The PC2, PC3, ..., axes are successively defined as orthogonal to all previous axes and having the largest possible variance of the data positions along the axis. The coordinate values on a PC axis are called PC scores. The PC scores of the data points have a mean of zero for each PC and smaller variances for later PCs. Accordingly, the relative positions of the data points can be described reasonably well by using only their first q ($\leq p$) PC

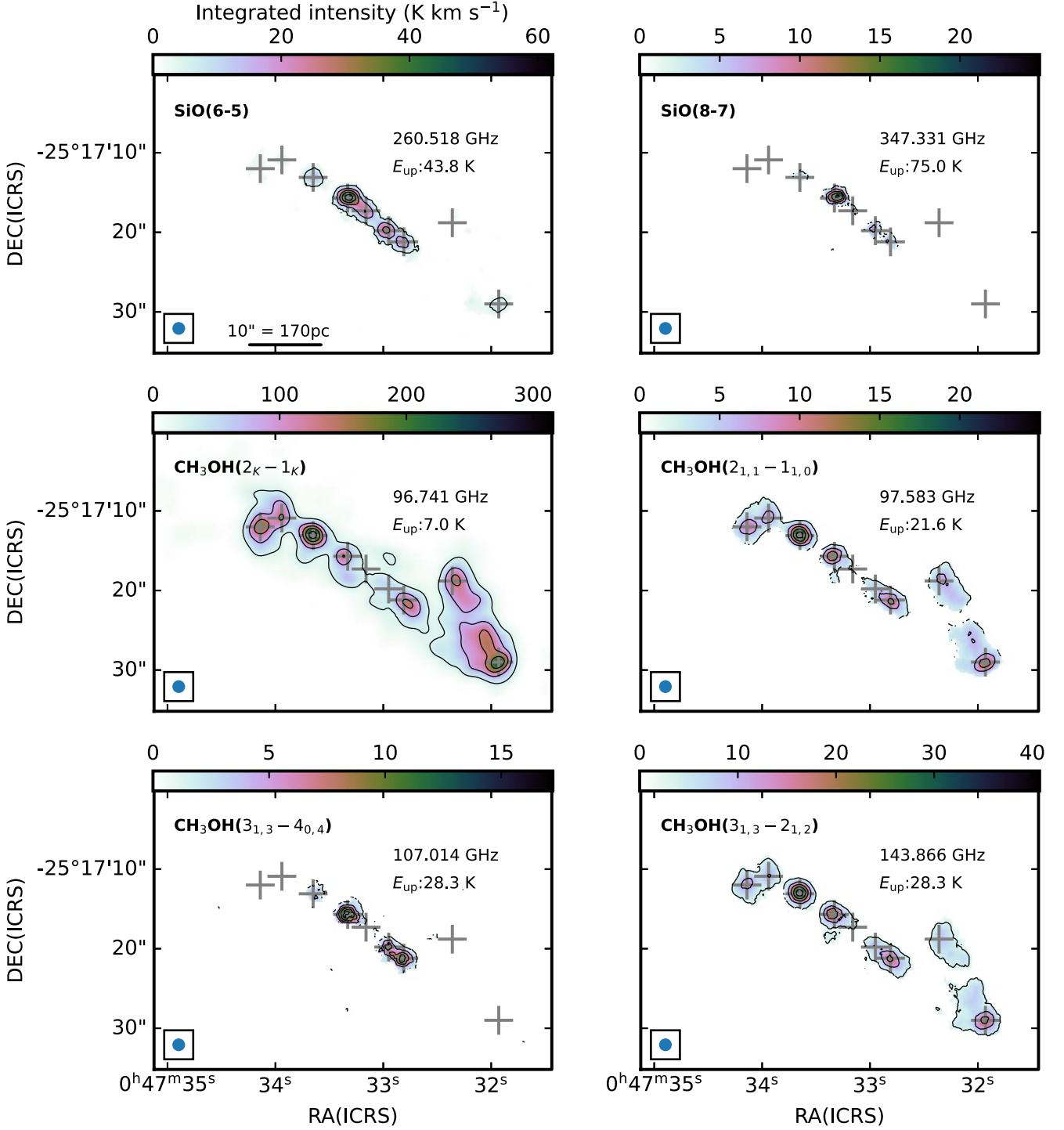


Figure 11. Same as Figure 2.

scores, since all the data points have approximately the same scores (≈ 0) for the rest of the PCs. This description reduces the dimensionality of the data set from p to q .

Individual PC axes are found in the following way. Let x_{ij} be the value of the j th variable measured at the i th target. The data matrix $X = (x_{ij})_{1 \leq i \leq n, 1 \leq j \leq p}$ has x_{ij} in the i th row, j th column. We use the data matrix that is standardized for each variable; i.e., each column has its mean subtracted and then divided by its standard deviation. This subtraction aligns the coordinate origin with the centroid of the data points. The correlation

matrix for the p variables is then $\Sigma = \frac{1}{n} X^T X$, where T denotes the transpose. The $p \times p$ real matrix is a symmetric and nonnegative definite, hence having p eigenvalues that are real and nonnegative. We denote them as $\lambda_1 \geq \dots \geq \lambda_p \geq 0$. The direction vector of the PC_j axis is the unit eigenvector of Σ associated with the j th largest eigenvalue λ_j , and we denote it as $a_j = (a_{1j}, \dots, a_{pj})^T$. They are orthonormal, i.e., $a_i \cdot a_j = \delta_{ij}$. The variance of the PC_j scores is λ_j .

The transformation between the data coordinates and the PC coordinates is as follows. Let z_{ij} be the PC_j score of the i th

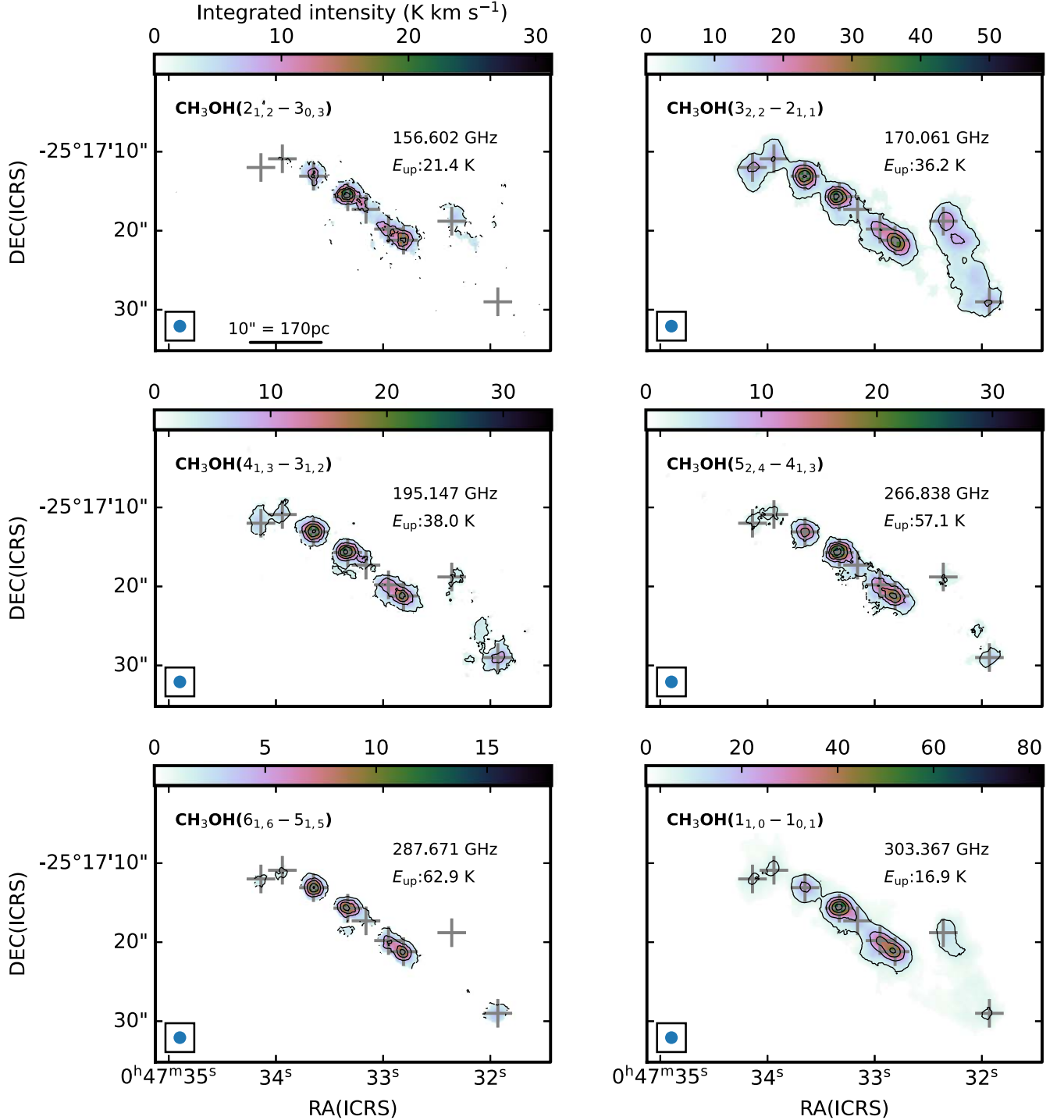


Figure 12. Same as Figure 2.

target. The target is located at $\mathbf{z}_i = (z_{i1}, \dots, z_{iq})$ in the q -dimensional PC coordinates, and $\mathbf{x}_i = (x_{i1}, \dots, x_{ip})$ in the standardized data coordinates. Since z_{ij} is the projection of \mathbf{x}_i onto the PC j axis along the unit vector \mathbf{a}_j , we have $z_{ij} = \mathbf{x}_i \mathbf{a}_j$, and $\mathbf{z}_i = \mathbf{x}_i \mathbf{A}$, where \mathbf{A} is the matrix $\mathbf{A} = (\mathbf{a}_1, \dots, \mathbf{a}_q) = (a_{ij})_{1 \leq i \leq p, 1 \leq j \leq q}$. The element a_{ij} is the direction cosine between the i th data axis and the PC j axis, and is usually referred to as a *coefficient* or *loading* for PC j . If it is positive, a positive value of the i th variable makes a positive contribution to the PC j score, while a negative a_{ij} indicates a negative contribution.

For the simplest case of two variables with a strong correlation, the PC1 axis would lie in the direction along the linear fit of the data points, while the PC2 axis would be in the direction perpendicular to it. Therefore, PC1 scores indicate the strength of the common properties in the two variables, while PC2 scores reflect the strength of the differential properties of the two variables.

PC scores are uncorrelated between different PCs because Σ is diagonal in the PC coordinates. Therefore, if the variables are determined by underlying parameters with some correlations,

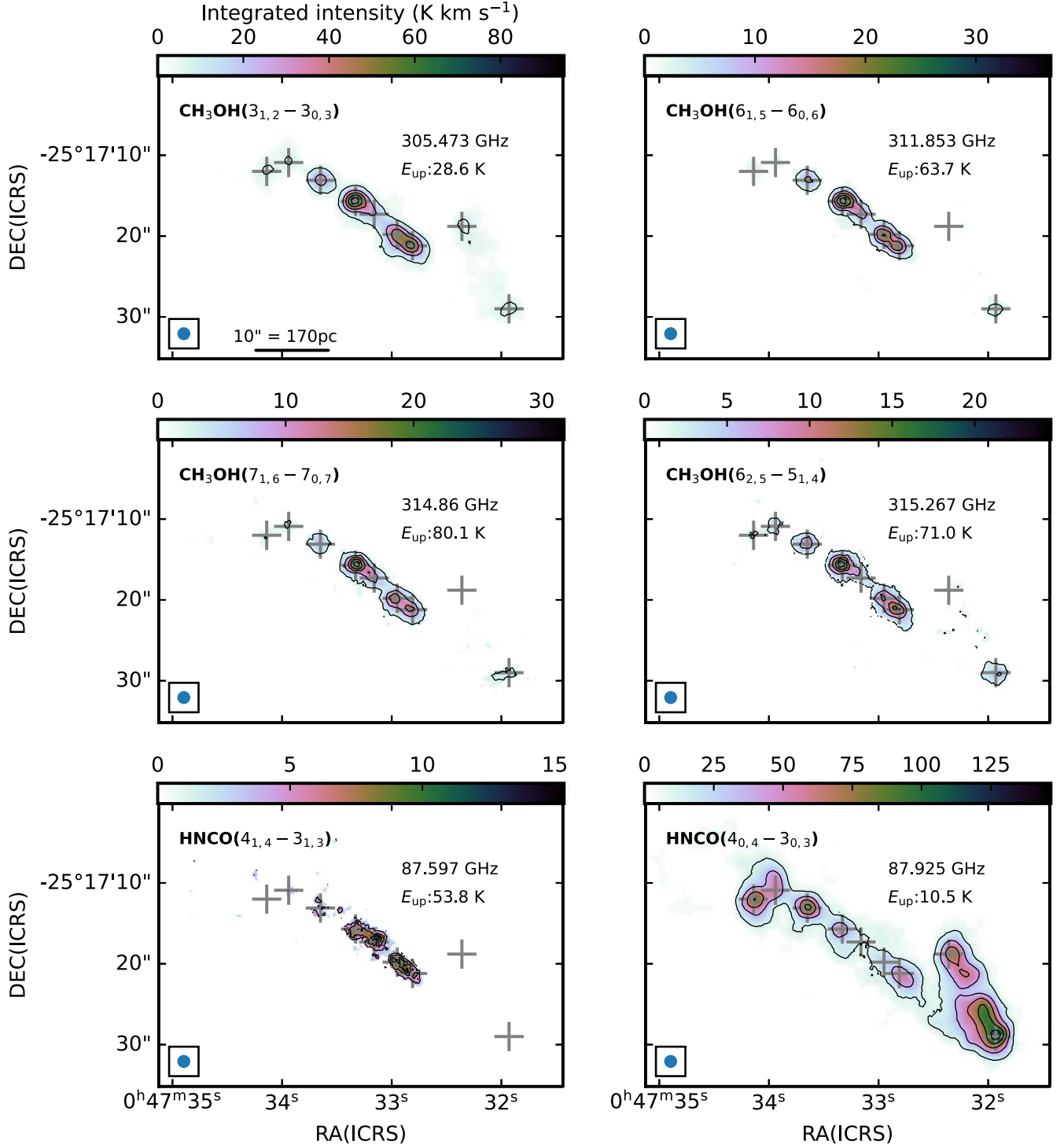


Figure 13. Same as Figure 2.

then there would not be a one-to-one relationship between those parameters and the principal components. We discuss this caveat when we apply PCA to the ALCHEMI data.

4.2. Application of PCA to the ALCHEMI Data

We binned the velocity-integrated images into hexagonal pixels with a horizontal length of $0.^{\circ}8$ using Python's hexbin function. The number of hex-pixels is $n = 2723$. The choice of

half the beam size is made for the Nyquist-like sampling. We filled the masked out channels/pixels with zero.

We standardized our data for each variable (i.e., transition or emission) as described in Section 4.1. The division by the standard deviation is a common procedure for a data set whose variables differ greatly in their variances. It also makes our PCA independent of the choice of data units between janskys and kelvin.

The variables in our analysis are transitions, and the targets are sky positions, as in Ungerechts et al. (1997) or Meier &

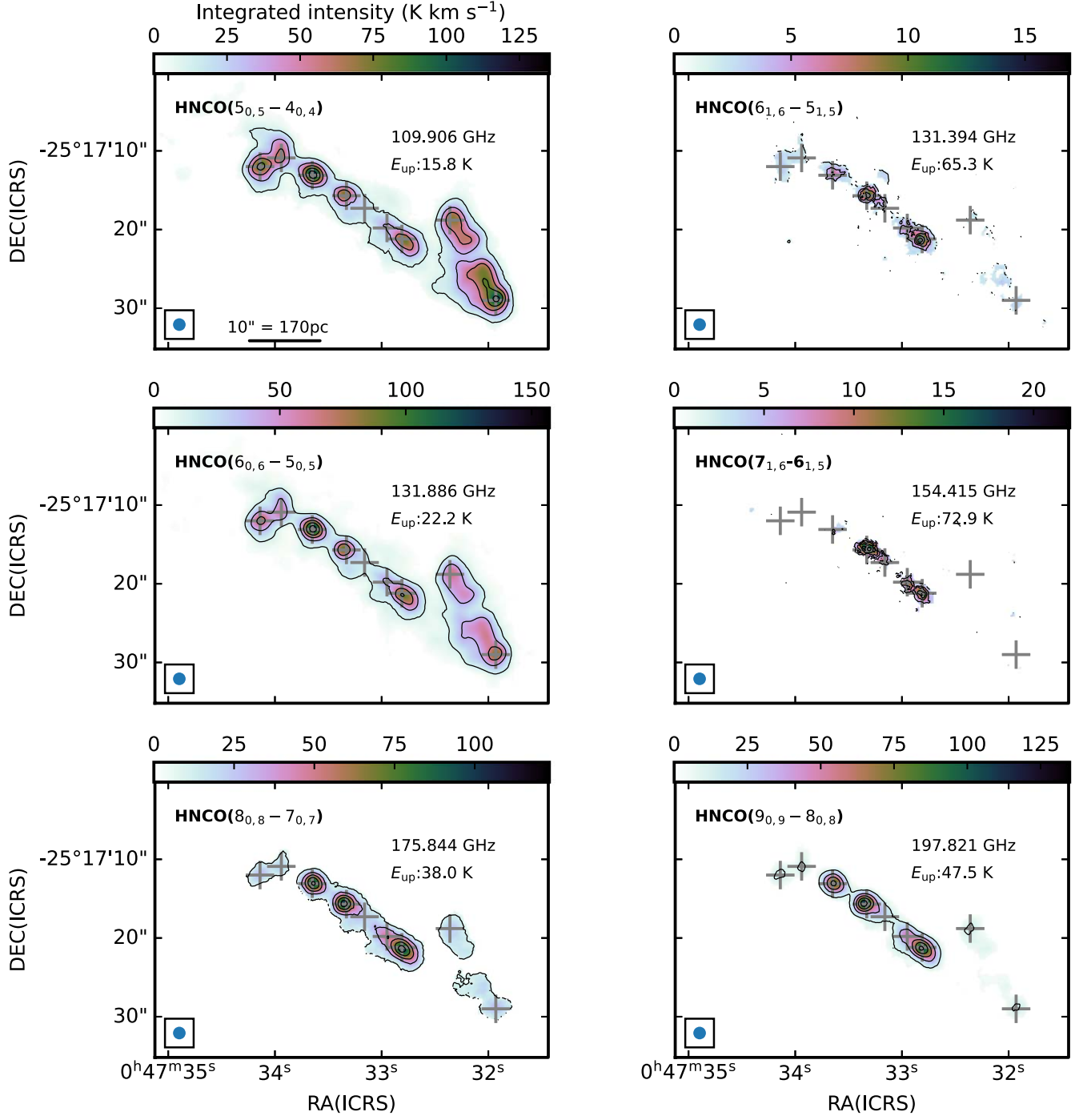


Figure 14. Same as Figure 2.

Turner (2005). With 148 lines and two continuum images, we have $p = 150$ variables. Instead, we could have used different transitions as targets and their intensities at the pixels as variables, as in facial recognition, where eigenvectors are eigenfaces. However, we did not use the approach to avoid the problem of high dimension and low sample size (i.e., $p > n$).²⁹ It is also possible to conduct a PCA on image cubes, instead of integrated intensities. Nonetheless, we use integrated-intensity images first, because integrated intensities tend to have higher

S/Ns. A PCA on image cubes, possibly with a lower number of transitions, is planned as a future work. Consequently, there are PC k scores for all hexagonal pixels, $\{z_{ik}\}_{i=1,\dots,n}$. We used the PCA package from the scikit-learn project (Pedregosa et al. 2011).

The number of principal components q must be chosen to retain most of the information in the data set. The information in the context of PCA is the configuration of the data points and is evaluated with the variances. For example, PC k has the variance of λ_k in its scores and therefore has less information for larger k . Figure 23, called a scree plot, shows the fraction of the variance of each PC in the total variance,

²⁹ See Takeuchi et al. (2022) for how to properly perform PCA on such a data set.

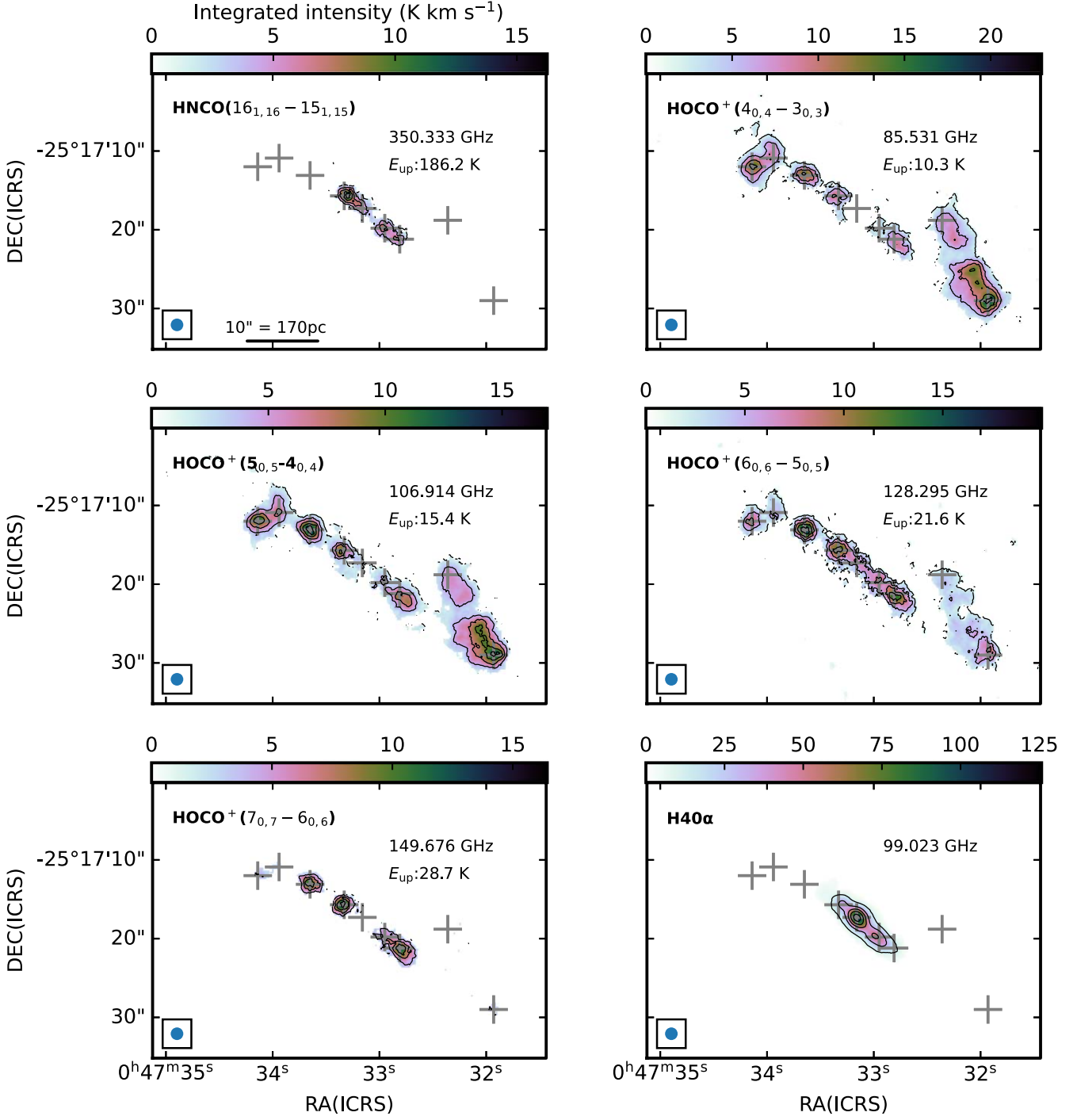


Figure 15. Same as Figure 2.

$f(k) \equiv \lambda_k / \sum_{j=1}^p \lambda_j$. In this plot, the PCs that exceed the least-squares linear fit to the high-order PCs (PC6–PC20) are considered more significant. The first three PCs have relatively large fractions of information (i.e., variance) $f(k) = 79.4\%$, 9.0% , and 5.0% , respectively, for $k = 1, 2, 3$, with a cumulative contribution of 93% of the total. PC4 and PC5 also show some significance ($f(k) = 1.8\%$ and 1.2%) exceeding the fit at PC6–PC20, each of which has $f(k) \leq 0.6\%$. As shown in Section 4.3, the PC score maps for PC6 and higher are noisier than for PC1–

PC5. Therefore, we only discuss PC1–PC5 in this paper; they have $\sum_{j=1}^5 \lambda_j / \sum_{j=1}^p \lambda_j = 96.4\%$ of the total variance.

PCA is one of the unsupervised machine-learning methods, which means that any known properties of data, or labels, are not used. This means that PCA results are derived independent of what kind of species the molecules are, or energy levels of the transitions. We will see below (in Section 4.4) that our PCA could recover such information to some extent from the data alone.

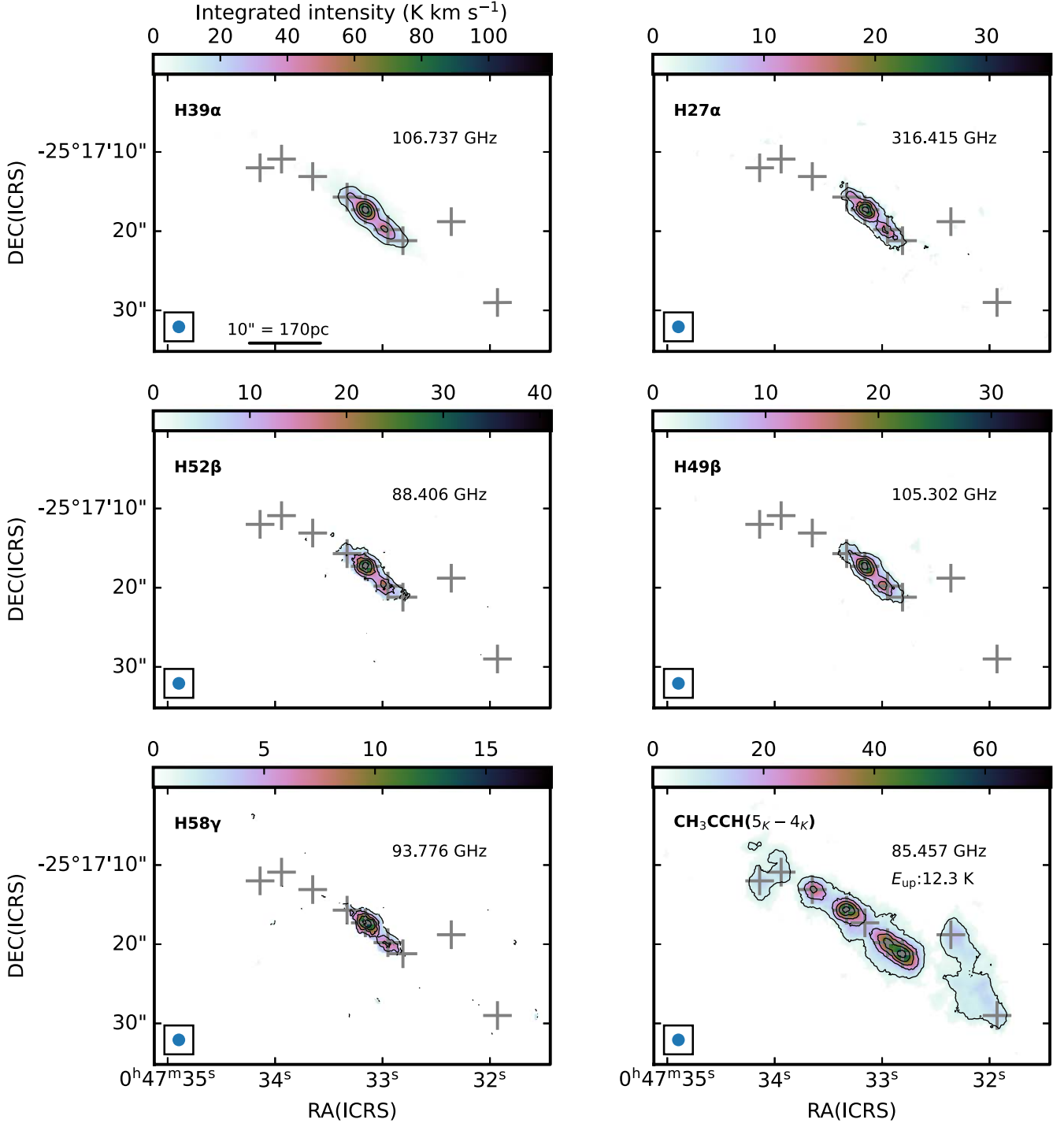


Figure 16. Same as Figure 2.

4.3. PC Score Maps

Figures 24 and 25 show the projection of data points onto the PC axes ($\{z_{ik}\}_{i=1,\dots,n}$ for PC k in the notation of Section 4.1), or the maps of PC scores for the first 10 PCs. Here, we provide a brief overview of the relationship between the individual PCs and the emission of certain molecular species. Note that the PC scores are dimensionless and have little meaning in their absolute values. Only their relative magnitudes between different PCs and positions are relevant. The PC1 score map (Figure 24 top left) shows a rough shape of the CMZ, similar to

the distribution of CO isotopologues. The positive PC2 scores (Figure 24 top right) appear near the central starburst regions (GMCs 4–6), where the high- J transitions of HCN emission and RRLs have high intensities. On the other hand, the negative PC2 scores are at the outskirts of the CMZ, where low- J transitions of CH₃OH and HNCO are enhanced (GMCs 1–3, 7–9). Note that the green (CH₃OH 2 K -1 K) and red (H39 α) colors in Figure 1 (top) show remarkable similarity with blue (negative) and red (positive) colors in the PC2 score map (Figure 24). High absolute values of the PC3 scores (Figure 24

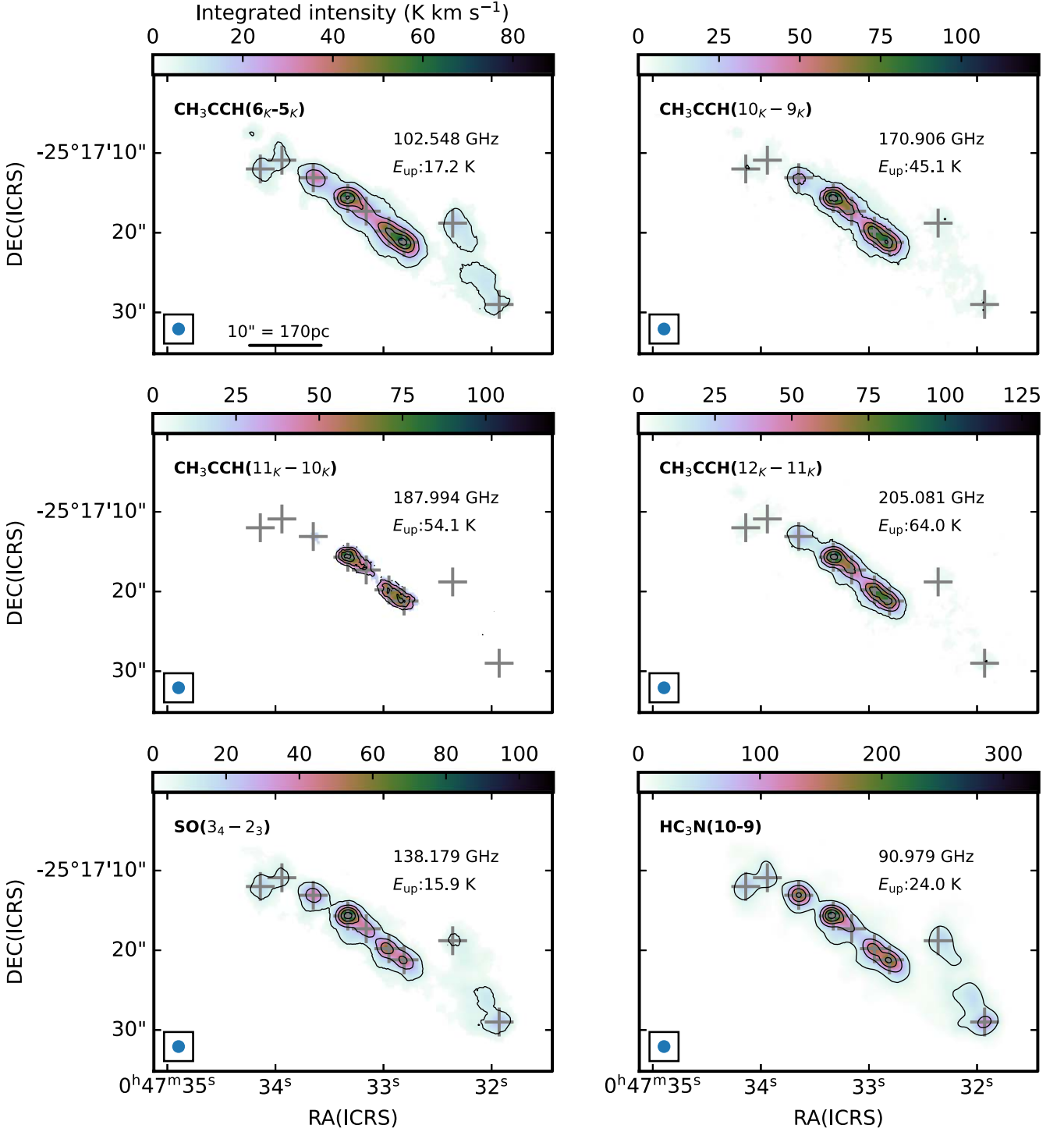


Figure 17. Same as Figure 2.

middle left) appear around positions with positive values of the PC2 score map. Positive PC3 scores appear at the peak location of HC_3N vibrationally excited lines (GMC 6) while the negative PC3 scores are at the peak of the RRL (GMC 5). We again note that the green ($\text{CN } 3-2$) and red ($\text{HC}_3\text{N } 25-24$) colors in Figure 1 (bottom) resemble the blue and red colors in the PC3 map.

As mentioned earlier, the contributions of PC4 and PC5 (Figure 24 middle right and bottom left) are less than those of

PC1–PC3. They may contain multiple physical components because PCs (eigenvectors) are by definition orthogonal to each other while each physical component does not necessarily influence the intensities orthogonally in dimensions of transition intensities. For example, PC4 has positive PC scores in most of the GMCs except for GMCs 3 and 7. The PC4 score map appears similar to that of PC2, except for GMCs in the outskirts (GMCs 1, 2, 7, 8, and 9). The PC4 score map also has an extended structure out of the galactic plane with the negative

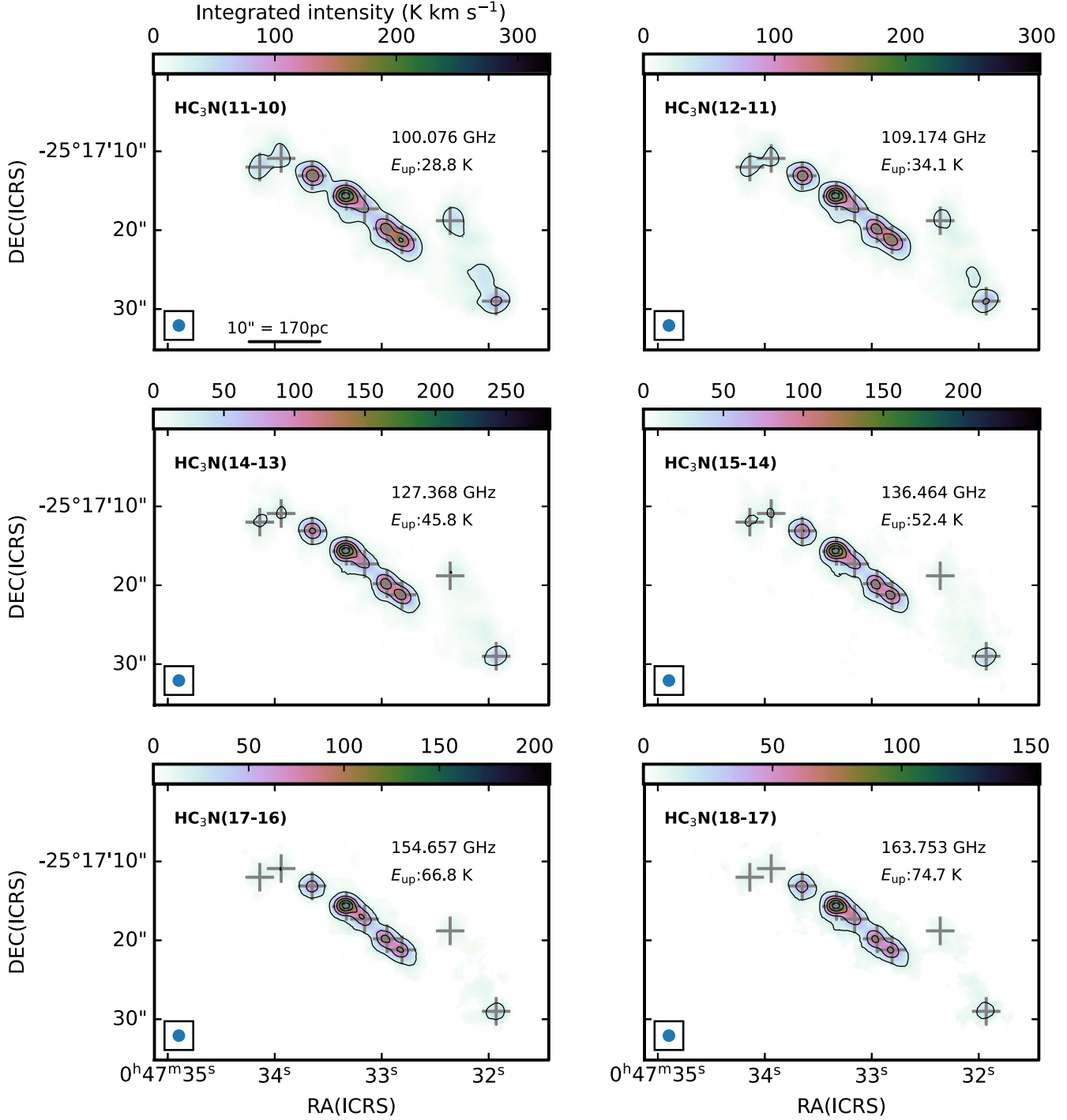


Figure 18. Same as Figure 2.

component. PC5 shows negative PC scores in most of the GMCs, but it has positive PC scores in GMC 6 and a diffuse extended structure.

In principle, PC6 and higher-order maps still provide some information about this galaxy, not merely contributions due to noise. However, PC score maps from PC6 to PC10 cannot be uniquely linked to the emission of individual species and therefore cannot easily be linked to specific physical processes (Figures 24 and 25).

4.4. Relationship with Physical Parameters

Here, we examine whether each PC has any clear relationship with physical parameters such as column densities, kinetic temperatures, and volume densities. Figure 26 shows the relationship between the PC scores in our results and physical conditions derived by Tanaka et al. (2024) from the ALCHEMI data. These physical parameters were obtained from the hierarchical Bayesian analysis method developed by Tanaka et al. (2018). Tanaka et al. (2024) present results from different

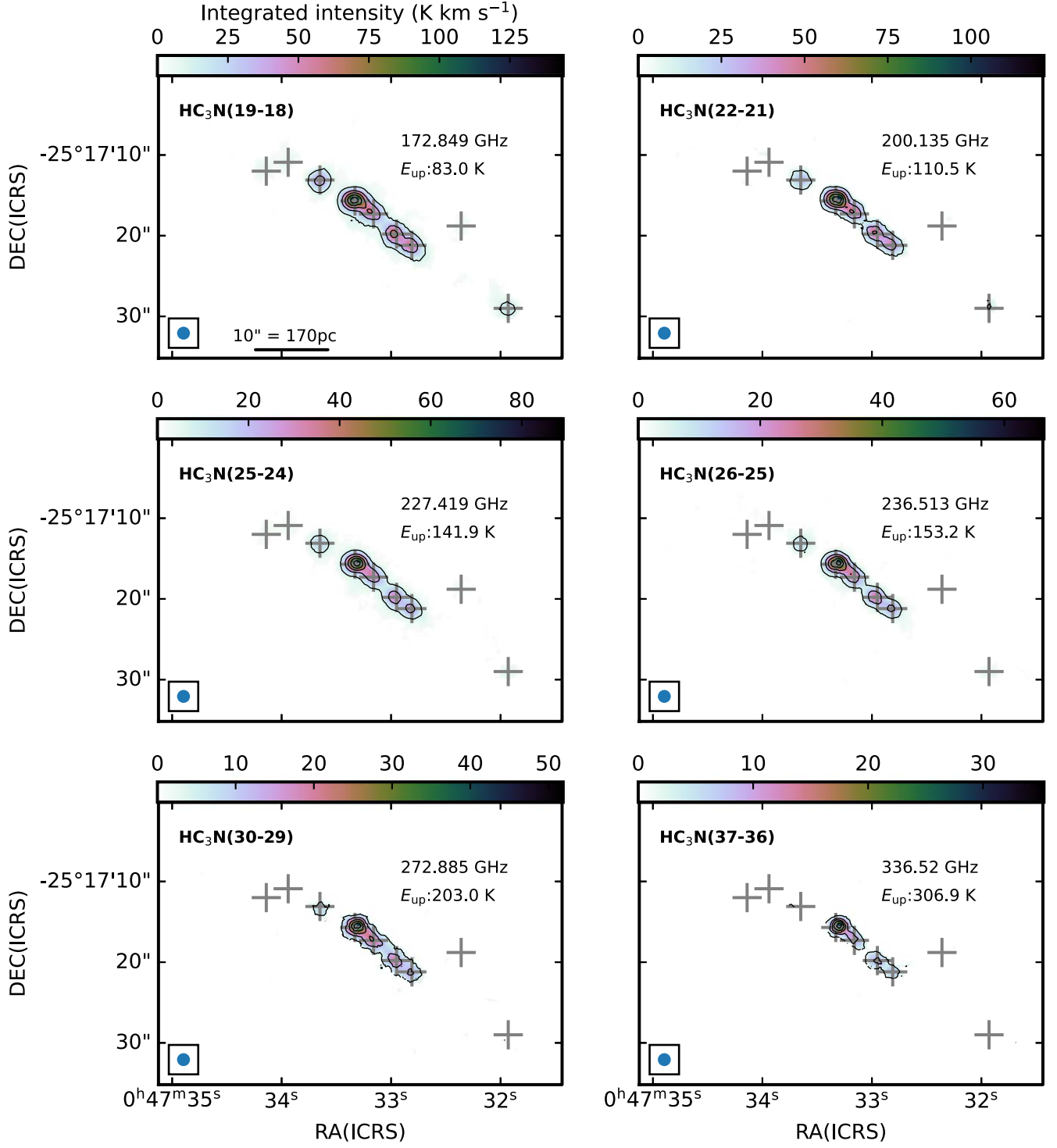


Figure 19. Same as Figure 2.

sets of transitions. Among their results, we use their “high-HB” model derived from species with higher critical densities such as HCN, HCO^+ , and their isotopologues, HC_3N , and SiO , instead of results derived from CO isotopologues. This is because our PCA used more species with high critical densities than CO isotopologues. The pixels from N_{H_2} -weighted averaged images along the velocity axis are binned to the same hexagonal pixels as our PCA. We omitted hexagonal pixels that do not have physical parameters derived for all the original pixels within the hexagon. We show pixels within one

standard deviation of all the data points of PC1 scores from zero in gray because they represent pixels with low S/Ns. The standard deviation of PC1 scores is 21. We note, however, that not all the gray points are noise. We only show relations with PC1 and PC2 because there are no clear trends for PC3 and higher.

PC1 scores show a clear increasing trend with increasing column densities. They also have a similar, but weaker correlation with volume densities, and even to a lesser degree, with temperatures. These results suggest that PC1 primarily

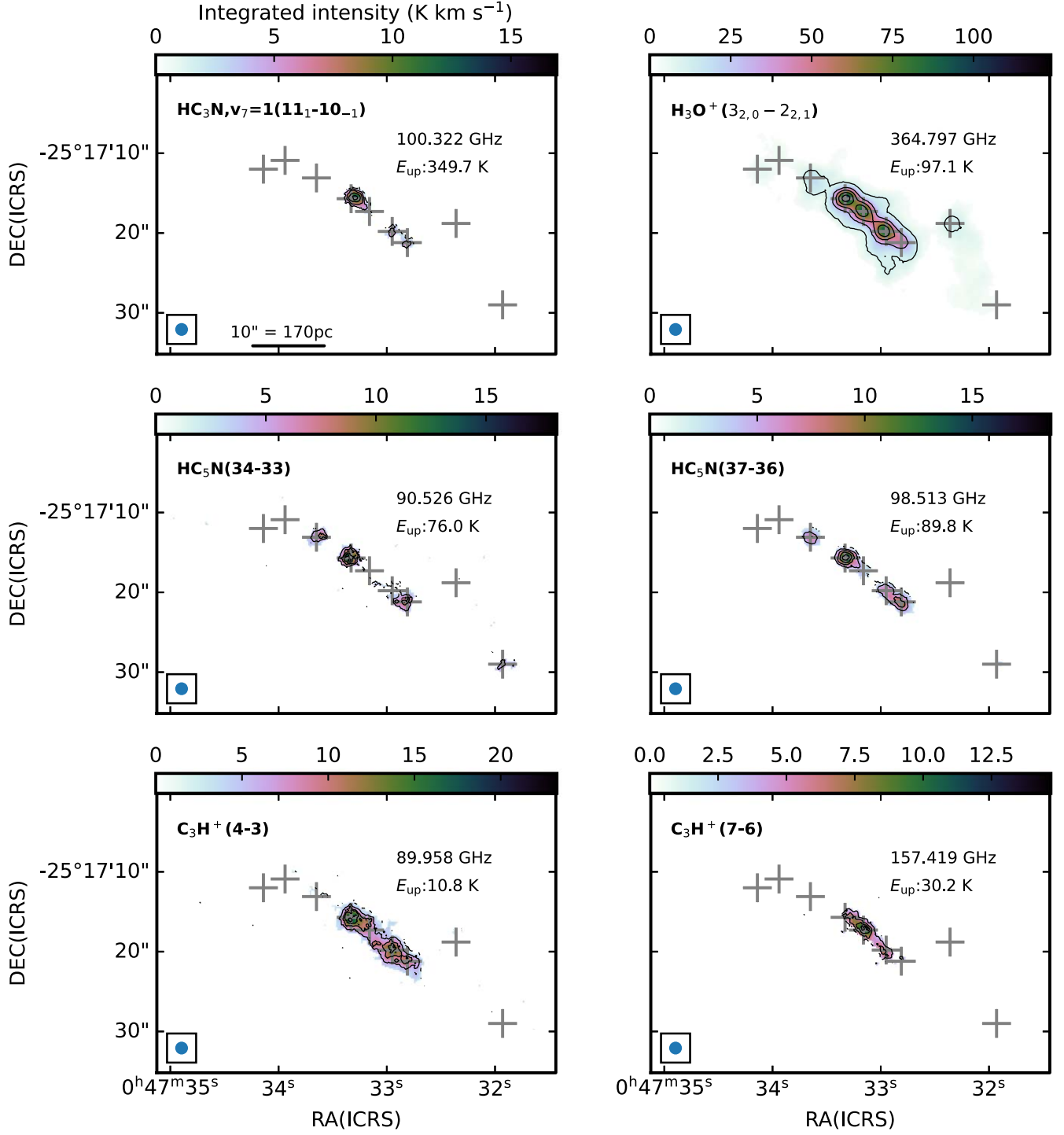


Figure 20. Same as Figure 2.

represents the overall molecular gas content. The volume densities tend to be higher in high-column-density regions in Tanaka et al. (2024), and this is likely why PC1 and the volume densities have a positive correlation. The high-density regions are also the regions with high star formation rates, which explains the trend of increasing PC1 scores with increasing temperatures.

PC2 scores increase with the increasing values of all of these physical parameters (column densities, volume densities, and temperature) if we focus on high S/N pixels (blue points in

Figure 26). This correlation between PC2 scores and physical parameters is tightest in the temperature, while it gets slightly weaker in the density. The scatter becomes larger between PC2 scores and the column density. To consider the relationship between PC2 and physical parameters in a different perspective, we consider PC2 coefficients (a_{i2} in the notation of Section 4.1), instead of PC scores discussed above, of multiple transitions of HCN, CS, C^{34}S , and HC_3N . Figure 27 shows the dependence of PC2 coefficients on upper-state energies (left figure) and critical densities (right figure). For all the species,

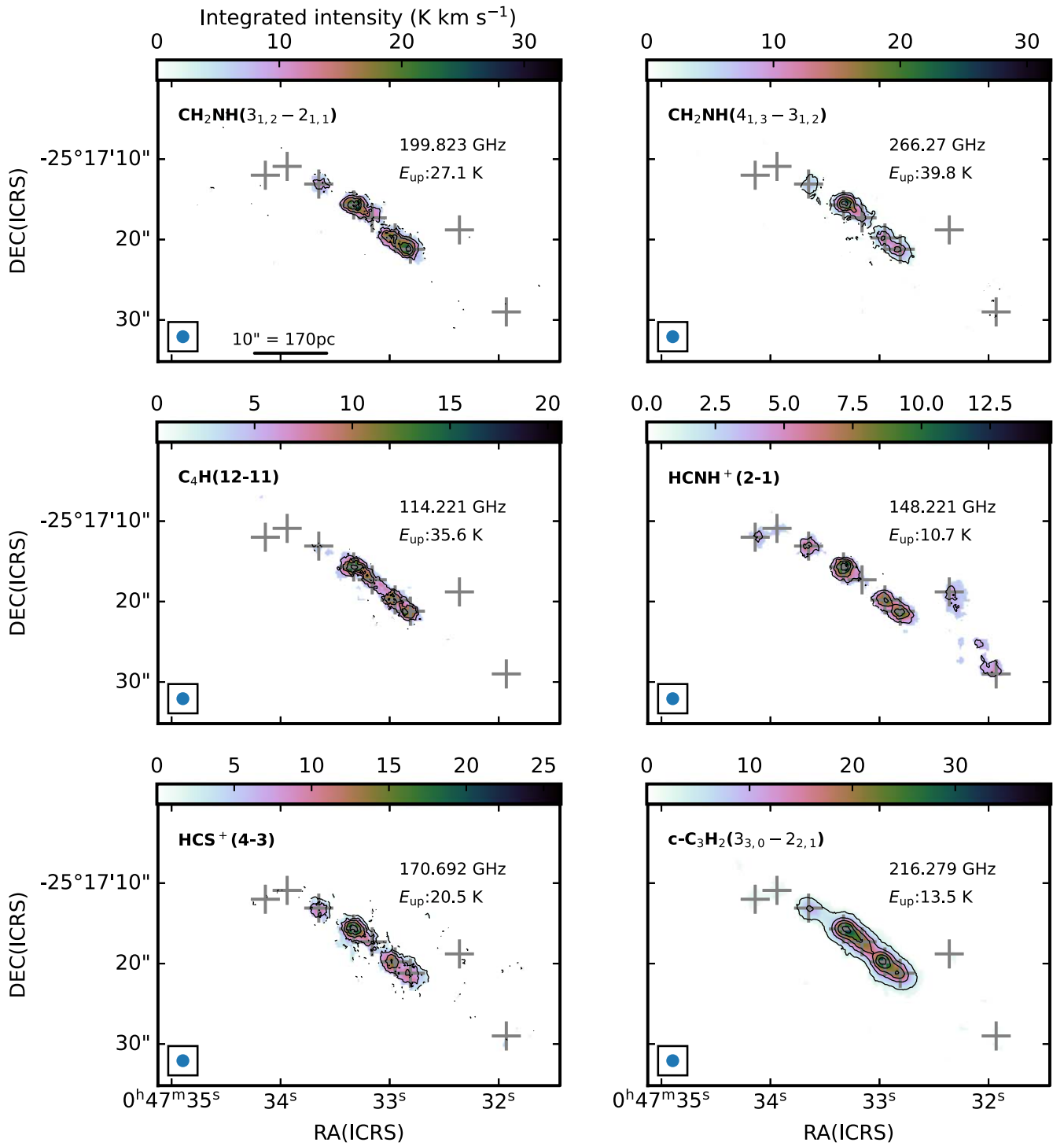


Figure 21. Same as Figure 2.

PC2 coefficients tend to be higher with higher upper-state energies and critical densities. The transitions with high PC2 coefficients clearly emit preferentially from increasingly higher-excitation regions.

4.5. PC Coefficients of Each Species

Figures 28–32 show the coefficients of various transitions for PC1–PC5, i.e., a_{ij} for a transition i , and PC j for $j = 1–5$. A table of these coefficients can be found in Appendix C. Figure 33 also shows the same information, but for transitions that are not

shown in Figures 28–32. The errors of the coefficients are evaluated in Appendix D and are negligible. Figures 28–32 are separated into four panels. The first two panels are for dense gas tracers (HCN, HNC, HCO⁺, CN, and their isotopologues, as well as N₂H⁺, HC₃N) and shock tracers (CH₃OH, SiO, HNCO, and HO⁺)³⁰. The colors indicate the upper-state

³⁰ While HO⁺ is not a conventional shock tracer, we consider it a shock tracer here because of the results obtained by Harada et al. (2022) who found an association between HO⁺ and shocks in NGC 253.

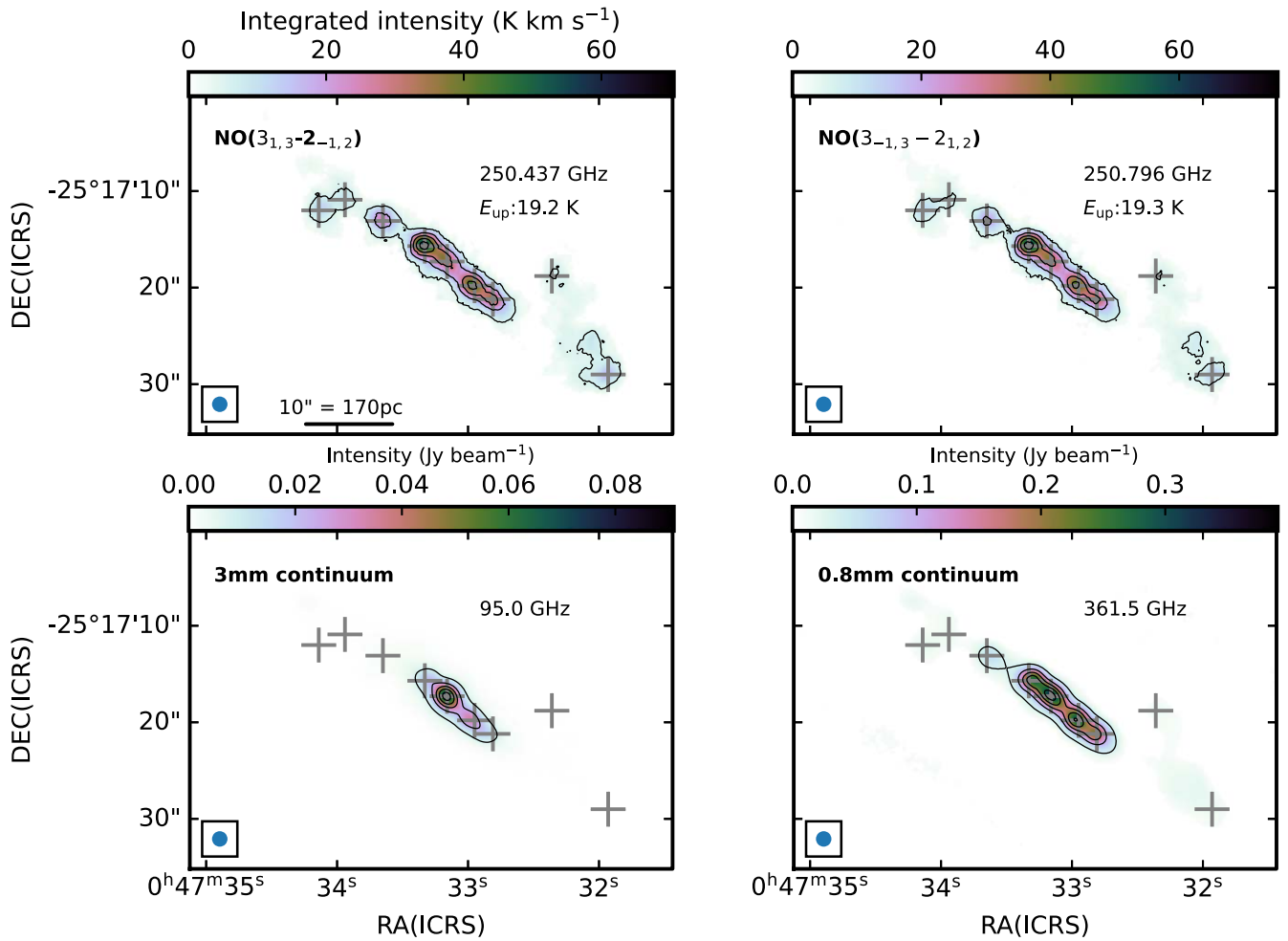


Figure 22. Same as Figure 2.

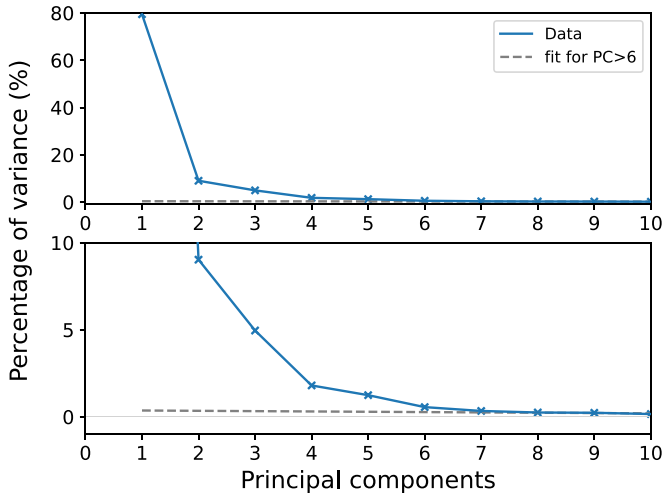


Figure 23. Top: a scree plot for our PCA. Bottom: the same as the top figure, but for a narrower range of the y-axis.

energies of transitions from 0 to 100 K in cyan to blue for dense gas tracers, and lime to green for shock gas tracers. The third panel shows CO isotopologues, continuum, RRLs, vibrationally excited HC₃N, and CH₂NH, and the fourth panel is for sulfur-bearing molecules. The fourth panel also shows upper-state energies with colors (0–100 K with pink to purple).

Figures 28 and 33 show that all the transitions have positive coefficients in PC1. The variation of PC1 coefficients among transitions is not large. This result can easily be explained by the fact that PC1 correlates with the emission brightness of these transitions. Consequently, PC1 in general traces overall gas column density as described in Section 4.4 because the regions with higher column densities tend to have a higher brightness. Star formation tracers such as RRLs and the 3 mm continuum also have positive PC1 values because the star formation rate is generally higher toward the high-column-density regions.

High absolute values of PC3 scores (around GMCs 5 and 6) appear in regions with positive values of PC2 scores (Figure 24). Negative PC3 coefficients are seen for RRLs, while high-excitation dense gas tracers have positive PC3 coefficients (Figure 30). It is interesting to note that most of the shock tracers and sulfur-bearing molecules have positive PC3 coefficients, unlike dense gas tracers. Meanwhile, CO isotopologues and continua all have negative PC3 coefficients. PC3 separates high-excitation transitions with high PC2 coefficients into different groups as illustrated in Figure 34. High-excitation transitions of CN, HNC, HCN, and RRLs have negative PC3 coefficients (the fourth quadrant in Figure 34)³¹

³¹ We number quadrants counterclockwise from the top right.

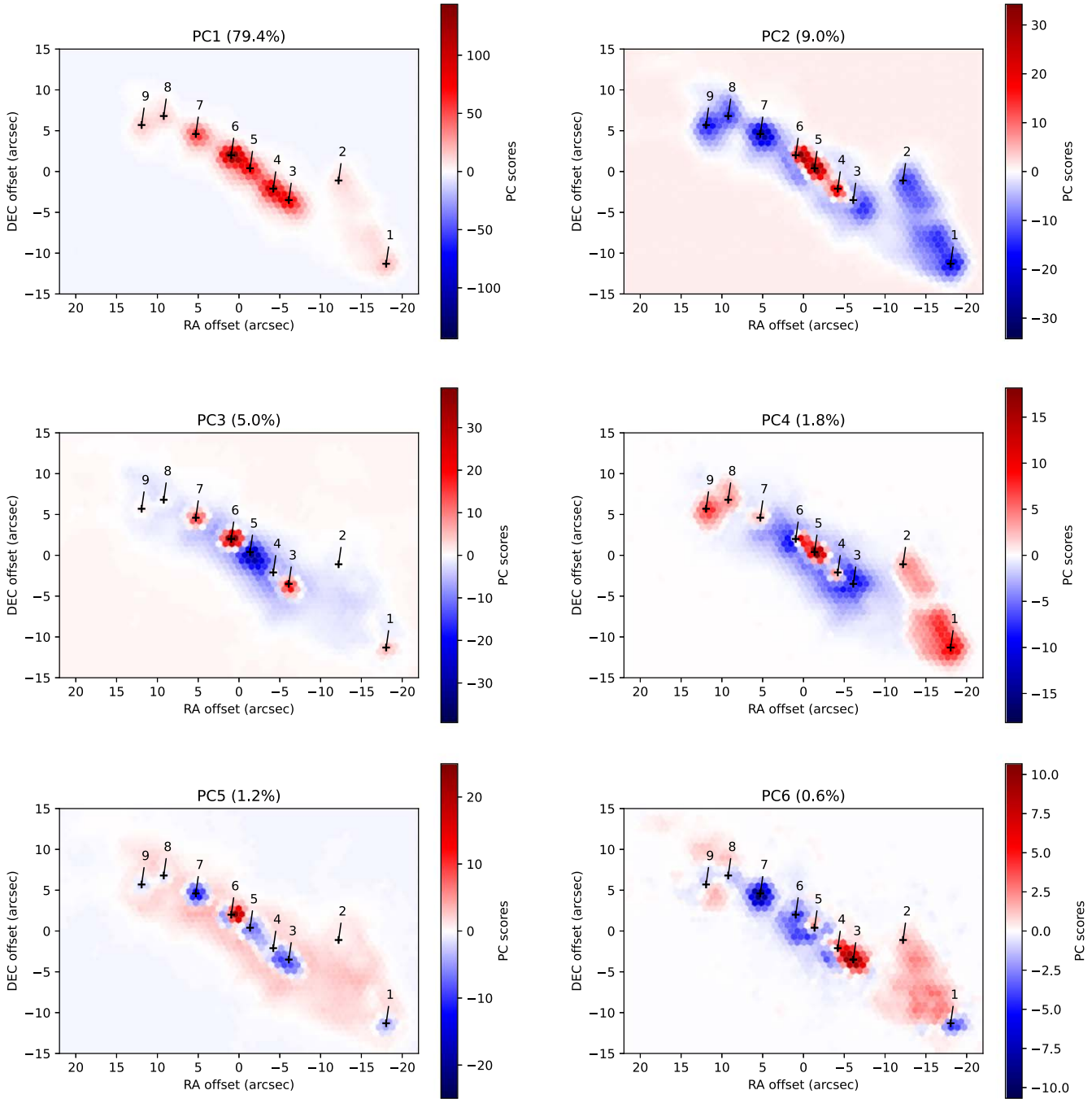


Figure 24. PC scores of the first to sixth principal components (i.e., $\{z_{ij}\}_{1 \leq i \leq n}^{j=1-6}$). GMC positions listed in Table 1 are shown with black crosses. The origin is at the phase center of the observation, $\alpha = 00^{\text{h}}47^{\text{m}}33\overset{\text{s}}{.}26$, $\delta = -25^{\circ}17'17\overset{\text{s}}{.}7$ (ICRS).

while HC₃N transitions have positive ones (the first quadrant in Figure 34).

As mentioned previously, there are some similarities between the PC2 and PC4 score maps near the central starbursts. However, there are also interesting exceptions in the outskirts (Figure 24). Therefore, if a transition has positive coefficients for PC2 and PC4 (the first quadrant in Figure 35), it has stronger emission in GMCs 4, 5, and 6 than that which can be accounted for by PC2 alone. On the other hand, if a transition has negative PC2 and positive PC4 coefficients (the second quadrant in Figure 35), the contributions from the CMZ outskirts are significant (GMCs 1, 2, 7, 8, 9).

Positive PC5 scores are at either GMC 6 or the component extended toward higher galactic latitudes likely associated with outflows, while the area of negative PC4 scores contain these outflow-related extended structures and GMC 3 (Figure 24). Because the vertically extended structure is likely caused by outflows and is of interest, we picked out transitions tracing this structure by comparing PC4 and PC5 coefficients in Figure 36. The transitions of our interest should have negative PC4 and positive PC5 coefficients and in the second quadrant of the figure. Because these outflow features also appear weakly as negatives in the PC3 score map, we also compare PC3 and PC5 coefficients in Figure 37, where the outflow tracers should be in

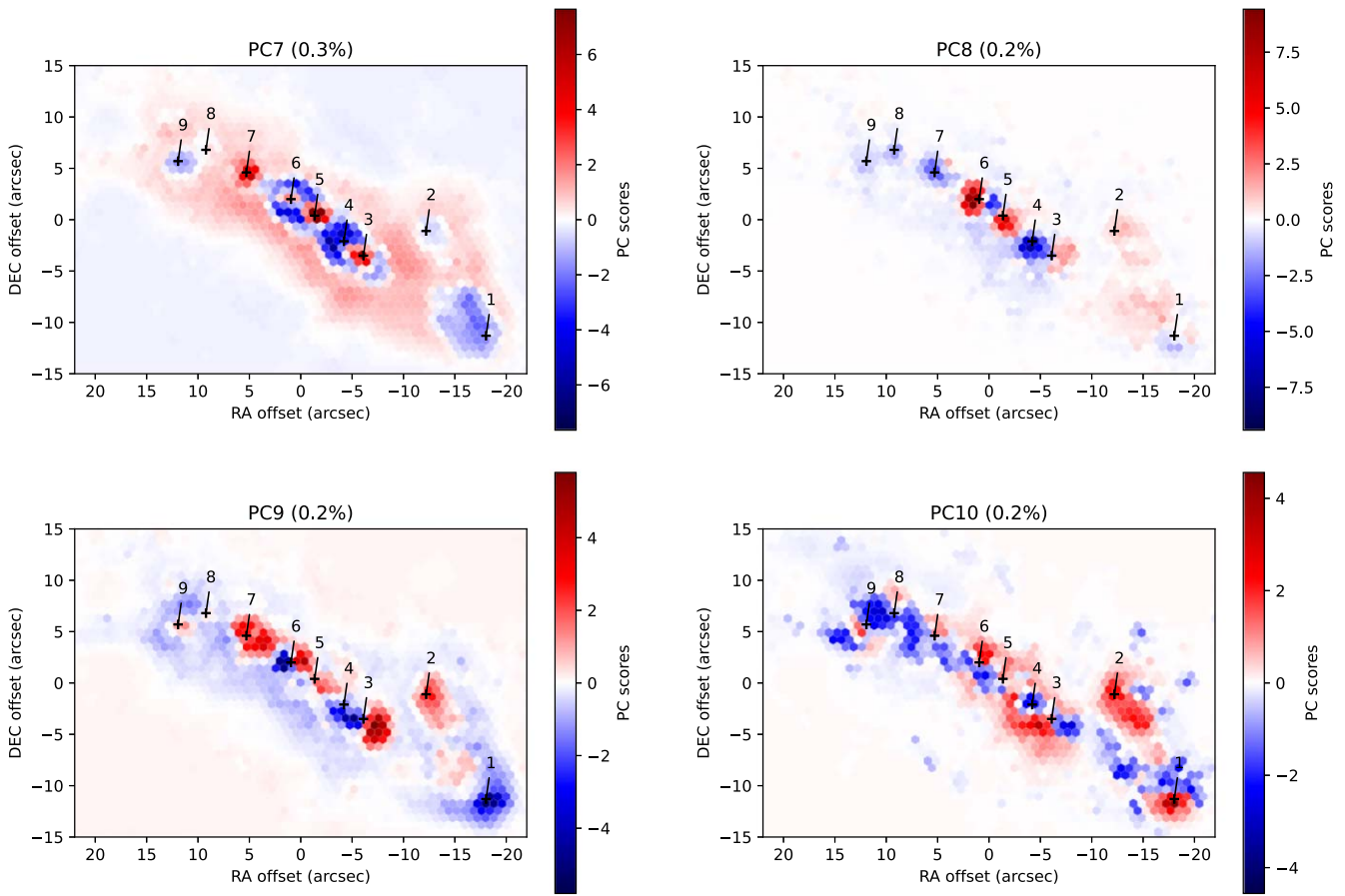


Figure 25. The same as Figure 24, but for PC7–PC10.

the second quadrant. It turns out that most transitions that appear in the second quadrant in Figure 36 also appear in the second quadrant of Figure 37. The transitions having this outflow feature are CO isotopologues, CCH(1–0), HOC⁺(1–0), and H₃O⁺. Although they are not shown in the figure, the dense gas tracers seen in an outflow (Southwest streamer) by Walter et al. (2017) such as HCN, HCO⁺, CS in $J=1-0$, and CN($N=1-0$) also have negative PC4 and positive PC5 coefficients. We note that CCH(1–0) has been detected also in the outflow in Maffei 2 (Meier & Turner 2012) and from an AGN in NGC 1068 (García-Burillo et al. 2017; Saito et al. 2022).

It is important to note that line intensities depend on column densities (or abundances), temperatures, and densities. Consequently, our results show very different PC coefficients, which means different distributions, even for the same species depending on transitions. This illustrates that caution is needed when using a particular species as a tracer of certain phenomena simply by observing a single transition.

4.6. Similarities between Species

The similarity between a pair of transitions can be evaluated by the correlation coefficient of their integrated-intensity maps, or the relevant element of the matrix Σ used for the PCA.³² Figure 38 shows the correlation coefficients (or similarities) between a reference transition and other transitions, for reference transitions of ¹²CO(1–0), HC₃N(37–36),

CH₃OH(2_K–1_K) at 96.741 GHz, and H39 α . The transitions highly correlated with ¹²CO(1–0) are other transitions of CO isotopologues, $J = 1-0$, or $N=1-0$ transitions of HCN, HCO⁺, CN, and CCH, and CS(2–1) (Figure 38). These transitions are all ubiquitous in translucent ($n \sim 10^3 \text{ cm}^{-3}$) molecular gas. On the other hand, the transitions that have similar distributions as that of HC₃N(37–36) are highly excited. The examples are high-excitation transitions of other HC₃N, sulfur-bearing species (rarer isotopologues of CS and SO, H₂S), SiO, and CH₂NH. Some of these transitions are known to trace shocks (SiO), but others are considered as hot core tracers. The transitions that are strongly correlated with CH₃OH(2–1) are low-excitation transitions of HNCO, HOCO⁺, and OCS(8–7). Methanol and HNCO are both known slow shock tracers, and HOCO⁺ is shown to be enhanced in shocks in NGC 253 due to the ice sputtering of CO₂ (Harada et al. 2022). OCS may also be enhanced in shocks if OCS is a major constituent of ice. H39 α , other RRLs, and the 3 mm continuum are all very strongly correlated, all of which are known to be related to star formation. High-excitation radicals such as HOC⁺(3–2), CN(3–2), CCH(4–3) are also highly correlated with RRLs. These species are radicals, and are abundant in PDRs or cosmic-ray-dominated regions.

4.7. GMCs in Principal Components

Figure 39 shows the nine GMCs in their scores of PC1 through PC5. We measured the PC scores from the hexagonal pixels at the GMC positions. Each panel has dashed lines at the PC score of zero to indicate the mean score of the entire CMZ.

³² We also make the correlation matrix among all the transitions and continua available at http://github.com/nanaseharada/alchemy_pca.

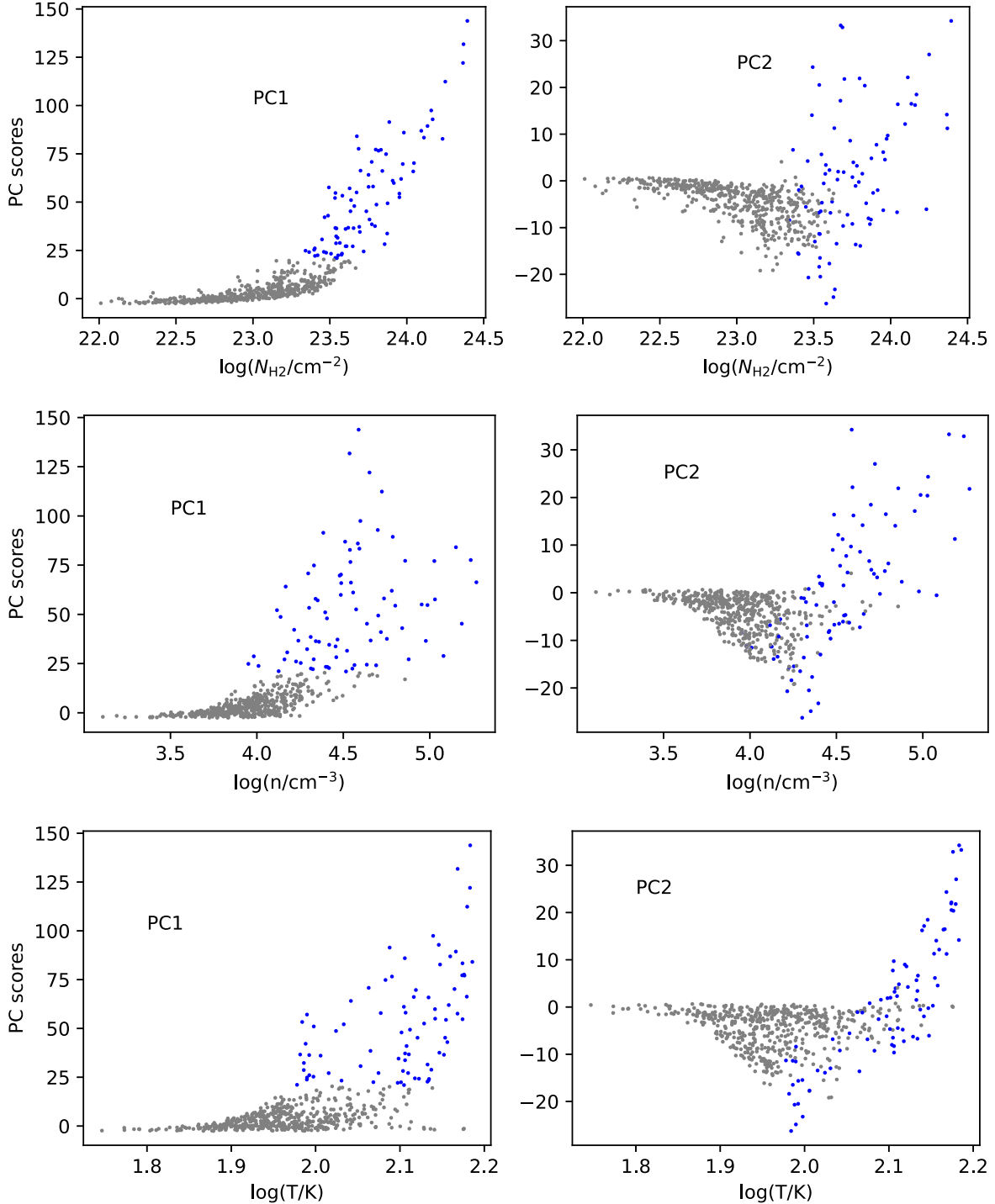


Figure 26. Physical parameters (top, column densities; middle, volume densities; bottom, temperatures) and PC scores in individual hexagonal pixels. Physical parameters are taken from “high-HB” results from Tanaka et al. (2024), which are the ones derived from species with relatively high critical densities. Gray points represent data points that lie within one standard deviation of PC1 scores from zero, pixels with low signal-to-noise ratios.

All GMCs have positive PC1 scores since the GMCs are emission peaks by definition, and the PC1 score reflects the overall strength of the emissions, approximately the ISM column density, at each position. PC2–PC5 are defined to be orthogonal to PC1. Therefore, they disregard the effect of overall emission strengths or ISM quantity and should only reflect the qualities of the ISM. The nine GMCs are clearly different in PC2–PC5. For example, they spread in the PC2–PC3 plane with the range of PC scores matching that in the

entire CMZ. Thus, the nine GMCs are distinct in their characteristics unrelated to their bulk emission strengths.

We categorized the GMCs into three groups on the basis of their PC scores using the k -means clustering method (KMeans class in the scikit-learn package). The k -means method is one of the simplest methods of categorization of data points into a desired number of clusters. This algorithm minimizes the following quantity: $\sum_{i=1}^k \sum_{z \in S_i} |z - \mu_i|^2$, for a set of clusters $S = \{S_1, S_2, \dots, S_k\}$ where μ_i is a mean of a set S_i

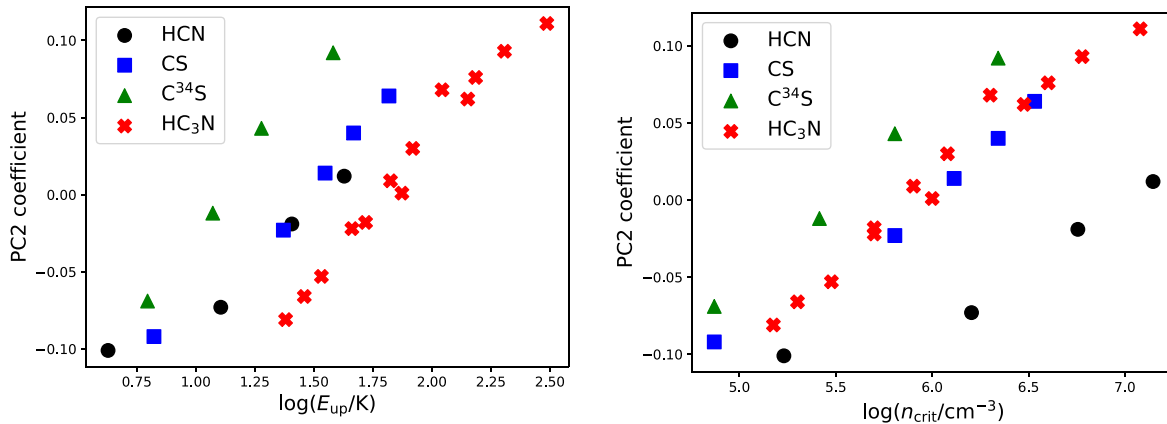


Figure 27. Comparisons between PC2 coefficients and (left) upper-state energies and (right) critical densities from the bright linear rotors, where the reasonable connection between J , E_{up} , and n_{cr} is expected. For HCN and CS, values of critical densities are taken from Shirley (2015) considering multiple levels. We assume the same critical densities as CS for C^{34}S . We take values of critical densities from Wernli et al. (2007) for HC_3N .

(MacQueen 1967), that is, the sum of a square of a distance between a data point and a cluster mean for each data point. Computationally, this minimum is found by (1) randomly assigning data points into clusters,³³ (2) calculating the center of mass within each cluster, (3) reassigning each data point into a cluster having the closest center of mass, and (4) iterating Steps 2 and 3 until it converges. In our case, the distances are Euclidean in the 5D PC space.

Using the cluster number of three based on the inspection of Figure 39, we categorized the nine GMCs into the groups of GMCs [1, 2, 7, 8, 9], [3, 6], and [4, 5] and refer to them as categories A, B, and C, respectively. This categorization indeed appears to correspond to physical differences between the GMCs. The first GMC category (A) contains the locations where Class I methanol masers have been detected, which indicates shocked locations. The second category (B) contains GMCs with relatively high intensities of complex molecules. The third category (C) has locations where RRLs are strong. We discuss in Section 5.3 that the difference between the second and third categories is likely attributed to the evolutionary stages of starbursts.

5. Discussion

5.1. Overall Gas Content and Star Formation

We suggest in Section 4.4 that PC1 is mostly associated with the molecular hydrogen column density. Figures 24 and 28 show that all transitions have positive PC1 coefficients (in the range of 0.042–0.091; see Table 4), which means that all transitions are correlated with the column density. Understandably, the molecular transitions are correlated with the total column densities because the emission is expected to be stronger where there is more molecular gas. RRLs should also somewhat correlate with the total column density because, when there is molecular gas, star formation is also expected in general (e.g., Kenicutt–Schmidt law; Kennicutt 1998). Although star formation and molecular gas content are not always cospatial depending on the GMC evolutionary stage and spatial resolution (e.g., Schinnerer et al. 2019), their correlation is relatively strong in the CMZ of NGC 253 where

³³ We use $k\text{-means}^{++}$, the default method in the KMeans class, where the initial assignment is not totally at random, but chosen so that the centers of mass are not close to each other.

its star formation is relatively young. We note that this strong correlation may also be attributed to the edge-on inclination of this target.

Although PC1 generally represents the overall molecular gas column density, transitions with the highest coefficients for PC1 are not what we expect given this relation. It is not $^{12}\text{CO}(1-0)$ that has the highest coefficients for PC1 among CO isotopologues; instead, these are the $J=3-2$ transitions of C^{18}O and C^{17}O . This may be partly because $^{12}\text{CO}(1-0)$ is optically thick, and does not trace the overall gas column density properly. If the optical depth is the major effect, PC1 appears to trace the overall molecular gas better than $^{12}\text{CO}(1-0)$. On the other hand, there is a factor that could cause deviation of PC1 from overall molecular gas. Many high-excitation or optically thin transitions or transitions from complex molecules show concentration on the central starburst regions with fewer transitions of optically thick, low-excitation, and extended transitions. That results in PC1 being biased toward central starburst regions, not purely indicating the total column density. Given the above factors, PC1 in general is a good tracer of overall molecular gas because many transitions have similar PC1 coefficients as C^{18}O and C^{17}O (3–2).

5.2. Dense Gas Tracers and Star Formation

Our PCA shows that PC2 is related to excitation (Figure 27). PC2 coefficients are positive and large for RRLs (Figure 29), which is also evident from the resemblance between the positive part of the PC2 score map (Figure 24) and moment 0 maps of RRLs. PC2 scores are the highest in the GMCs of category C (GMCs 4 and 5), and relatively high in category B (GMCs 3 and 6), as shown in Figure 39. They are GMCs with massive-star formation judging from the RRLs. In addition to RRLs, dense gas tracers with high upper-state energies ($\gtrsim 50$ K) also have large positive coefficients for PC2 (Figure 29). Meanwhile, their lower-excitation transitions (e.g., HCN $J = 1-0$) do not have such a strong correlation to RRLs (e.g., see their PC2 coefficients in Figure 29), and have negative PC2 coefficients comparable to the PC2 coefficients of CO isotopologues.

The correlation between star formation and low-excitation transitions with moderately high critical densities ($n_{\text{crit}} \sim 10^5 \text{ cm}^{-3}$ in an optically thin case, e.g., HCN $J = 1-0$) is not very tight in our study, although such a correlation has been

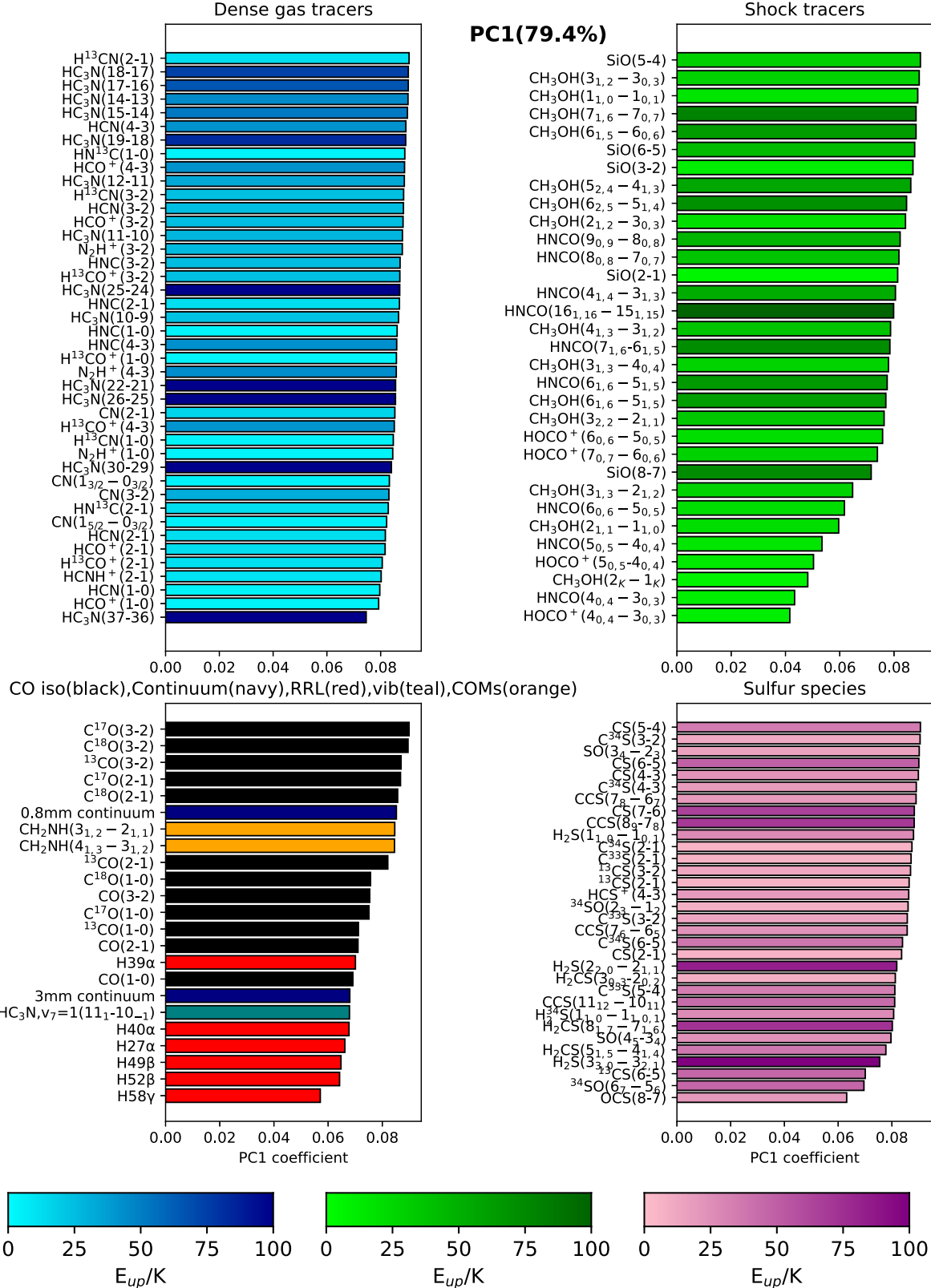


Figure 28. PC1 coefficients for selected transitions are shown in a descending order. For dense gas tracers, shock tracers, and sulfur species, upper-state energies are color-coded. Values from 0 to 100 K are shown from cyan to dark blue (dense gas tracers), from lime to dark green (shock tracers), and pink to purple (sulfur species). Colors of CO, continuum, RRL, vibrationally excited lines, and COMs indicate categories, not energies.

reported from extragalactic observations in a single-dish resolution (e.g., Gao & Solomon 2004). In fact, this correlation appears unlikely to be tight on <100 pc scale in general.

Galactic observations on the 1–10 pc scale (in Orion A, Orion B, W51, W33(OH), and Perseus) have already shown that HCN (1–0) does not trace only high-density regions, but can also

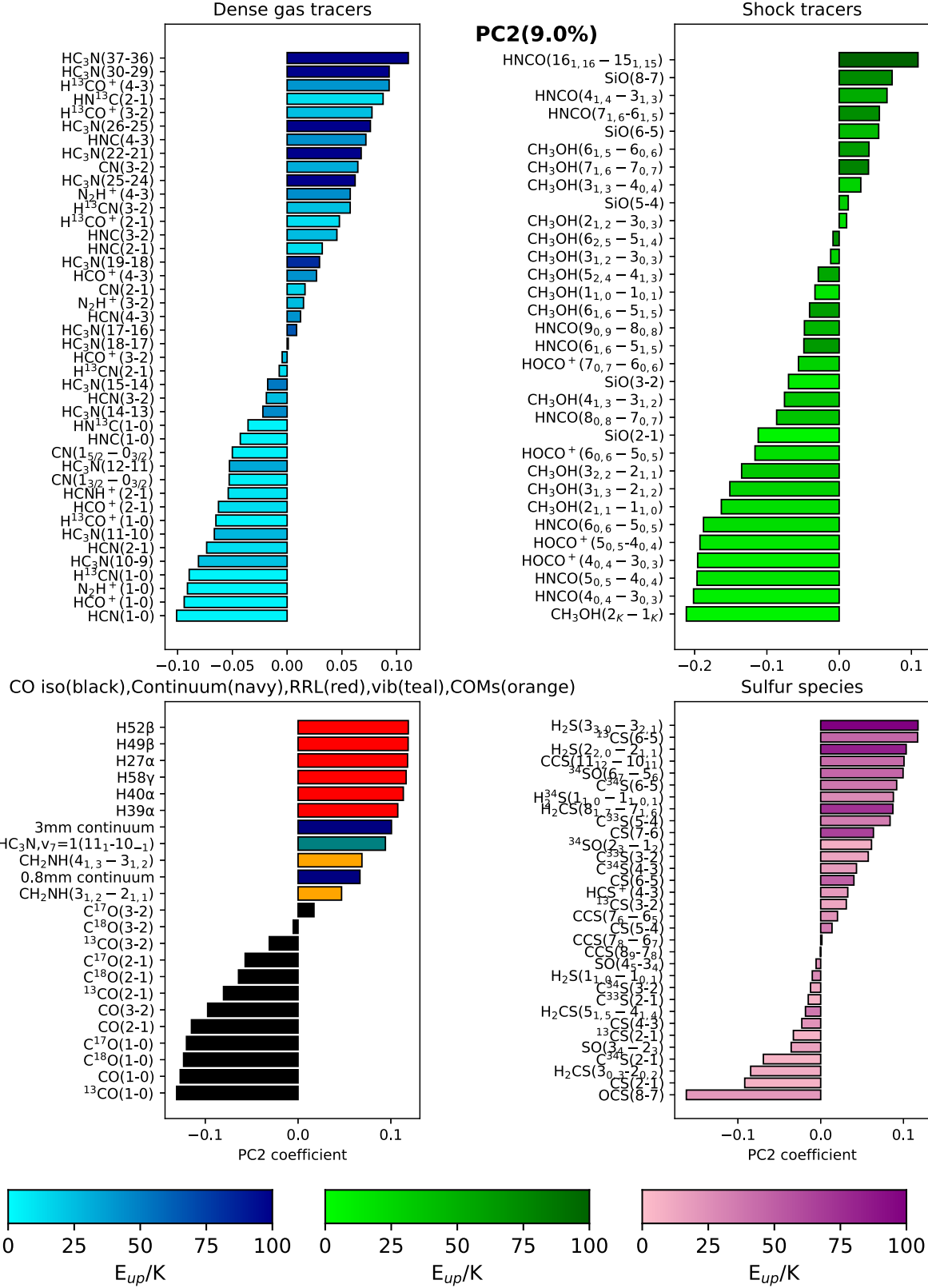


Figure 29. The same as Figure 28, but for PC2.

originate from translucent clouds ($n \gtrsim 10^3 \text{ cm}^{-3}$) (Kauffmann et al. 2017; Nishimura et al. 2017; Pety et al. 2017; Watanabe et al. 2017; Tafalla et al. 2021). This may be in conflict with the results by Wu et al. (2010) who claim that the correlation between the HCN luminosity and star formation rate does not break down

within $<100 \text{ pc}$. However, this difference may come from the fact that they focused on dense clumps where stars are already forming in the field of view of 4 pc on average. Although the mean mass-weighted density of the molecular gas in NGC 253 CMZ is $\sim 10^{3.5}-10^4 \text{ cm}^{-3}$ (Tanaka et al. 2024), higher than in the GMCs

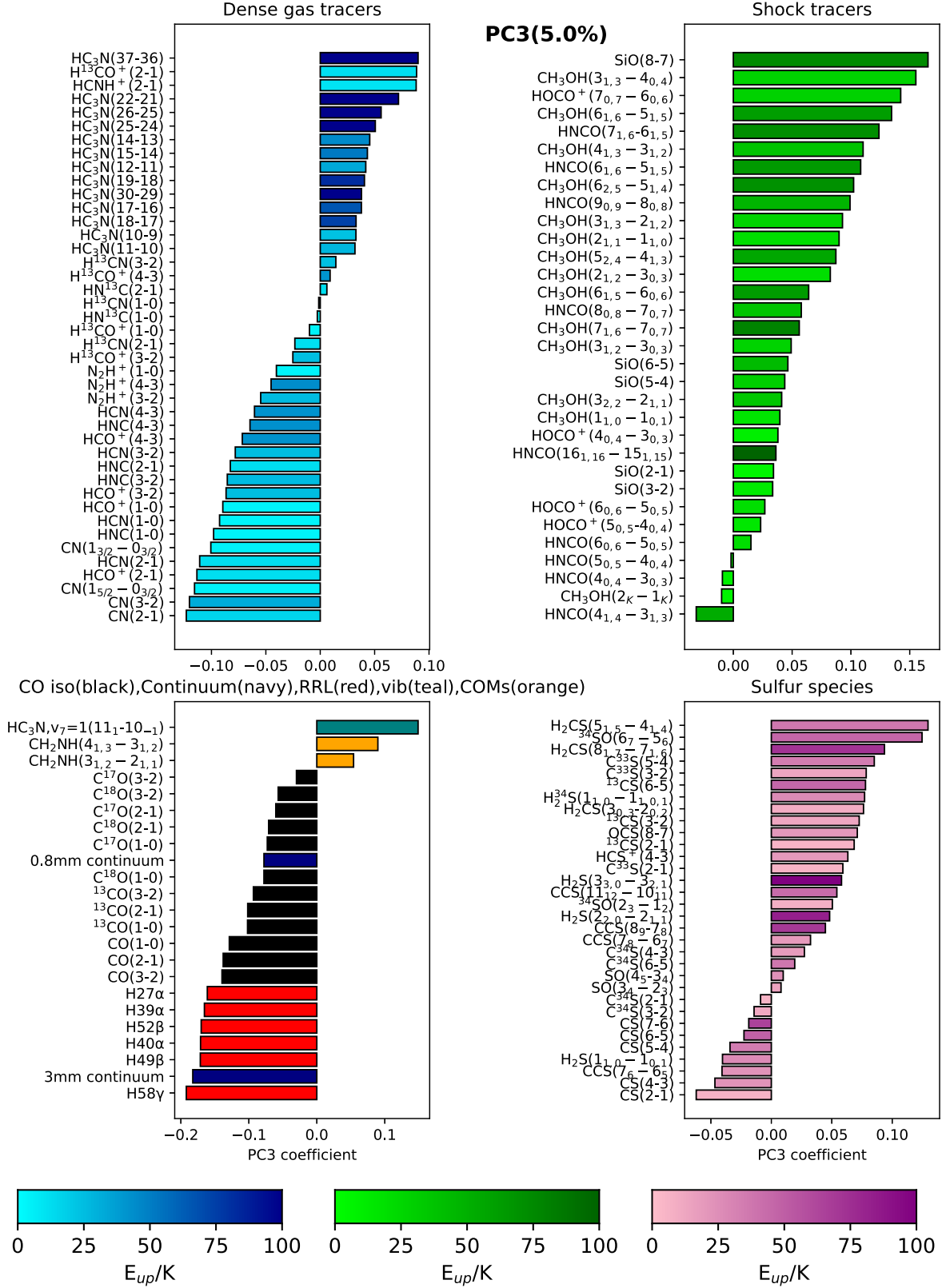


Figure 30. The same as Figure 28, but for PC3.

in the Galactic disk (10^2 – 10^3 cm $^{-3}$; Pety et al. 2017), the gas detected with low-excitation “dense-gas tracers” should be low enough in density not to immediately form stars within the timescale for the gas to orbit to different locations in our

observations. For example, it takes $\sim 10^6$ yr for a cloud to move 100 pc if it is moving with a velocity of 100 km s $^{-1}$, a few times the freefall time of a cloud with $n = 10^4$ cm $^{-3}$. Note, though, that the star formation threshold is likely higher in the CMZ of

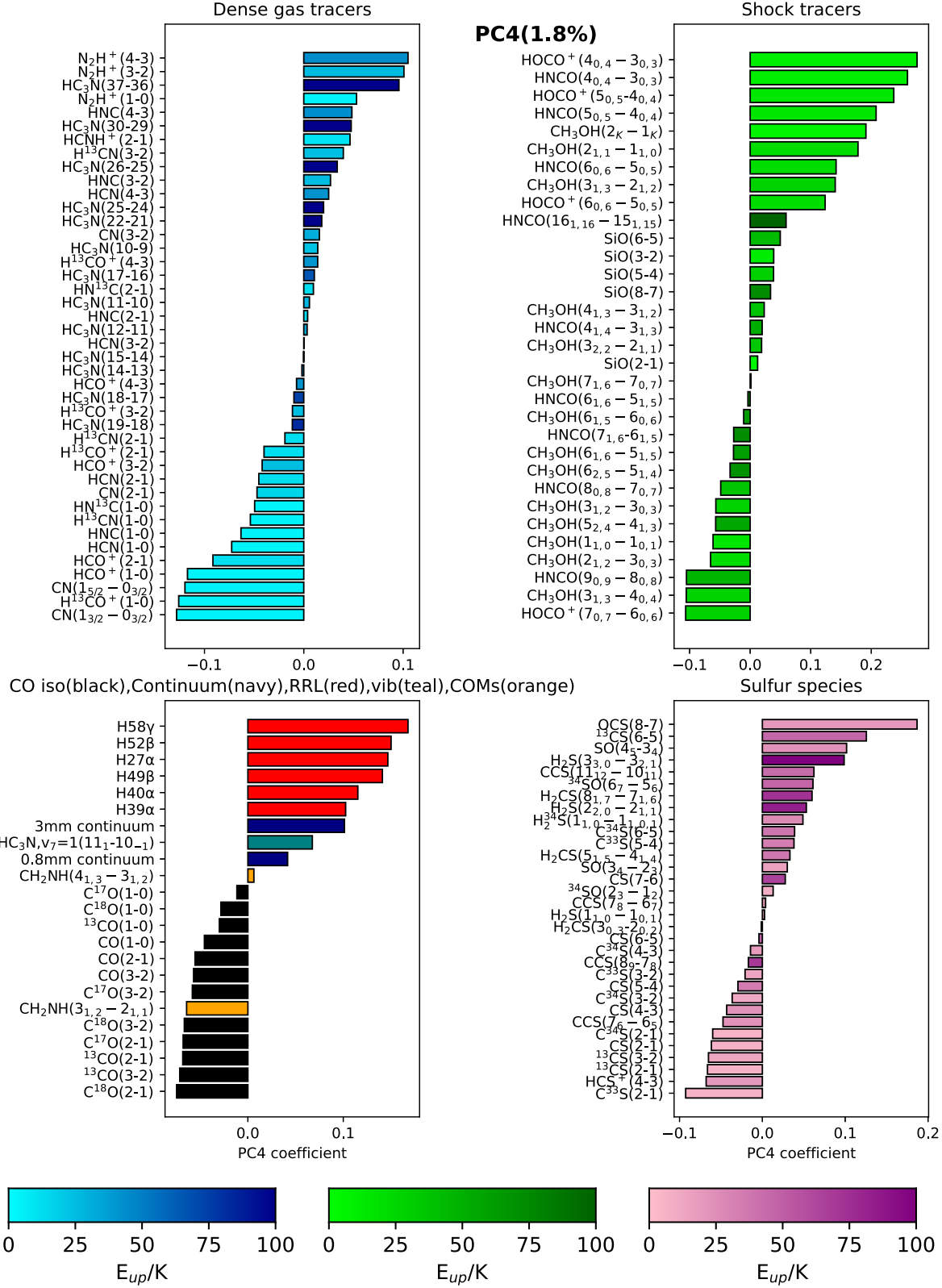


Figure 31. The same as Figure 28, but for PC4.

NGC 253 than that in the Galactic center and the Galactic disk (Tanaka et al. 2024).

The similarity between the high- J dense gas tracers and star formation has at least two possible interpretations. One is that dense gas is intimately related to star formation. Because star formation takes place in dense gas, this high-density gas traced

with high- J transitions may coexist with star formation. Alternatively, the high-excitation dense gas may have resulted from star formation. Star formation heats the gas, and the molecules around young stars may be more excited owing to the high temperature. The distinction between these two scenarios is discussed further in Section 5.3.

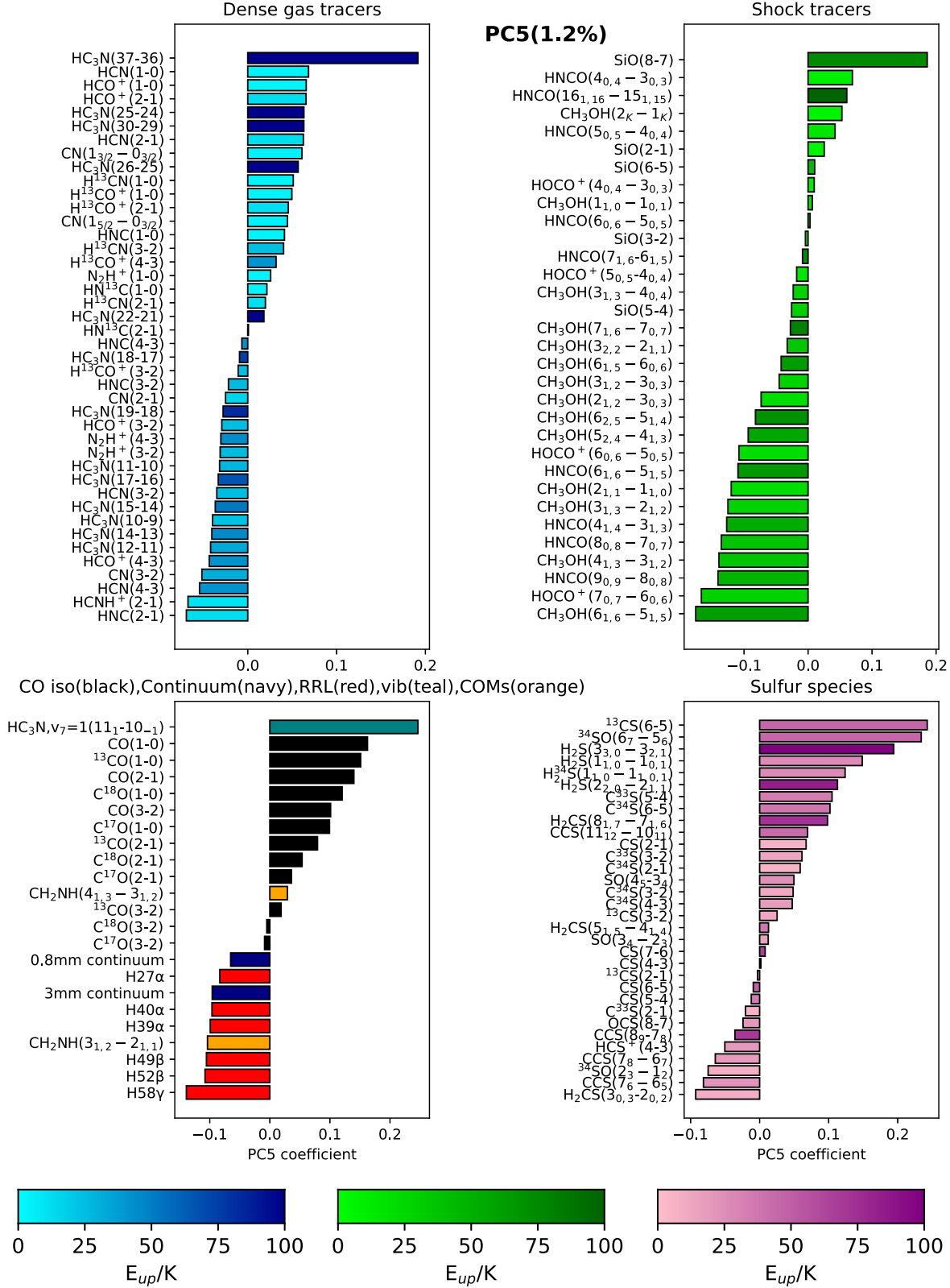


Figure 32. The same as Figure 28, but for PC5.

5.3. Evolutionary Stages of Proto-Super Star Clusters

There are some works reported on the evolutionary different stages among GMCs in the center of NGC 253, and it is of interest to see whether it has an impact on the physical and chemical properties that appear in our data. Rico-Villas et al.

(2020) showed different ages among these GMCs using the ratios between luminosities of protostars and zero-age main-sequence stars (ZAMS),³⁴ concluding that GMCs 3 (their

³⁴ This age estimation by Rico-Villas et al. (2020) applies to young clusters up to the ZAMS stage.

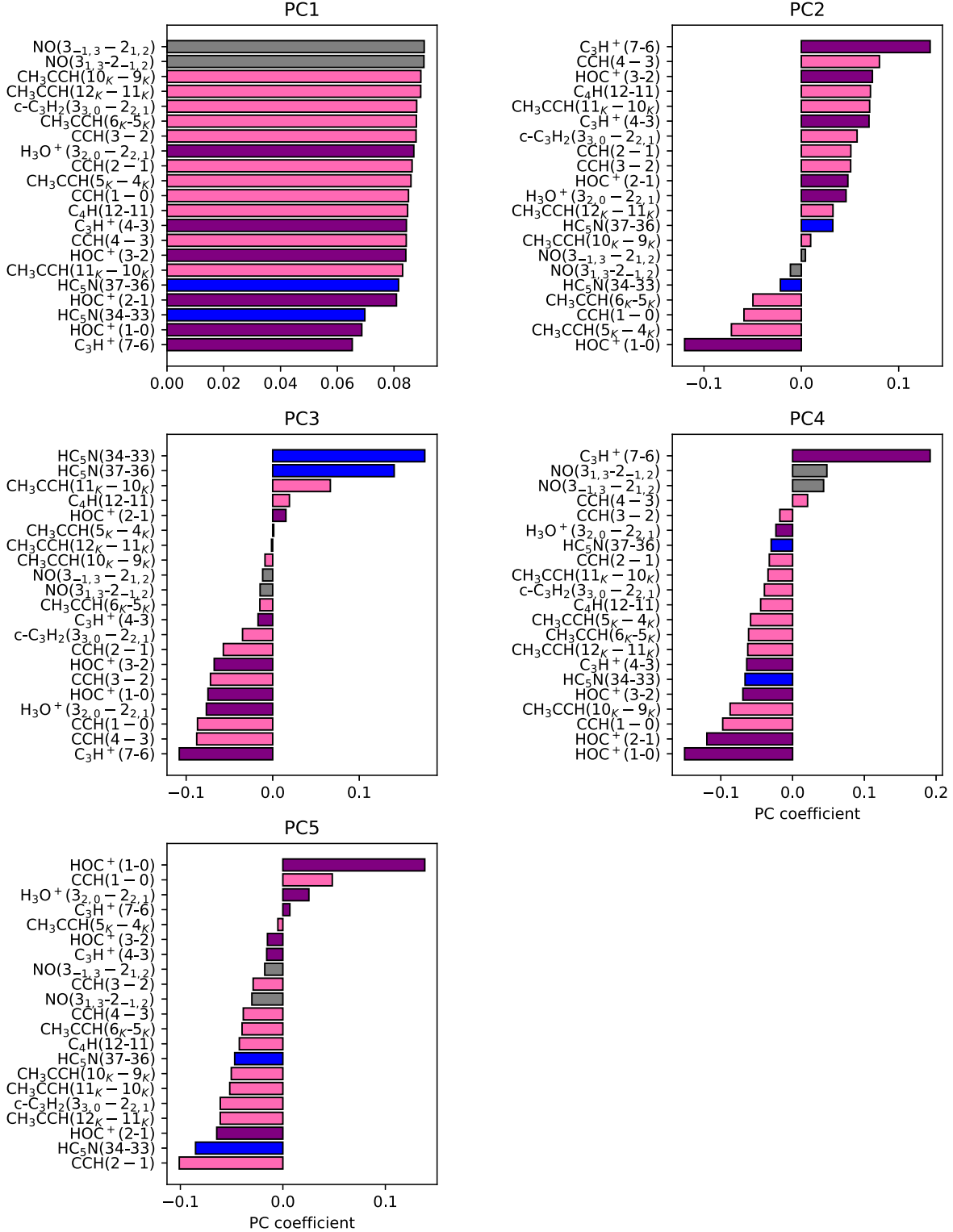


Figure 33. The same as Figure 28, but for PC1–PC5 of the rest of transitions. Dense gas tracers are shown with blue, reactive ions with violet, carbon chains with pink, and others with gray.

clusters 1, 2, and 3) and 6 (their cluster 14) have proto-super star clusters that are younger (proto-super star clusters $<10^5$ yr) than most of the stars in GMC 5 (their clusters 8–13; mostly ZAMS with $t_{\text{age}} = 10^5$ – 10^6 yr) although there are a couple of clusters that are young in GMC 5 (their clusters 8 and 13). Mills et al. (2021) also concluded that their clusters 1, 2, 3, 8, 13, and 14 (our GMCs 3 and 6, a part of GMC 5) are

younger than other clusters with the assumption that the stellar mass to dust mass ratios increases with age.

The literature above indicates that GMCs in category B defined in Section 4.7 host younger proto-super star clusters, while GMCs in category C are more developed clusters (GMCs 4 and 5). It is therefore natural to suspect that the evolutionary stages of SSCs alter chemical characteristics in GMCs. The difference that

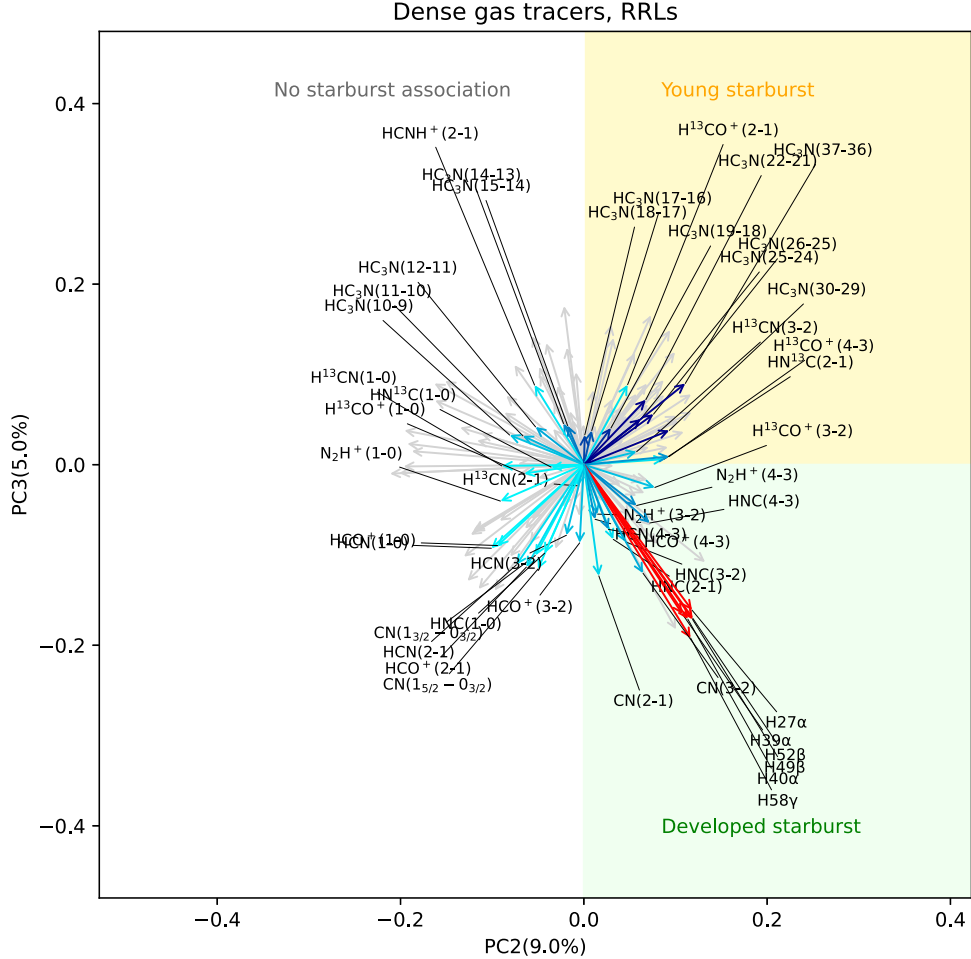


Figure 34. PC2 and PC3 coefficients are shown in abscissa and ordinate, respectively, for dense gas tracers and RRLs. Other transitions are also shown as gray arrows. Arrow coloring is the same as in Figure 28. Transitions in the first quadrant (filled with light yellow) are distributed near young starbursts ($<10^5$ yr) while transitions in the fourth quadrant (filled with light green) are near well-developed starbursts ($>10^5$ yr) as discussed in Section 5.3.

appears in PC3 likely contributes to these characteristics in the PC score categorization. Positive PC3 scores seem to trace GMCs that have relatively young star formation (because its tracers have positive coefficients for PC3 as seen in the first quadrant of Figure 34). There, the relatively large molecules like cyanopolyynes (HC_{2n+1}N), in particular vibrationally excited lines, are bright. PC3 is also positive in GMC 3, where Rico-Villas et al. (2020) show the youngest clusters. Meanwhile, negative PC3 values likely trace more well-developed star formation (the fourth quadrant of Figure 34). GMC 5 and a part of GMC 4 have negative PC3 scores, and they contain more developed star formation ($>10^5$ yr).

We note that the age sequence proposed by Rico-Villas et al. (2020), Mills et al. (2021) is not consistent with that reported by Krieger et al. (2020), who assumed that the HCN/HC₃N ratios decrease with evolutionary stage owing to the increasing density. Instead, their HCN/HC₃N intensity ratios in the 1 mm band tend to be higher in GMCs 5 and 6. We argue that the HCN/HC₃N ratios may not follow the same stages as those measured by Rico-Villas et al. (2020). Krieger et al. (2020) used the HCN/HC₃N ratios to estimate the ratios between the very dense gas and the dense gas. This ratio likely increases as a molecular cloud evolves to form stars, but it is unclear if the density continues to increase after stars form. In addition, the age differences among all the super star clusters in NGC 253

CMZ may not be enough to cause chemical differentiation as already noted by Krieger et al. (2020).

These young and more developed starbursts embedded in the gas are characterized by different chemistry. In GMC 6, high-excitation transitions of cyanopolyynes (HC₃N and HC₅N), CH₂NH, and shock tracers have high intensities. On the other hand, in GMC 5, there are high intensities of high-excitation transitions of CN and CCH. These features can be attributed to differences in shock strengths/frequencies and/or the presence of hot molecular cores or PDRs. Embedded young starbursts may encounter a stronger influence from the interaction between the starburst and its surrounding medium, which causes shocks. Cyanopolyynes and CH₂NH may also be enhanced from the ice sublimation from shocks. Dense and hot molecular cores heated from star formation can also increase the abundances of cyanopolyynes, CH₂NH, and methanol. These GMCs are hot and dense, having a similar environment as that of protostellar cores (*hot cores*), although individual protostellar cores are too small to resolve in our beams. If shocks or hot molecular cores are the only cause of this chemical differentiation, it does not fully explain the strong correlation between high-excitation radicals (CCH 4–3, CN 3–2) and RRLs. Dense PDRs around GMC 5 may explain this trend as they can both increase the abundances of radicals and cause high excitation. Galactic PDRs around high-mass star-forming regions (e.g., Taniguchi et al. 2022) show decreased

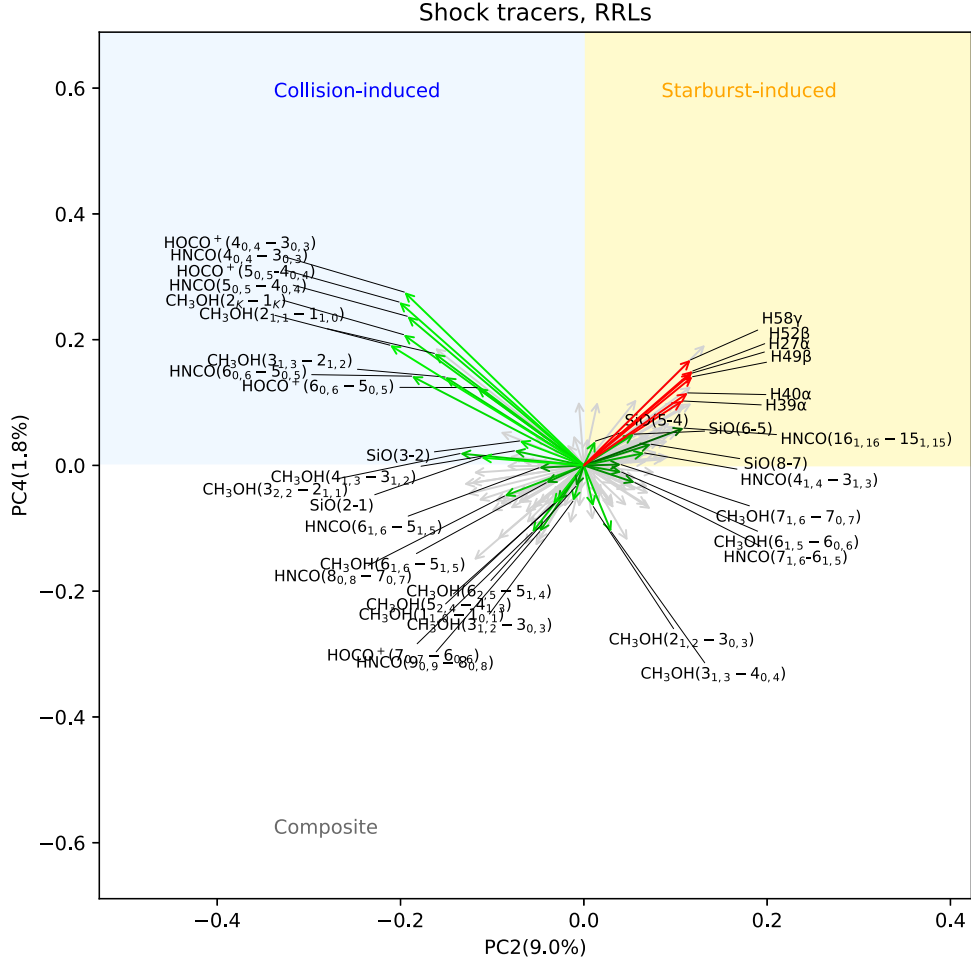


Figure 35. Same as Figure 34, but showing PC2 and PC4 for shock tracers.

abundances of cyanopolyynes likely due to photodissociation. While low-excitation CN and CCH can be emitted from extended low-density gas or cosmic-ray dominated regions, we suggest that higher-excitation transitions such as CCH(4–3), CN(3–2), HOC⁺(3–2) may be relatively uncontaminated tracers of PDRs in the vicinity of a starburst. Higher stellar-to-dust mass ratios in some clumps in GMC 5 seen by Mills et al. (2021) may support this scenario because GMCs with more ionizing sources (massive stars) per unit mass are capable of creating more PDRs within them.

There are possible arguments against the strong influence of PDRs. For example, Holdship et al. (2021, 2022) concluded that the total column densities of GMCs are extremely high ($N_{\text{H}} \sim 10^{24} \text{ cm}^{-2}$), and PDRs should not have significant contributions assuming that the media are largely uniform, and not clumpy; instead, radicals can be enhanced with high cosmic-ray ionization rates ($\zeta \gtrsim 10^{-13} \text{ s}^{-1}$). We note that the presence of PDRs, as previously claimed based on the detection of significant abundances of HOC⁺ and CO⁺ (Martín et al. 2009), does not necessarily exclude high cosmic-ray ionization rates. In fact, they are expected to be high in starburst galaxies, and we do not dispute that cosmic-ray ionization rates are in general much higher than that in the Galactic disk. Among the cosmic rays, lower-energy ones are attenuated even with low column densities while higher-energy cosmic rays are likely to influence a larger extent than the individual GMC scale. If there are cosmic-ray sources within GMCs, the cosmic rays can cause differences between individual GMCs. However, known

supernovae lie outside of GMCs (Ulvestad & Antonucci 1997). Therefore, cosmic rays are unlikely to account for chemical differences among GMCs shown in this work. Moreover, cosmic rays have stronger influences in lower-density regions because the chemistry roughly scales as ζ/n , and molecules can be dissociated with extremely high cosmic-ray ionization rates ($\zeta \gtrsim 10^{-13} \text{ s}^{-1}$). One needs a reasonable explanation for the wide-spread presence of CO in low-density regions ($n \sim 10^3 \text{ cm}^{-3}$) if the cosmic-ray ionization rates are that high over a large extent. Therefore, we suggest that PDRs can be a main driver of chemistry in some regions even if cosmic-ray ionization rates are also high.

How feedback is acting in these GMCs is an interesting question. Simulations have modeled quenching mechanisms of star formation in GMCs. Stellar feedback may include UV, optical, and infrared radiation pressure, stellar winds, supernovae, photoionization, and photoelectric heating (Grudić et al. 2018). Photoionization feedback may be important in low-column-density clouds, but not in high-column-density clouds (Fukushima & Yajima 2021). Radiation pressure may instead be more important in many cases (Grudić et al. 2018). Therefore, the incident radiation field producing the PDR-like emission characteristics that we see in our results may not directly measure the total feedback strength. In other words, a larger degree of feedback may be acting in young embedded proto-super star clusters (e.g., Levy et al. 2021) than in clusters showing PDR-like features. However, we expect such PDRs when molecular clouds are already disrupted by feedback, and

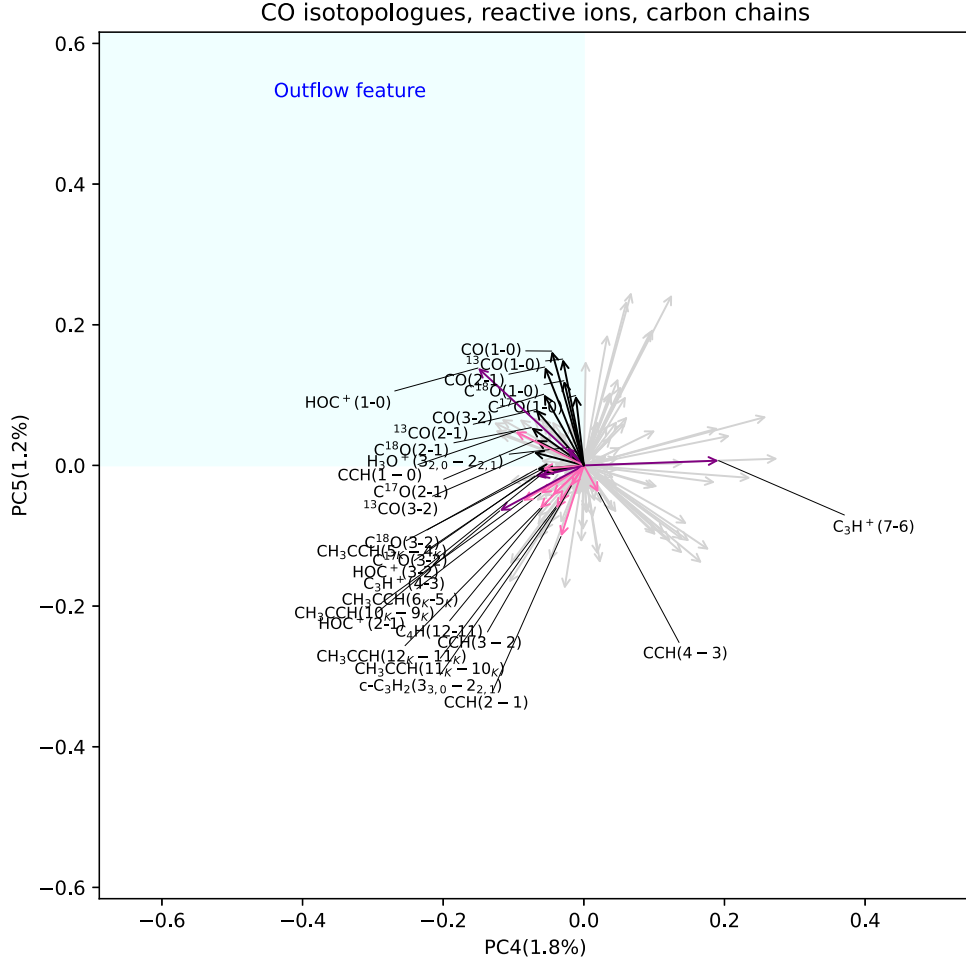


Figure 36. Same as Figure 34, but showing PC4 and PC5 for CO isotopologues, reactive ions, and carbon chains. Arrows show CO isotopologues in black, ions in violet, and carbon chains in pink. Transitions with outflow-like features should lie in the quadrant marked with light blue as discussed in Section 4.5.

UV photons can travel spatially farther away than when they are embedded (e.g., the ISM is made more porous).

We note that a strong continuum in GMC 5 (so-called “TH2” from Turner & Ho 1985) causes absorption features for some transitions such as $\text{H}^{13}\text{CO}^+(1-0)$, $\text{HC}^{13}\text{N}(1-0)$, and $\text{SiO}(2-1)$. The absorption features are not obvious for other transitions, and our PCA results are unlikely to be significantly affected. But this effect should be checked against higher-angular-resolution data.

5.4. Origins of Shocks and Relationship with Star Formation

The clustering analysis in the PC space found GMCs 1, 2, 7, 8, and 9 in the same group (category A, Figure 39). These are locations with detected Class I methanol masers (Humire et al. 2022), indicating the presence of shocks. Shocks are likely to be at intersections between orbits of the bar (x_1 orbits) and circumnuclear ring (x_2 orbits; Meier et al. 2015; Harada et al. 2022; Humire et al. 2022). The transitions that are enhanced in these regions are low- J transitions of CH_3OH , HNCO, and HOCO^+ , tracers of weak shocks. Although star formation could also cause shocks, it is unlikely to be causing shocks here because there is no obvious evidence of star formation. Meanwhile, these shocks or cloud collisions could promote future star formation through the compression of molecular clouds (e.g., Böker et al. 2008; Harada et al. 2019).

A well-known tracer of shocks, SiO, does not show strong enhancement near orbital intersections according to our result (e.g., PC2; Figure 29). High-excitation transitions of SiO (e.g., $J = 8-7, 6-5$) correlate relatively well with RRLs when PC2 and PC4 are considered (Figure 35). In addition to these SiO lines, some HNCO transitions are relatively well-correlated with RRLs. They are the $K_a \geq 1$ transitions of HNCO ($J_{K_a, K_b} - J'_{K'_a, K'_b}$), which Churchwell et al. (1986) suggested to be radiation-pumped, not collisionally pumped, in Galactic hot cores. For them to be radiation-pumped, a strong far-infrared radiation field needs to be present, which may come from embedded protostars. If these HNCO $K_a = 1$ transitions originate from protostars, they do not necessarily need shocks. It has been suggested that HNCO can be abundant near young protostars (Quan et al. 2010). We note here that these SiO and HNCO transitions are similar to RRLs in contributions to PC2 and PC4, but not to PC3. This trend implies that these transitions are associated with younger starbursts, not developed ones (Section 5.3).

High- J SiO transitions appear to be the only transitions of shock tracers that are centrally concentrated, if HNCO $K_a = 1$ transitions are not related to shocks. This trend suggests the prevalence of strong shocks in the central regions. One has to be careful making this conclusion because we did not image high- J HNCO transitions ($J > 10$) due to the contamination criteria discussed in Section 2.2, but the contamination to these

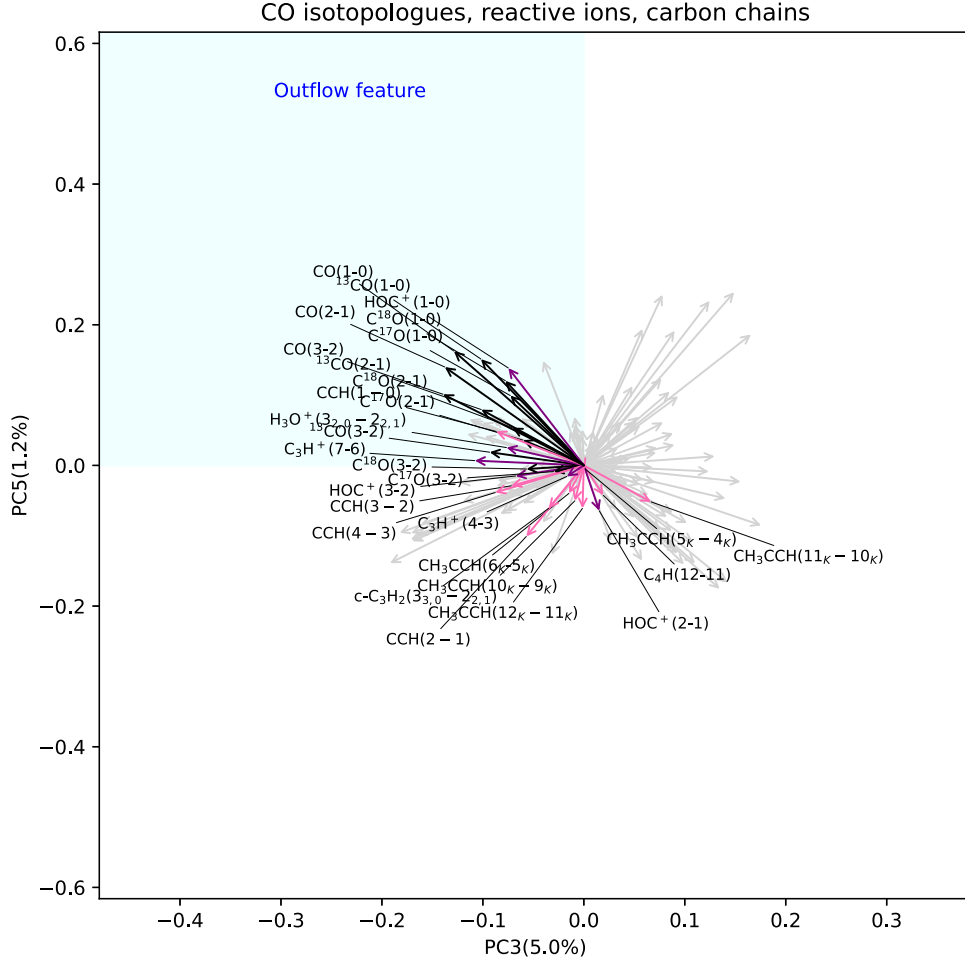


Figure 37. Same as Figure 36, but showing PC3 and PC5. Transitions with outflow-like features should lie in the quadrant marked with light blue as discussed in Section 4.5. These transitions are the same as ones in the second quadrant in Figure 36 except for $\text{C}_3\text{H}^+(7-6)$.

transitions from neighboring transitions does not seem very severe except for $J=12$ (Huang et al. 2023). However, it seems also true that SiO is more concentrated around the starburst regions, GMCs 4–6, compared with CH_3OH , HNCO, and HOCO^+ of similar upper-state energy levels. The only exception to it is when the low- J SiO line is affected by absorption against a strong continuum source. A large velocity gradient analysis by Huang et al. (2023) found that SiO/HNCO column density ratios are higher in GMCs 4 and 6 compared with those in GMCs 3 and 7 although this difference is not significant considering errors, and there are some in the outskirts (GMCs 2 and 9) that have high SiO/HNCO ratios as well. Note that they did not model GMC 5 because of the self-absorption. It is not clear whether fast shocks are more dominant than slow shocks in this central starburst region as Huang et al. (2023) concluded, but there are indeed strong shocks near the starburst regions.

What are the origins of the shocks that caused the high- J SiO line emission near the central starbursts? One scenario is again cloud collisions. Levy et al. (2022) suggested another x_2 orbits connecting GMCs 3–6 in addition to the larger one shown in Figure 1. If this orbit crosses with some x_1 orbits, cloud collisions could occur. However, features from such cloud collisions should appear in GMCs 3 and 6 where x_1 orbits likely cross with the inner x_2 orbits instead of GMCs 4–6. Another explanation is that the medium in NGC 253 CMZ is in general turbulent, and high-excitation transitions are seen

simply because the gas is excited near the starbursts. This scenario is hard to exclude, but it does not solely explain variations among SiO and other shock tracers. The other cause of shocks is the starburst itself. Cluster-scale outflows have been found in high-angular-resolution observations through P-Cygni profiles in GMCs 4 and 6 (Levy et al. 2021) and through broad line wings of $\text{H40}\alpha$ in GMCs 4 and 5 (Mills et al. 2021). Therefore, outflows from young stellar objects may cause strong shocks, which yield high-excitation SiO emission. In addition to such cluster-scale outflows, fast shocks are common around young massive stars from stellar winds. We consider this starburst-induced shock scenario is most plausible for now because of the signatures of outflows, but this claim is still speculative.

5.5. Vertically Extended Structures Likely Associated with Outflows

Outflows on the galactic scale have been detected in the center of NGC 253 in previous studies, and some of them contribute to the vertically extended structures or emission at high galactic altitudes seen in PC4 and PC5 (Turner 1985; Bolatto et al. 2013; Walter et al. 2017; Krieger et al. 2019). In Section 4.5, we show that CO isotopologues, J or $N=1-0$ transitions of HCN, HCO^+ , CN, CS, CCH, HOC^+ , and $\text{H}_3\text{O}^+(3_{2,0}-2_{2,1})$ have emission in this structure. Among them, HOC^+ (Figure 10) and H_3O^+ (Figure 20) have relatively weak overall intensities but still show this extended structure. This is

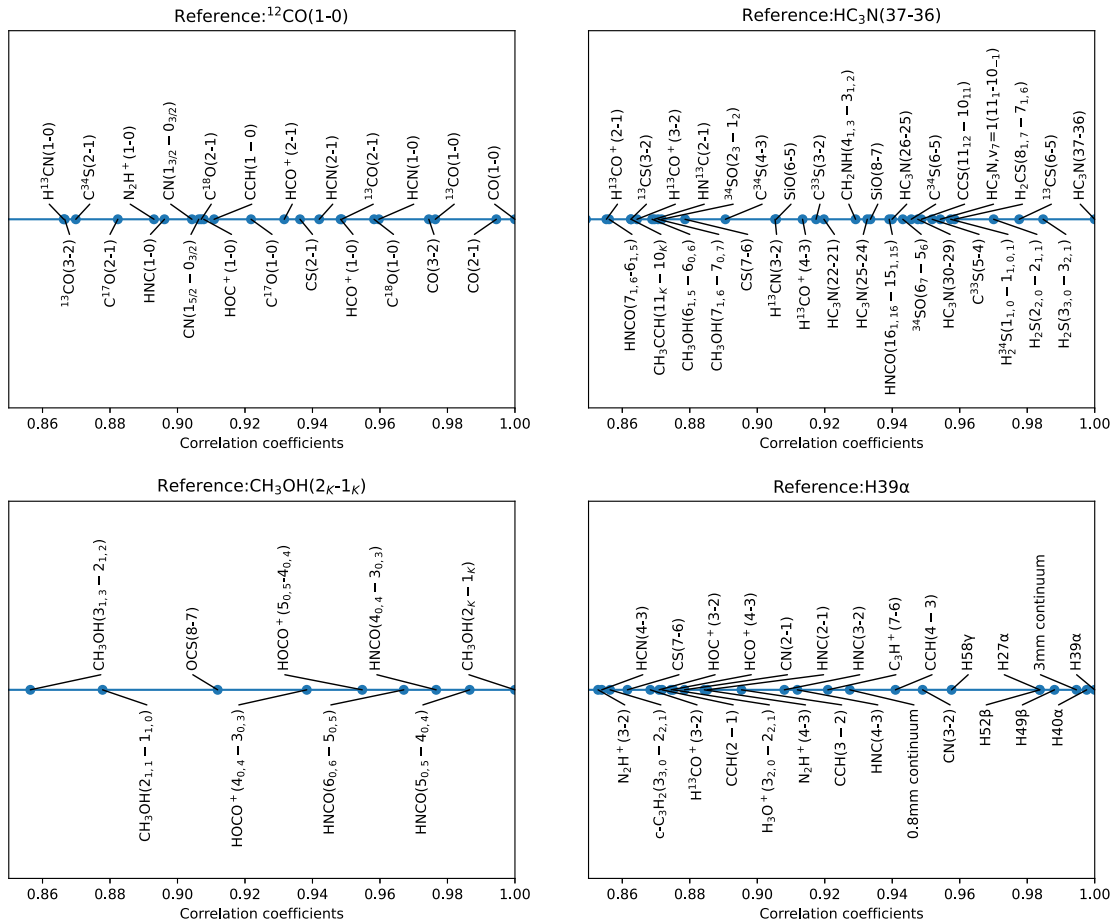


Figure 38. Covariance between reference transitions and other transitions. The reference transitions are $^{12}\text{CO}(1-0)$ (top left panel), $\text{HC}_3\text{N}(37-36)$ (top right panel), $\text{CH}_3\text{OH}(2K-1K)$ (bottom left panels), and $\text{H}39\alpha$ (right panels). Transitions that appear close to 1 have similar distributions as that of the reference transition.

likely because these species are reactive ions that are enhanced by strong UV radiation or cosmic rays (Harada et al. 2021; Holdship et al. 2022). This result suggests a high ionization degree in these outflows.

In general, there are multiple possible mechanisms creating starburst-driven and AGN-driven outflows such as thermal energy, radiation, cosmic rays, and radio jets (Veilleux et al. 2020). While our observations do not suggest which mechanisms are most effective in producing energy, they do suggest an influence of cosmic rays because H_3O^+ is preferentially enhanced with cosmic rays compared to UV photons (Holdship et al. 2022).

5.6. Comparisons with Other PCA Studies

We compare our study with previous image-based PCA studies conducted for nearby galaxies (Meier & Turner 2005, 2012; Chidac 2020; Saito et al. 2022) and Galactic molecular clouds (Ungerechts et al. 1997; Gratier et al. 2017). Comparisons are not necessarily straightforward because the number of molecules and transitions in this work is unprecedented. The results of PCAs are affected by the transitions used, their intensities, and the normalization method. In addition, the field of view and angular resolutions are different in all studies. Here, our discussion takes these factors into consideration. Similar to our results, most studies found positive PC1 coefficients for all input variables used in PCA, except for Saito et al. (2022). This is because they used not only molecular transitions or continuum but also other quantities such as the [S III]/[S II] ratio and [CI]

intensity that do not necessarily trace the overall molecular content. Note also that Gratier et al. (2017) showed that the interstellar radiation field anticorrelates with all the molecular emission intensities.

Meier & Turner (2005) observed the center of the modest starburst galaxy IC 342, with a similar field of view and twice larger beam size (50 pc) in comparison with those of our study. They used $^{12}\text{CO}(1-0)$, $\text{C}^{18}\text{O}(1-0)$, CCH , $\text{C}^{34}\text{S}(2-1)$, $\text{N}_2\text{H}^+(1-0)$, CH_3OH , HNCO , HNC , $\text{HC}_3\text{N}(10-9)$, SO , and continuum in the 3 mm band. Their study shows that CH_3OH and HNCO emission also peaks at the outskirts of the CMZ, and has a high absolute value in their PC2. This is in agreement with our study; high-excitation transitions have high absolute values of PC2 while CH_3OH and HNCO have the opposite sign. In the 3 mm band observations of Meier & Turner (2005), there were no such high-excitation transitions. Instead, C^{34}S and CCH showed different degrees of contribution in PC2 from CH_3OH and HNCO coming from high-column-density regions (C^{34}S) or PDRs (CCH). In our study, these transitions have somewhat different coefficients for PC2 compared to CH_3OH and HNCO , but the difference is not as large as for the high-excitation transitions. Similar results are found by Meier & Turner (2012) in Maffei 2.

In the study of M82 by Chidac (2020), they used CCH , CN , CS , HCN , HCO^+ , HNC , and ^{13}CO in the 3 mm band. Because of the limited number of transitions, ^{13}CO and other transitions had different contributions to PC2 likely because of the difference in the critical densities.

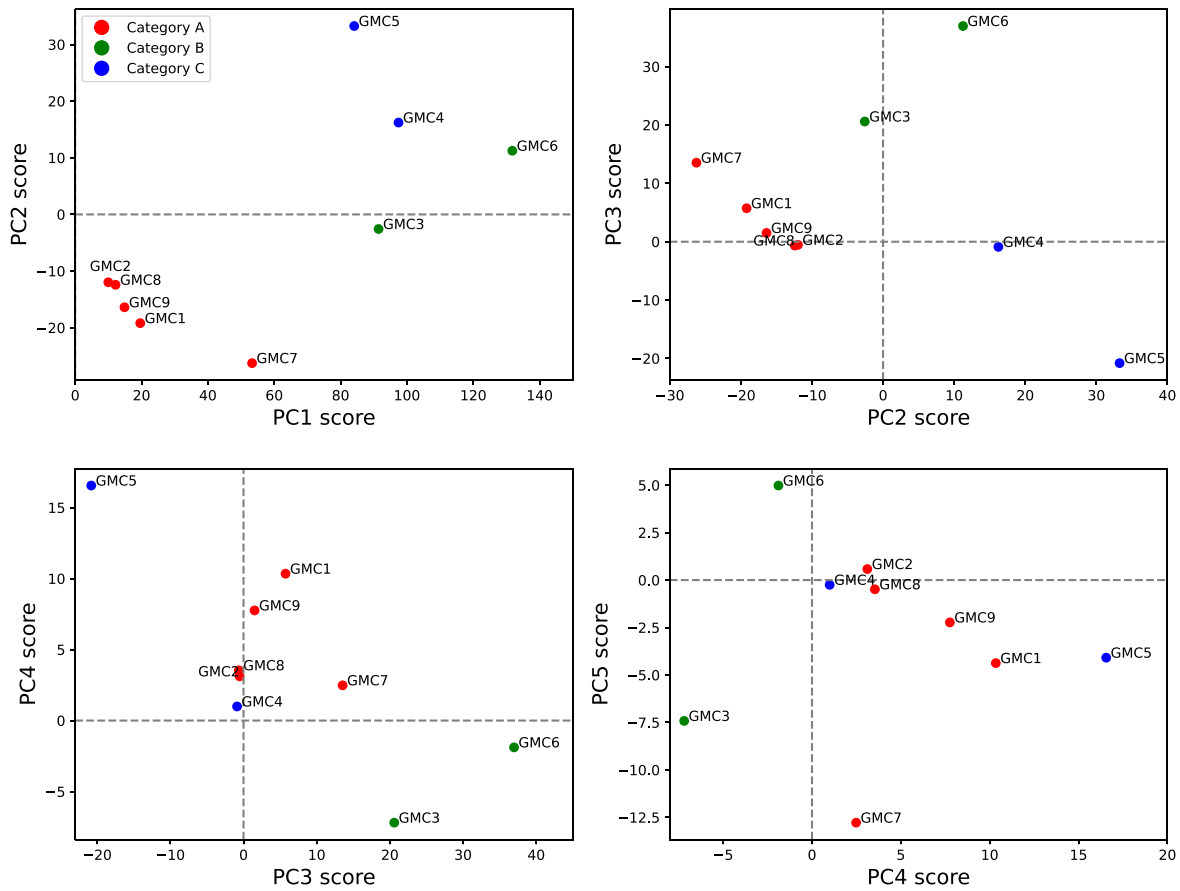


Figure 39. PC scores in GMCs. Different colors show three different groups categorized with the k -means clustering method. Each category is referred to as A (red), B (green), and C (blue) in the text.

The nature of PCA in Saito et al. (2022) is quite different from ours in the sense that they focused on the region around the AGN in NGC 1068. They used 16 transitions in the 3 mm band line survey together with [C I] and [S III]/[S II] ratio from archival data. They separated out the circumnuclear disk in PC1 and the AGN-driven outflow in PC2. In their result, CN, HNC, and CCH showed a high contribution from the outflow while N_2H^+ , HC_3N , and CO isotopologues show the opposite trend according to the categorization from PC2. In our result, CN, HNC, and CCH also have outflow features, but so do the CO isotopologues, HCN, and HCO^+ .

Ungerechts et al. (1997) mapped the Orion BN-KL regions with ^{12}CO , CS, HCN, HNC, HCO^+ and their ^{13}C isotopologues, C^{18}O , C^{34}S , N_2H^+ , CN, CCH, HC_3N , CH_3CCH , C_3H_2 , SO, and CH_3OH . Because their line widths are much narrower than ours, their observations spectrally resolved hyperfine structure lines of N_2H^+ and various K -ladders of CH_3CCH . Their field of view is at the parsec scale with the beam size of 0.1 pc and so is qualitatively different from the extragalactic studies. Their results separate among transitions enhanced near the high-mass star-forming regions of BN-KL such as HC_3N and CH_3OH , ones enhanced around the ridge such as CS and CN, and ones enhanced near a relatively cold cloud such as N_2H^+ . This distinction is not obvious in our result. One reason may be the difference in spatial resolution. Our 27 pc beam is not small enough to separately resolve dense clouds and star-forming regions within a GMC. Another reason may be that the difference between dense clouds and star-forming regions is better highlighted in our study by the difference between higher- J HC_3N and N_2H^+ rather than $\text{HC}_3\text{N}(10-9)$ and N_2H^+ .

in the 3 mm band. It is also important to note that NGC 253 contains more extreme star formation compared with Orion-KL.

Gratier et al. (2017) conducted a PCA study using maps of ^{12}CO , ^{13}CO , C^{18}O , CS, HCN, HCO^+ , SO, CN, HNC, CCH, N_2H^+ , and CH_3OH in the Orion B molecular cloud with the linear resolution of 0.05–0.07 pc covering the area of $\sim 6 \times 8$ pc. In addition to these line intensities, they also examined the correlation between these molecular line emission intensities and logarithms of the H_2 column density N_{H_2} obtained from dust continuum flux, volume density n_{H} from the dust mass and core sizes, and UV radiation field normalized by the mean value U/\bar{U} from polycyclic aromatic hydrocarbon emissivity. Their coefficients for PC2 show a large difference between N_2H^+ or CH_3OH versus CO isotopologues. This is likely due to the difference in the density and temperature as N_2H^+ and CH_3OH should be more abundant in cold and dense regions. Our result also shows a similarity between N_2H^+ and CH_3OH . They also showed a contrast between CCH, CN, and other species. CCH and CN are known as PDR tracers, and their PC3 should have contributions from the UV radiation field. In fact, they suggested a tight positive correlation between PC1 and N_{H_2} , a positive but weak correlation between PC2 and n_{H} , and a moderate positive correlation between PC3 and the UV radiation field.

The above studies show that PCA is a useful way to identify coupled chemistries, reveal the underlying dynamics driving them, and summarize rich molecular line data sets. Extragalactic PCA studies seem to be consistent in showing distinct contributions in low-excitation transitions of methanol and HNCO, especially near the intersection of the bar orbit and the

central region. Galactic and extragalactic PCAs may show different categorizations of transitions, likely due to the difference in spatial scale.

6. Summary

We have presented integrated-intensity images of the isolated line emission from the ALCHEMI survey, a wide-frequency imaging spectral scan of the CMZ of the starburst galaxy NGC 253. With these images, we have performed a PCA as a statistical approach to reduce the dimensions of the data set to investigate underlying physical conditions that cause differences in line intensities, and to relate these physical conditions to starburst activities.

We succeeded in reducing the dimension of the data space from 150 variables to 5 principal components through PCA while retaining more than 96% of the original information. It reflects the fact that spatial distributions of various sub/millimeter emissions are highly correlated in the CMZ. One needs only a handful of uncorrelated parameters to explain the most of the standardized emission maps. Our PCA found that the nine GMCs in the CMZ are distinct from each other in their qualities after subtracting the effect of their overall emission strengths. We interpreted the PCs in physical terms and assessed various emissions with their contributions to the PCs. We list our findings below.

1. As expected, the largest factor that changes line intensities is the amount of molecular gas. There is an overall correlation among all the molecular emission lines, RRLs, and continuum images. This is indicated by the first principal component (PC1). Locations with larger molecular gas column densities in general emit stronger molecular transitions. These locations are also likely to have higher star formation rates (Kennicut–Schmidt law), which causes the higher intensity of RRLs. We also note that there are some biases that cause PC1 to deviate from an accurate measure of the total column density as discussed in the text. The deviation from this correlation appears in PC2 or higher.
2. High-excitation dense gas tracers and RRLs have similar spatial distributions and large positive contributions to PC2. Meanwhile, low-excitation ($J = 1-0$) dense gas tracers have negative coefficients for PC2; indeed, we found strong correlations between contributions to PC2 and critical densities as well as upper-state energies of the transitions of dense gas tracers. The difference between low-excitation dense gas and star formation tracers suggests that these low-excitation dense gas tracers also emit from less dense regions than indicated by their critical densities. This result is consistent with Galactic large-scale cloud observations in the literature.
3. Evolutionary stages of GMCs cause differences in the chemistry. Young starbursts (GMCs 3 and 6) tend to have peaks of high-excitation transitions of HC₃N and complex organic molecules (COMs), while more developed starbursts (GMCs 4, 5) have peaks of RRLs and high-excitation transitions of radicals (CN, CCH). This difference appears as positive and negative contributions to PC3, respectively. The lack of HC₃N and COMs in developed starbursts may be caused by photodissociation, which shows the effect of stellar feedback. These PDRs near the starbursts can be traced by high-excitation transitions of CN and CCH. These transitions should be

observable for some sources at $z = 2-3$ in the 3 mm band, and can be useful for studying the ISM variation during $z = 0-2$.

4. Comparisons between PC2 and PC4 show that low-excitation shock tracers (CH₃OH, HNCO, HOCO⁺, and OCS) do not correlate with star formation, and likely trace shocks caused by cloud collisions of x_1 and x_2 orbits. On the other hand, the high-excitation transitions of SiO may originate from star formation as their emissions are from locations of cluster-scale outflows in the literature.
5. Vertically extended structures, some of which must originate from outflows, have emissions of CO isotopologues, CCH, HOC⁺, H₃O⁺, HCN, HCO⁺, CS, and CN. The enhanced emission of HOC⁺, H₃O⁺ in outflows indicates that these outflows are highly ionized, possibly due to cosmic rays.
6. We have also made the first extragalactic detection of HCNH⁺, and the first extragalactic images for C₃H⁺ NO, and HCS⁺. From the characteristics of these species and their distributions, we suggest that C₃H⁺ emission preferentially comes from PDRs near the starburst while HCNH⁺ emits in cold clouds.

We have identified some categories of molecular transitions that are characteristics of physical conditions through the extensive spectral scan ALCHEMI. While not many observations can afford a wide-band scan like ALCHEMI, the overall chemical structures can be found by observing sets of transitions such as CO isotopologues, shock tracers (SiO, CH₃OH, HNCO), high-excitation dense gas tracers (HC₃N), or COMs, high-excitation radicals (CN, CCH) as starburst tracers. Reactive ions such as HOC⁺ and H₃O⁺ are also useful in tracing highly ionized regions as our previous studies found.

Acknowledgments

We appreciate the constructive comments by the anonymous referee. We thank Francesco Costagliola for setting the path to the ALCHEMI survey. We are also grateful to the ALMA staff at JAO and ARCs for their dedicated work to keep ALMA running, which made this survey possible. This paper makes use of the following ALMA data: ADS/JAO.ALMA#2017.1.00161.L, ADS/JAO.ALMA#2018.1.00162.S. ALMA is a partnership of ESO (representing its member states), NSF (USA) and NINS (Japan), together with NRC (Canada), MOST and ASIAA (Taiwan), and KASI (Republic of Korea), in cooperation with the Republic of Chile. The National Radio Astronomy Observatory is a facility of the National Science Foundation operated under cooperative agreement by Associated Universities, Inc. The Joint ALMA Observatory is operated by ESO, AUI/NRAO and NAOJ. Data analysis was in part carried out on the Multi-wavelength Data Analysis System operated by the Astronomy Data Center (ADC), National Astronomical Observatory of Japan. N.H. acknowledges support from JSPS KAKENHI grant No. JP21K03634, and the ALMA Japan Research Grant of NAOJ ALMA Project, NAOJ-ALMA-304. K.S. acknowledges the support from the Ministry of Science and Technology (MOST) of Taiwan through the grant MOST 111-2112-M-001-039. This work was supported by NAOJ ALMA Scientific Research grant No. 2021-18A. L.C. acknowledges financial support through the Spanish grant PID2019-105552RB-C41 funded by MCIN/AEI/10.13039/

501100011033. S.K. gratefully acknowledges funding from the European Research Council (ERC) under the European Union's Horizon 2020 research and innovation programme (grant agreement No. 789410). S.V., M.B., and K.-Y.H. acknowledge support from the ERC Advanced Grant MOPPEX 833460. K.K. acknowledges the support by JSPS KAKENHI grant No. JP17H06130 and the NAOJ ALMA Scientific Research grant No. 2017-06B. K.N. acknowledges the support by JSPS KAKENHI grant No. JP19K03937.

Facility: ALMA

Software: astropy (Astropy Collaboration et al. 2013, 2018), scikit-learn (Pedregosa et al. 2011), CASA (McMullin et al. 2007).

Appendix A Transitions Properties of Blended with the Same Species

The transitions of species such as CN, CCH are blended in our observations due to large line widths. We combined these blended neighboring transitions to make velocity-integrated images of these species. Table 2 lists these transitions.

Table 2
Spectroscopic Properties for Transitions Blended with the Same Species

Species	Transition	$\nu_{\text{rest}}^{\text{a}}$ (GHz)	E_{up}^{b} (K)	$\log(A_{\text{ul}})^{\text{c}}$ (s ⁻¹)
CN	$N = 1-0, J = 1/2-1/2, F = 1/2-3/2$	113.144	5.43	-4.98
	$N = 1-0, J = 1/2-1/2, F = 3/2-1/2$	113.170	5.43	-5.29
	$N = 1-0, J = 1/2-1/2, F = 3/2-3/2$	113.191	5.43	-5.18
CN	$N = 1-0, J = 3/2-1/2, F = 3/2-1/2$	113.488	5.45	-5.17
	$N = 1-0, J = 3/2-1/2, F = 5/2-3/2$	113.491	5.45	-4.92
	$N = 1-0, J = 3/2-1/2, F = 1/2-1/2$	113.500	5.45	-4.97
	$N = 1-0, J = 3/2-1/2, F = 3/2-3/2$	113.509	5.45	-5.28
CN	$N = 2-1, J = 3/2-3/2, F = 1/2-1/2$	226.287	16.3	-4.99
	$N = 2-1, J = 3/2-3/2, F = 1/2-3/2$	226.299	16.3	-5.08
	$N = 2-1, J = 3/2-3/2, F = 3/2-1/2$	226.303	16.3	-5.38
	$N = 2-1, J = 3/2-3/2, F = 3/2-3/2$	226.315	16.3	-5.00
	$N = 2-1, J = 3/2-3/2, F = 3/2-5/2$	226.332	16.3	-5.34
	$N = 2-1, J = 3/2-3/2, F = 5/2-3/2$	226.342	16.3	-5.50
	$N = 2-1, J = 3/2-3/2, F = 5/2-5/2$	226.360	16.3	-4.79
	$N = 2-1, J = 3/2-1/2, F = 1/2-3/2$	226.617	16.3	-4.97
	$N = 2-1, J = 3/2-1/2, F = 3/2-3/2$	226.632	16.3	-4.37
	$N = 2-1, J = 3/2-1/2, F = 5/2-3/2$	226.660	16.3	-4.02
	$N = 2-1, J = 3/2-1/2, F = 1/2-1/2$	226.664	16.3	-4.07
	$N = 2-1, J = 3/2-1/2, F = 3/2-1/2$	226.679	16.3	-4.28
	$N = 2-1, J = 5/2-3/2, F = 5/2-3/2$	226.874	16.3	-4.02
	$N = 2-1, J = 5/2-3/2, F = 7/2-5/2$	226.875	16.3	-3.94
	$N = 2-1, J = 5/2-3/2, F = 3/2-1/2$	226.876	16.3	-4.07
	$N = 2-1, J = 5/2-3/2, F = 3/2-3/2$	226.887	16.3	-4.56
	$N = 2-1, J = 5/2-3/2, F = 5/2-5/2$	226.892	16.3	-4.74
	$N = 2-1, J = 5/2-3/2, F = 3/2-5/2$	226.905	16.3	-5.95
CN	$N = 3-2, J = 5/2-5/2, F = 3/2-3/2$	339.447	32.6	-4.64
	$N = 3-2, J = 5/2-5/2, F = 3/2-5/2$	339.460	32.6	-5.36
	$N = 3-2, J = 5/2-5/2, F = 5/2-3/2$	339.463	32.6	-5.53
	$N = 3-2, J = 5/2-5/2, F = 5/2-5/2$	339.476	32.6	-4.67
	$N = 3-2, J = 5/2-5/2, F = 5/2-7/2$	339.493	32.6	-5.52
	$N = 3-2, J = 5/2-5/2, F = 7/2-5/2$	339.499	32.6	-5.63
	$N = 3-2, J = 5/2-5/2, F = 7/2-7/2$	339.517	32.6	-4.60
	$N = 3-2, J = 5/2-3/2, F = 3/2-5/2$	339.992	32.6	-5.41
	$N = 3-2, J = 5/2-3/2, F = 5/2-5/2$	340.008	32.6	-4.21
	$N = 3-2, J = 5/2-3/2, F = 3/2-3/2$	340.020	32.6	-4.03
	$N = 3-2, J = 5/2-3/2, F = 7/2-5/2$	340.032	32.6	-3.41
	$N = 3-2, J = 5/2-3/2, F = 3/2-1/2$	340.035	32.6	-3.54
	$N = 3-2, J = 5/2-3/2, F = 3/2-1/2$	340.035	32.6	-3.49
	$N = 3-2, J = 7/2-5/2, F = 7/2-5/2$	340.248	32.7	-3.42
	$N = 3-2, J = 7/2-5/2, F = 7/2-5/2$	340.248	32.7	-3.38
	$N = 3-2, J = 7/2-5/2, F = 5/2-3/2$	340.249	32.7	-3.43
	$N = 3-2, J = 7/2-5/2, F = 5/2-5/2$	340.262	32.7	-4.35
	$N = 3-2, J = 7/2-5/2, F = 7/2-7/2$	340.265	32.7	-4.47
CH ₃ CCH	$J = 5-4, K = 4$	85.431	128.0	-6.65
	$J = 5-4, K = 3$	85.443	77.3	-6.40
	$J = 5-4, K = 2$	85.451	41.2	-6.28

Table 2
(Continued)

Species	Transition	$\nu_{\text{rest}}^{\text{a}}$ (GHz)	E_{up}^{b} (K)	$\log(A_{\text{ul}})^{\text{c}}$ (s ⁻¹)
CH_3CCH	$J = 5-4, K = 1$	85.456	19.5	-6.23
	$J = 5-4, K = 0$	85.457	12.3	-6.21
CH_3CCH	$J = 6-5, K = 5$	102.499	198.0	-6.48
	$J = 6-5, K = 4$	102.517	133.0	-6.22
	$J = 6-5, K = 3$	102.530	82.3	-6.09
	$J = 6-5, K = 2$	102.540	46.1	-6.02
	$J = 6-5, K = 1$	102.546	24.5	-5.98
	$J = 6-5, K = 0$	102.548	17.2	-5.96
CH_3CCH	$J = 10-9, K = 5$	170.824	226.0	-5.41
	$J = 10-9, K = 4$	170.854	161.0	-5.36
	$J = 10-9, K = 3$	170.876	110.0	-5.33
	$J = 10-9, K = 2$	170.893	74.0	-5.30
	$J = 10-9, K = 1$	170.903	52.3	-5.29
	$J = 10-9, K = 0$	170.906	45.1	-5.29
CH_3CCH	$J = 11-10, K = 5$	187.904	235.0	-5.26
	$J = 11-10, K = 4$	187.936	170.0	-5.22
	$J = 11-10, K = 3$	187.961	119.0	-5.19
	$J = 11-10, K = 2$	187.979	83.0	-5.17
	$J = 11-10, K = 1$	187.990	61.4	-5.16
	$J = 11-10, K = 0$	187.994	54.1	-5.16
CH_3OH	$2(1, 2)-1(1, 1) \text{ E}$	96.739	12.5	-5.59
	$2(0, 2)-1(0, 1) \text{ A}$	96.741	6.96	-5.47
	$2(-0, 2)-1(-0, 1) \text{ E}$	96.745	20.1	-5.47
	$2(-1, 1)-1(-1, 0) \text{ E}$	96.756	28.0	-5.58
CCH	$N = 1-0, J = 3/2-1/2, F = 1-1$	87.284	4.19	-6.59
	$N = 1-0, J = 3/2-1/2, F = 2-1$	87.317	4.19	-5.82
	$N = 1-0, J = 3/2-1/2, F = 1-0$	87.329	4.19	-5.90
	$N = 1-0, J = 1/2-1/2, F = 1-1$	87.402	4.20	-5.90
	$N = 1-0, J = 1/2-1/2, F = 0-1$	87.407	4.20	-5.81
	$N = 1-0, J = 1/2-1/2, F = 1-0$	87.446	4.20	-6.58
CCH	$N = 2-1, J = 5/2-3/2, F = 3-2$	174.663	12.6	-4.83
	$N = 2-1, J = 5/2-3/2, F = 2-1$	174.668	12.6	-4.87
	$N = 2-1, J = 3/2-1/2, F = 2-1$	174.722	12.6	-4.95
	$N = 2-1, J = 3/2-1/2, F = 1-0$	174.728	12.6	-5.09
	$N = 2-1, J = 3/2-1/2, F = 1-1$	174.733	12.6	-5.29
	$N = 2-1, J = 3/2-3/2, F = 2-2$	174.807	12.6	-5.57
CCH	$N = 3-2, J = 7/2-5/2, F = 4-3$	262.004	25.1	-4.28
	$N = 3-2, J = 7/2-5/2, F = 3-2$	262.006	25.1	-4.29
	$N = 3-2, J = 5/2-3/2, F = 3-2$	262.065	25.2	-4.31
	$N = 3-2, J = 5/2-3/2, F = 2-1$	262.067	25.2	-4.35
	$N = 3-2, J = 5/2-3/2, F = 2-2$	262.079	25.2	-5.22
	$N = 3-2, J = 5/2-5/2, F = 3-3$	262.209	25.2	-5.40
CCH	$N = 4-3, J = 9/2-7/2, F = 5-4$	349.338	41.9	-3.88
	$N = 4-3, J = 9/2-7/2, F = 4-3$	349.339	41.9	-3.89
	$N = 4-3, J = 7/2-5/2, F = 4-3$	349.399	41.9	-3.90
	$N = 4-3, J = 7/2-5/2, F = 3-2$	349.401	41.9	-3.92
C_4H	$N = 12-11, J = 25/2-23/2, F = 12-11$	114.183	35.6	-4.44
	$N = 12-11, J = 25/2-23/2, F = 13-12$	114.183	35.6	-4.44
	$N = 12-11, J = 23/2-21/2, F = 11-10$	114.221	35.6	-4.44
	$N = 12-11, J = 23/2-21/2, F = 12-11$	114.221	35.6	-4.44

Notes.^a Rest frequency.^b Upper level energy of the transition.^c Einstein A coefficient; all values were taken from the Cologne Database for Molecular Spectroscopy (CDMS; <https://cdms.astro.uni-koeln.de>; Müller et al. 2001, 2005).

Appendix B

Transition Properties

Table 3 shows the spectroscopic properties of transitions used in our PCA in an ascending order in frequency.

Table 3
A List of Molecular Transitions and RRLs used in PCA

Transition	$\nu_{\text{rest}}^{\text{a}}$ (GHz)	E_{up}^{b} (K)	Transition	$\nu_{\text{rest}}^{\text{a}}$ (GHz)	E_{up}^{b} (K)
CH ₃ CCH(5 _K –4 _K)	85.457	12.3	HOCO ⁺ (4 _{0,4} –3 _{0,3})	85.531	10.26
CCS(7 ₆ –6 ₅) ^c	86.181	23.35	H ¹³ CN(1–0) ^c	86.34	4.14
H ¹³ CO ⁺ (1–0)	86.754	4.16	SiO(2–1)	86.847	6.25
HN ¹³ C(1–0)	87.091	4.18	CCH(1–0)	87.317	4.19
HNCO(4 _{1,4} –3 _{1,3})	87.597	53.78	HNCO(4 _{0,4} –3 _{0,3})	87.925	10.55
H52 β	88.406		HCN(1–0)	88.632	4.25
HCO ⁺ (1–0)	89.189	4.28	HOC ⁺ (1–0)	89.487	4.29
C ₃ H ⁺ (4–3)	89.958	10.79	HC ₃ N(34–33)	90.526	76.03
HNC(1–0)	90.664	4.35	HC ₃ N(10–9)	90.979	24.01
¹³ CS(2–1)	92.494	6.65	N ₂ H ⁺ (1–0)	93.173	4.47
H58 γ	93.776		CCS(7 ₈ –6 ₇) ^c	93.87	19.89
C ³⁴ S(2–1)	96.413	6.25	CH ₃ OH(2 _K –1 _K)	96.741	6.96
C ³³ S(2–1)	97.172	7.0	OCS(8–7) ^c	97.301	21.01
CH ₃ OH(2 _{1,1} –1 _{1,0})	97.583	21.56	³⁴ SO(2 ₃ –1 ₂) ^c	97.715	9.09
CS(2–1) ^c	97.981	7.1	HC ₃ N(37–36)	98.513	89.83
H40 α	99.023		HC ₃ N(11–10)	100.076	28.82
HC ₃ N, $v_7 = 1(11_1–10_{-1})$	100.322	349.73	CH ₃ CCH(6 _K –5 _K)	102.548	17.23
H ₂ CS(3 _{0,3} –2 _{0,2}) ^c	103.04	9.89	H49 β	105.302	
CCS(8 ₉ –7 ₈) ^c	106.348	70.39	H39 α	106.737	
HOCO ⁺ (5 _{0,5} –4 _{0,4})	106.914	15.39	CH ₃ OH(3 _{1,3} –4 _{0,4})	107.014	28.35
HC ₃ N(12–11)	109.174	34.06	C ¹⁸ O(1–0) ^c	109.782	5.27
HNCO(5 _{0,5} –4 _{0,4})	109.906	15.82	¹³ CO(1–0) ^c	110.201	5.29
C ¹⁷ O(1–0) ^c	112.359	5.39	CN(1 _{3/2} –0 _{3/2})	113.191	5.43
CN(1 _{5/2} –0 _{3/2})	113.491	5.45	C ₄ H(12–11)	114.221	35.64
CO(1–0)	115.271	5.53	HC ₃ N(14–13)	127.368	45.85
HOCO ⁺ (6 _{0,6} –5 _{0,5})	128.295	21.55	SiO(3–2)	130.269	12.5
HNCO(6 _{1,6} –5 _{1,5})	131.394	65.35	HNCO(6 _{0,6} –5 _{0,5})	131.886	22.15
HC ₃ N(15–14)	136.464	52.4	SO(3 ₄ –2 ₃)	138.179	15.86
¹³ CS(3–2)	138.739	13.32	CH ₃ OH(3 _{1,3} –2 _{1,2})	143.866	28.35
CCS(11 ₂ –10 ₁₁) ^c	144.245	43.94	C ³⁴ S(3–2)	144.617	11.8
C ³³ S(3–2)	145.756	13.99	HCNH ⁺ (2–1)	148.221	10.67
HOCO ⁺ (7 _{0,7} –6 _{0,6})	149.676	28.73	HNCO(7 _{1,6} –6 _{1,5})	154.415	72.92
HC ₃ N(17–16)	154.657	66.8	CH ₃ OH(2 _{1,2} –3 _{0,3})	156.602	21.44
C ₃ H ⁺ (7–6)	157.419	30.22	HC ₃ N(18–17)	163.753	74.66
H ³⁴ S(1 _{1,0} –1 _{1,0,1}) ^c	167.911	27.83	H ₂ S(1 _{1,0} –1 _{0,1}) ^c	168.763	27.88
H ₂ CS(5 _{1,5} –4 _{1,4}) ^c	169.114	37.52	CH ₃ OH(3 _{2,2} –2 _{1,1})	170.061	36.17
HCS ⁺ (4–3)	170.692	20.48	CH ₃ CCH(10 _K –9 _K)	170.906	45.11
H ¹³ CN(2–1) ^c	172.678	12.43	HC ₃ N(19–18)	172.849	82.96
H ¹³ CO ⁺ (2–1) ^c	173.507	12.49	HN ¹³ C(2–1)	174.179	12.54
CCH(2–1)	174.663	12.57	HNCO(8 _{0,8} –7 _{0,7})	175.844	37.98
HCN(2–1)	177.261	12.76	HCO ⁺ (2–1)	178.375	12.84
SO(4 ₅ –3 ₄) ^c	178.605	24.43	HOC ⁺ (2–1)	178.972	12.88
HNC(2–1)	181.325	13.05	CH ₃ CCH(11 _K –10 _K)	187.994	54.13
C ³⁴ S(4–3)	192.818	18.98	CH ₃ OH(4 _{1,3} –3 _{1,2})	195.147	37.95
CS(4–3) ^c	195.954	23.5	HNCO(9 _{0,9} –8 _{0,8})	197.821	47.47
CH ₂ NH(3 _{1,2} –2 _{1,1})	199.823	27.07	HC ₃ N(22–21)	200.135	110.46
CH ₃ CCH(12 _K –11 _K)	205.081	63.98	c-C ₃ H ₂ (3 _{3,0} –2 _{2,1})	216.279	13.53
H ₂ S(2 _{2,0} –2 _{1,1}) ^c	216.71	83.98	SiO(5–4)	217.105	31.26
C ¹⁸ O(2–1)	219.56	15.81	¹³ CO(2–1)	220.399	15.87
C ¹⁷ O(2–1) ^c	224.714	16.18	CN(2–1)	226.66	16.31
HC ₃ N(25–24)	227.419	141.89	CO(2–1)	230.538	16.6
HC ₃ N(26–25)	236.513	153.25	C ³³ S(5–4)	242.914	34.97
CS(5–4)	244.936	35.3	NO(3 _{1,3} –2 _{–1,2})	250.437	19.23
NO(3 _{–1,3} –2 _{1,2})	250.796	19.28	³⁴ SO(6 ₇ –5 ₆) ^c	256.878	46.71
H ¹³ CN(3–2) ^c	259.012	24.86	H ¹³ CO ⁺ (3–2)	260.255	24.98
SiO(6–5)	260.518	43.76	CCH(3–2)	262.004	25.15
HCN(3–2)	265.886	25.52	CH ₂ NH(4 _{1,3} –3 _{1,2})	266.27	39.84

Table 3
(Continued)

Transition	$\nu_{\text{rest}}^{\text{a}}$ (GHz)	E_{up}^{b} (K)	Transition	$\nu_{\text{rest}}^{\text{a}}$ (GHz)	E_{up}^{b} (K)
CH ₃ OH(5 _{2,4} –4 _{1,3})	266.838	57.07	HCO ⁺ (3–2)	267.558	25.68
HOC ⁺ (3–2)	268.451	25.77	HNC(3–2)	271.981	26.11
HC ₃ N(30–29)	272.885	203.01	¹³ CS(6–5)	277.455	46.61
H ₂ CS(8 _{1,7} –7 _{1,6}) ^c	278.888	73.41	N ₂ H ⁺ (3–2)	279.512	26.83
CH ₃ OH(6 _{1,6} –5 _{1,5})	287.671	62.87	C ³⁴ S(6–5)	289.209	38.19
CS(6–5)	293.912	49.4	H ₂ S(3 _{3,0} –3 _{2,1}) ^c	300.506	168.9
CH ₃ OH(1 _{1,0} –1 _{0,1})	303.367	16.88	CH ₃ OH(3 _{1,2} –3 _{0,3})	305.473	28.59
CH ₃ OH(6 _{1,5} –6 _{0,6})	311.853	63.71	CH ₃ OH(7 _{1,6} –7 _{0,7})	314.86	80.09
CH ₃ OH(6 _{2,5} –5 _{1,4})	315.267	71.0	H27 α	316.415	
C ¹⁸ O(3–2)	329.331	31.61	¹³ CO(3–2)	330.588	31.73
HC ₃ N(37–36)	336.52	306.91	C ¹⁷ O(3–2) ^c	337.061	32.35
CN(3–2)	340.032	32.66	CS(7–6)	342.883	65.8
CO(3–2)	345.796	33.19	H ¹³ CO ⁺ (4–3)	346.998	41.63
SiO(8–7)	347.331	75.02	CCH(4–3)	349.338	41.91
HNCO(16 _{1,16} –15 _{1,15})	350.333	186.2	HCN(4–3)	354.505	42.53
HCO ⁺ (4–3)	356.734	42.8	HNC(4–3)	362.63	43.51
H ₃ O ⁺ (3 _{2,0} –2 _{2,1})	364.797	97.06	N ₂ H ⁺ (4–3)	372.672	44.71

Notes.^a Rest frequency.^b Upper level energy of the transition; all values were taken from the CDMS (<https://cdms.astro.uni-koeln.de>; Müller et al. 2001, 2005).^c Maps that are used in PCA, but not shown in this paper because they are included in the future publications.

Appendix C PC Coefficients

The coefficients of all the 150 emissions for PC1 through PC10 are in Table 4.

Table 4
PC Coefficients for Each Species

Transition	PC1	PC2	PC3	PC4	PC5	PC6	PC7	PC8	PC9	PC10
CO(1–0)	0.069	-0.127	-0.129	-0.046	0.163	0.029	0.161	-0.001	-0.116	-0.065
CO(2–1)	0.071	-0.115	-0.138	-0.055	0.140	-0.017	0.170	-0.024	-0.132	-0.058
CO(3–2)	0.075	-0.097	-0.139	-0.057	0.101	-0.060	0.125	-0.011	-0.087	-0.035
¹³ CO(1–0)	0.071	-0.131	-0.102	-0.030	0.151	0.133	0.081	0.064	-0.001	-0.110
¹³ CO(2–1)	0.082	-0.080	-0.102	-0.068	0.079	0.053	0.034	0.038	0.015	-0.059
¹³ CO(3–2)	0.087	-0.031	-0.093	-0.071	0.019	0.015	-0.024	0.046	0.034	-0.022
C ¹⁸ O(1–0)	0.076	-0.123	-0.078	-0.028	0.120	0.145	0.055	0.065	0.052	-0.079
C ¹⁸ O(2–1)	0.086	-0.064	-0.071	-0.075	0.054	0.058	0.014	0.043	0.066	-0.015
C ¹⁸ O(3–2)	0.090	-0.005	-0.057	-0.067	-0.005	0.031	-0.044	0.047	0.056	-0.013
C ¹⁷ O(1–0)	0.075	-0.120	-0.073	-0.012	0.099	0.188	-0.008	0.090	0.102	-0.074
C ¹⁷ O(2–1)	0.087	-0.057	-0.060	-0.068	0.036	0.067	-0.027	0.056	0.072	-0.057
C ¹⁷ O(3–2)	0.090	0.017	-0.030	-0.058	-0.009	0.019	-0.073	0.051	0.082	-0.017
HCN(1–0)	0.080	-0.101	-0.093	-0.073	0.068	-0.063	0.089	-0.109	-0.093	-0.001
HCN(2–1)	0.082	-0.073	-0.111	-0.045	0.063	-0.085	0.125	-0.053	-0.094	0.037
HCN(3–2)	0.088	-0.019	-0.078	0.000	-0.035	-0.112	0.016	-0.032	-0.033	0.046
HCN(4–3)	0.089	0.012	-0.060	0.025	-0.054	-0.098	-0.021	-0.023	-0.011	0.037
HCO ⁺ (1–0)	0.079	-0.094	-0.090	-0.117	0.066	-0.033	0.106	-0.128	-0.077	-0.035
HCO ⁺ (2–1)	0.082	-0.063	-0.113	-0.091	0.066	-0.056	0.138	-0.063	-0.062	0.011
HCO ⁺ (3–2)	0.088	-0.005	-0.087	-0.042	-0.029	-0.063	0.011	-0.029	-0.001	0.025
HCO ⁺ (4–3)	0.089	0.027	-0.072	-0.007	-0.043	-0.015	-0.041	-0.015	0.031	0.029
CN(1 _{3/2} –0 _{3/2})	0.083	-0.053	-0.101	-0.128	0.061	-0.047	-0.008	-0.073	-0.025	0.038
CN(1 _{5/2} –0 _{3/2})	0.082	-0.050	-0.116	-0.120	0.045	-0.067	0.058	-0.099	-0.057	0.023
CN(2–1)	0.085	0.016	-0.123	-0.047	-0.025	-0.070	-0.019	-0.015	-0.009	0.039
CN(3–2)	0.083	0.065	-0.120	0.016	-0.052	-0.052	-0.053	0.023	-0.003	0.019
HNC(1–0)	0.086	-0.043	-0.098	-0.063	0.041	-0.008	-0.014	-0.067	-0.015	0.040
HNC(2–1)	0.087	0.032	-0.083	0.004	-0.069	-0.040	-0.075	-0.068	0.073	0.053
HNC(3–2)	0.087	0.045	-0.085	0.027	-0.022	-0.034	-0.062	-0.069	0.009	0.027
HNC(4–3)	0.086	0.072	-0.065	0.048	-0.007	-0.023	-0.089	-0.094	0.007	0.015
N ₂ H ⁺ (1–0)	0.085	-0.091	-0.040	0.053	0.026	-0.017	-0.015	-0.136	-0.033	-0.032
N ₂ H ⁺ (3–2)	0.088	0.015	-0.055	0.101	-0.031	-0.043	-0.029	-0.162	0.017	-0.051
N ₂ H ⁺ (4–3)	0.086	0.058	-0.045	0.105	-0.030	-0.083	-0.053	-0.150	0.003	-0.060

Table 4
(Continued)

Transition	PC1	PC2	PC3	PC4	PC5	PC6	PC7	PC8	PC9	PC10
CS(2–1)	0.084	−0.092	−0.062	−0.062	0.067	−0.045	0.046	−0.013	0.016	0.003
CS(4–3)	0.090	−0.023	−0.047	−0.043	0.002	−0.082	0.001	0.019	0.018	0.017
CS(5–4)	0.091	0.014	−0.034	−0.029	−0.012	−0.075	−0.011	0.032	0.024	0.016
CS(6–5)	0.090	0.040	−0.023	−0.004	−0.009	−0.070	−0.013	0.065	0.015	0.005
CS(7–6)	0.088	0.064	−0.019	0.028	0.008	−0.068	−0.027	0.092	−0.008	0.014
CCH(1–0)	0.085	−0.059	−0.087	−0.097	0.048	0.009	−0.007	−0.006	0.005	0.017
CCH(2–1)	0.086	0.051	−0.057	−0.032	−0.101	0.003	−0.118	0.002	0.022	−0.009
CCH(3–2)	0.088	0.051	−0.072	−0.018	−0.029	−0.004	−0.067	0.036	−0.015	0.005
CCH(4–3)	0.084	0.080	−0.088	0.021	−0.039	0.006	−0.056	0.015	−0.006	0.007
H ¹³ CN(1–0)	0.085	−0.089	−0.001	−0.054	0.051	−0.070	−0.108	−0.125	−0.049	0.006
H ¹³ CN(2–1)	0.091	−0.007	−0.023	−0.019	0.020	−0.079	−0.069	−0.047	−0.045	0.021
H ¹³ CN(3–2)	0.089	0.058	0.014	0.040	0.040	−0.085	−0.071	−0.025	0.004	0.008
H ¹³ CO ⁺ (1–0)	0.086	−0.065	−0.010	−0.126	0.050	0.020	−0.118	−0.085	−0.006	−0.009
H ¹³ CO ⁺ (2–1)	0.081	0.048	0.089	−0.040	0.046	0.144	0.027	0.078	0.066	−0.173
H ¹³ CO ⁺ (3–2)	0.087	0.077	−0.025	−0.011	−0.011	0.045	−0.070	−0.028	−0.022	−0.011
H ¹³ CO ⁺ (4–3)	0.085	0.093	0.009	0.014	0.032	0.067	−0.071	−0.063	−0.021	−0.013
HN ¹³ C(1–0)	0.089	−0.036	−0.003	−0.049	0.022	0.009	−0.171	−0.100	0.042	0.005
HN ¹³ C(2–1)	0.083	0.088	0.006	0.010	0.001	0.124	−0.089	−0.170	−0.010	−0.004
¹³ CS(2–1)	0.086	−0.033	0.069	−0.066	−0.003	−0.111	−0.048	0.036	0.152	−0.016
¹³ CS(3–2)	0.087	0.031	0.073	−0.065	0.025	−0.070	−0.026	0.020	0.153	−0.017
¹³ CS(6–5)	0.070	0.117	0.078	0.126	0.243	−0.063	0.059	0.039	0.131	0.093
C ³⁴ S(2–1)	0.087	−0.069	−0.009	−0.060	0.059	−0.041	0.018	0.009	0.061	0.013
C ³⁴ S(3–2)	0.090	−0.012	−0.014	−0.036	0.048	−0.057	0.011	0.043	0.096	0.033
C ³⁴ S(4–3)	0.089	0.043	0.027	−0.014	0.047	−0.084	−0.025	0.039	0.087	0.019
C ³⁴ S(6–5)	0.084	0.092	0.019	0.039	0.102	−0.075	−0.044	0.085	0.073	0.027
C ³³ S(2–1)	0.087	−0.015	0.059	−0.093	−0.020	−0.086	−0.046	0.024	0.171	−0.053
C ³³ S(3–2)	0.086	0.057	0.078	−0.021	0.061	−0.045	−0.015	−0.011	0.079	0.003
C ³³ S(5–4)	0.081	0.084	0.085	0.038	0.105	0.021	−0.024	−0.002	−0.036	0.013
HOC ⁺ (1–0)	0.069	−0.120	−0.075	−0.151	0.138	0.070	0.174	0.184	0.206	0.197
HOC ⁺ (2–1)	0.081	0.048	0.015	−0.120	−0.065	0.205	−0.103	0.293	−0.075	0.023
HOC ⁺ (3–2)	0.084	0.073	−0.068	−0.069	−0.015	0.049	−0.182	0.008	−0.109	0.065
SiO(2–1)	0.081	−0.112	0.034	0.012	0.025	−0.058	−0.117	−0.118	−0.102	0.060
SiO(3–2)	0.087	−0.070	0.033	0.039	−0.004	−0.057	−0.063	−0.071	−0.087	0.060
SiO(5–4)	0.090	0.013	0.044	0.039	−0.026	−0.095	−0.061	0.046	−0.072	0.024
SiO(6–5)	0.088	0.055	0.046	0.050	0.010	−0.080	−0.036	0.079	−0.084	0.020
SiO(8–7)	0.072	0.073	0.166	0.034	0.186	−0.072	0.034	0.083	0.007	0.018
CH ₃ OH(2 _K –1 _K)	0.048	−0.211	−0.010	0.191	0.053	0.032	0.040	0.023	−0.054	0.013
CH ₃ OH(2 _{1,1} –1 _{1,0})	0.060	−0.163	0.090	0.178	−0.120	−0.103	0.049	−0.066	0.058	0.057
CH ₃ OH(3 _{1,3} –4 _{0,4})	0.078	0.030	0.155	−0.106	−0.023	0.166	0.051	−0.004	−0.139	−0.019
CH ₃ OH(3 _{1,3} –2 _{1,2})	0.065	−0.151	0.093	0.140	−0.125	−0.137	0.075	−0.077	0.026	0.074
CH ₃ OH(2 _{1,2} –3 _{0,3})	0.084	0.010	0.082	−0.065	−0.073	0.084	0.115	0.119	0.114	0.133
CH ₃ OH(3 _{2,2} –2 _{1,1})	0.076	−0.135	0.041	0.019	−0.033	0.002	0.050	0.059	0.135	0.077
CH ₃ OH(4 _{1,3} –3 _{1,2})	0.079	−0.076	0.110	0.023	−0.139	−0.139	0.115	−0.125	−0.042	0.014
CH ₃ OH(5 _{2,4} –4 _{1,3})	0.086	−0.029	0.087	−0.057	−0.094	−0.048	0.006	0.049	−0.048	−0.013
CH ₃ OH(6 _{1,6} –5 _{1,5})	0.077	−0.041	0.135	−0.028	−0.176	−0.106	0.220	−0.197	0.030	−0.001
CH ₃ OH(1 _{1,0} –1 _{0,1})	0.089	−0.033	0.040	−0.061	0.007	0.076	−0.033	0.042	−0.028	0.106
CH ₃ OH(3 _{1,2} –3 _{0,3})	0.089	−0.012	0.049	−0.057	−0.045	0.084	−0.049	−0.011	−0.045	0.067
CH ₃ OH(6 _{1,5} –6 _{0,6})	0.088	0.041	0.064	−0.011	−0.042	0.035	−0.017	−0.115	−0.079	0.006
CH ₃ OH(7 _{1,6} –7 _{0,7})	0.088	0.041	0.056	0.001	−0.028	0.019	−0.027	−0.071	−0.145	0.025
CH ₃ OH(6 _{2,5} –5 _{1,4})	0.085	−0.009	0.102	−0.033	−0.082	0.031	0.002	−0.015	−0.214	0.078
HNCO(4 _{1,4} –3 _{1,3})	0.081	0.066	−0.032	0.020	−0.127	0.106	0.175	−0.112	0.031	−0.093
HNCO(4 _{0,4} –3 _{0,3})	0.043	−0.201	−0.009	0.260	0.069	0.130	−0.061	0.066	−0.121	0.062
HNCO(5 _{0,5} –4 _{0,4})	0.053	−0.197	−0.002	0.208	0.042	0.097	−0.023	0.052	−0.015	0.045
HNCO(6 _{1,6} –5 _{1,5})	0.077	−0.049	0.108	−0.004	−0.110	0.161	0.101	−0.151	0.004	−0.027
HNCO(6 _{0,6} –5 _{0,5})	0.062	−0.188	0.015	0.142	0.003	0.065	0.026	0.041	0.076	0.048
HNCO(7 _{1,6} –6 _{1,5})	0.078	0.056	0.124	−0.027	−0.009	0.181	0.213	0.047	−0.091	−0.018
HNCO(8 _{0,8} –7 _{0,7})	0.082	−0.087	0.058	−0.049	−0.136	−0.003	0.010	0.056	0.217	0.032
HNCO(9 _{0,9} –8 _{0,8})	0.082	−0.048	0.099	−0.105	−0.141	0.014	0.093	0.050	0.142	−0.019
HNCO(16 _{1,16} –15 _{1,15})	0.080	0.109	0.036	0.059	0.061	0.163	0.058	−0.166	−0.067	0.023
HOCO ⁺ (4 _{0,4} –3 _{0,3})	0.042	−0.196	0.038	0.276	0.010	0.123	−0.157	0.069	−0.117	0.050
HOCO ⁺ (5 _{0,5} –4 _{0,4})	0.050	−0.193	0.023	0.237	−0.018	0.076	−0.097	0.045	−0.023	−0.032
HOCO ⁺ (6 _{0,6} –5 _{0,5})	0.076	−0.116	0.027	0.124	−0.108	0.002	−0.026	−0.000	0.173	−0.036
HOCO ⁺ (7 _{0,7} –6 _{0,6})	0.074	−0.056	0.142	−0.107	−0.167	−0.008	0.111	−0.035	0.226	−0.155
H40 α	0.068	0.113	−0.171	0.115	−0.096	0.015	0.053	0.073	0.009	0.040
H39 α	0.070	0.107	−0.165	0.103	−0.099	0.011	0.060	0.062	0.020	0.034
H27 α	0.066	0.118	−0.161	0.147	−0.083	0.042	0.124	0.018	0.017	0.053
H52 β	0.064	0.119	−0.170	0.150	−0.108	0.002	0.097	0.065	−0.014	−0.017
H49 β	0.065	0.119	−0.171	0.141	−0.106	0.026	0.075	0.027	−0.011	0.029
H58 γ	0.057	0.116	−0.192	0.168	−0.139	0.039	0.166	0.031	0.025	0.002
CH ₃ CCH(5 _K –4 _K)	0.086	−0.072	0.001	−0.059	−0.005	0.172	−0.052	−0.018	0.072	0.021
CH ₃ CCH(6 _K –5 _K)	0.088	−0.050	−0.015	−0.061	−0.040	0.146	−0.035	0.001	0.096	0.044
CH ₃ CCH(10 _K –9 _K)	0.089	0.010	−0.009	−0.087	−0.050	0.097	−0.039	−0.040	−0.019	0.039

Table 4
(Continued)

Transition	PC1	PC2	PC3	PC4	PC5	PC6	PC7	PC8	PC9	PC10
CH ₃ CCH(11 _K -10 _K)	0.083	0.070	0.067	-0.034	-0.052	0.232	0.078	-0.035	-0.126	-0.035
CH ₃ CCH(12 _K -11 _K)	0.089	0.033	-0.001	-0.062	-0.061	0.097	-0.020	-0.027	-0.022	0.011
SO(3 _{_4} -2 ₃)	0.090	-0.036	0.008	0.030	0.012	-0.041	-0.057	0.039	-0.035	-0.012
SO(4 _{_5} -3 ₄)	0.080	-0.006	0.010	0.102	0.050	-0.134	0.002	0.140	-0.128	-0.748
³⁴ SO(2 _{_3} -1 ₂)	0.086	0.061	0.050	0.013	-0.075	0.049	0.114	-0.021	0.040	-0.106
³⁴ SO(6 _{_7} -5 ₆)	0.070	0.100	0.125	0.061	0.234	0.042	-0.031	-0.240	-0.008	0.017
H ₂ S(1 _{1,0} -1 _{0,1})	0.088	-0.010	-0.040	0.003	0.149	-0.090	-0.057	-0.030	0.013	-0.010
H ₂ S(2 _{2,0} -2 _{1,1})	0.082	0.103	0.048	0.053	0.113	0.034	-0.020	-0.063	0.029	0.042
H ₂ S(3 _{3,0} -3 _{2,1})	0.075	0.118	0.058	0.099	0.194	-0.022	-0.044	-0.047	0.066	0.065
OCS(8-7)	0.063	-0.162	0.071	0.187	-0.024	0.079	-0.046	0.003	0.097	0.012
H ₂ ³⁴ S(1 _{1,0} -1 _{0,1})	0.081	0.088	0.077	0.049	0.124	0.020	0.006	-0.099	0.146	-0.006
HC ₃ N(10-9)	0.087	-0.081	0.033	0.014	-0.040	-0.031	0.008	-0.009	-0.027	0.032
HC ₃ N(11-10)	0.088	-0.066	0.032	0.006	-0.032	-0.035	0.004	-0.014	-0.018	0.017
HC ₃ N(12-11)	0.089	-0.053	0.042	0.003	-0.042	-0.054	0.016	0.001	-0.031	0.015
HC ₃ N(14-13)	0.090	-0.022	0.046	-0.002	-0.040	-0.046	0.006	0.005	-0.049	0.017
HC ₃ N(15-14)	0.090	-0.018	0.043	-0.000	-0.037	-0.067	0.013	0.035	-0.090	0.002
HC ₃ N(17-16)	0.090	0.009	0.038	0.011	-0.033	-0.070	-0.003	0.083	-0.077	0.033
HC ₃ N(18-17)	0.090	0.001	0.033	-0.010	-0.009	-0.086	0.006	0.078	-0.057	0.025
HC ₃ N(19-18)	0.089	0.030	0.041	-0.012	-0.028	-0.094	-0.017	0.094	-0.089	0.004
HC ₃ N(22-21)	0.086	0.068	0.072	0.018	0.018	-0.056	0.031	0.127	-0.072	-0.004
HC ₃ N(25-24)	0.087	0.062	0.051	0.020	0.063	-0.087	0.021	0.100	0.005	0.042
HC ₃ N(26-25)	0.086	0.076	0.056	0.034	0.057	-0.078	0.014	0.104	-0.050	-0.003
HC ₃ N(30-29)	0.084	0.093	0.038	0.048	0.063	-0.027	0.015	0.110	0.006	0.003
HC ₃ N(37-36)	0.075	0.111	0.090	0.096	0.192	0.013	0.060	0.023	0.067	0.050
HC ₃ N, $v_7 = 1(11_1-10_{-1})$	0.068	0.094	0.149	0.068	0.246	0.019	0.052	-0.061	0.073	0.053
H ₃ O ⁺ (3 _{2,0} -2 _{1,1})	0.087	0.046	-0.077	-0.023	0.025	0.004	-0.091	0.065	-0.004	0.090
CCS(7 _{_6} -6 ₅)	0.086	0.020	-0.041	-0.048	-0.081	-0.113	-0.090	0.125	0.080	-0.025
CCS(7 ₈ -6 ₇)	0.089	0.001	0.032	0.004	-0.064	0.016	-0.084	0.016	0.031	-0.094
CCS(8 ₉ -7 ₈)	0.088	-0.000	0.045	-0.017	-0.036	-0.051	-0.041	-0.024	0.072	-0.075
CCS(11 ₁₂ -10 ₁₁)	0.081	0.101	0.054	0.062	0.069	0.046	0.059	0.048	-0.035	-0.076
H ₂ CS(3 _{0,3} -2 _{0,2})	0.081	-0.085	0.076	-0.001	-0.093	-0.076	-0.110	0.018	0.046	0.010
H ₂ CS(5 _{1,5} -4 _{1,4})	0.078	-0.018	0.130	0.033	0.013	-0.169	0.025	0.142	-0.028	-0.118
H ₂ CS(8 _{1,7} -7 _{1,6})	0.080	0.087	0.094	0.060	0.098	0.011	0.142	-0.011	-0.014	0.044
HC ₅ N(34-33)	0.070	-0.022	0.176	-0.066	-0.085	-0.106	0.151	0.260	-0.335	0.255
HC ₅ N(37-36)	0.082	0.032	0.140	-0.030	-0.047	0.019	0.166	-0.034	-0.014	-0.060
C ₃ H ⁺ (4-3)	0.084	0.070	-0.017	-0.064	-0.016	0.107	-0.212	0.034	-0.053	0.018
C ₃ H ⁺ (7-6)	0.065	0.132	-0.108	0.192	0.007	0.012	0.168	-0.082	0.126	0.034
CH ₂ NH(3 _{1,2} -2 _{1,1})	0.085	0.047	0.054	-0.064	-0.104	0.150	0.050	-0.152	-0.090	-0.029
CH ₂ NH(4 _{1,3} -3 _{1,2})	0.085	0.069	0.090	0.006	0.029	0.053	0.103	-0.007	-0.001	0.013
C ₄ H(12-11)	0.085	0.071	0.019	-0.045	-0.042	0.132	-0.040	0.106	-0.117	-0.055
HCNH ⁺ (2-1)	0.080	-0.054	0.088	0.047	-0.067	0.130	-0.104	-0.038	0.085	-0.043
HCS ⁺ (4-3)	0.086	0.033	0.063	-0.068	-0.050	-0.042	-0.059	-0.025	-0.046	-0.083
c-C ₃ H ₂ (3 _{0,0} -2 _{1,1})	0.088	0.057	-0.035	-0.039	-0.061	0.032	-0.096	-0.086	0.005	-0.016
NO(3 _{1,3} -2 _{1,2})	0.091	-0.011	-0.015	0.048	-0.030	0.008	-0.091	0.024	-0.053	-0.043
NO(3 _{-1,3} -2 _{1,2})	0.091	0.004	-0.012	0.043	-0.018	0.026	-0.102	0.048	-0.047	-0.037
3 mm continuum	0.068	0.101	-0.182	0.101	-0.096	-0.008	0.096	0.112	0.026	0.036
0.8 mm continuum	0.085	0.067	-0.078	0.042	-0.065	0.101	-0.039	-0.036	0.040	-0.024

Appendix D Estimation of Errors in PCA

To estimate errors, we tried the so-called bootstrapping method. We first created the rms error map, then multiplied it with a random number distribution that has the same size as the number of pixels, mean of 0, and standard distribution of 1. We added this noise map to the original image, and ran PCA. We examined how results changed for 1000 different sets of random number distributions for each transition tested. We only used the selected transitions for bootstrapping: HCN(1-0)

and ¹³CO(1-0) for high-intensity transitions; H39 α for intermediate; HC₃N $v_7 = 1$ (11₁-10₋₁), CH₂NH(4_{1,3}-3_{1,2}), and OCS(8-7) for low-intensity transitions. The results are shown in Table 5. For high-intensity transitions, the addition of noise did not change the results in any significant way, and the results are not shown. The variation among 1000 different noise maps added is overall small. However, we also note that, for a compact transition such as HC₃N $v_7 = 1$ (11₁-10₋₁), an act of adding noise itself changes the PCs more than the variation among different random noise sets. Nonetheless, qualitative results do not change even for these transitions.

Table 5
Bootstrapping Results

PC	Original	Mean (Bootstrap)	Standard Deviation (Bootstrap)
H39 α			
PC1	0.070	0.070	0.000
PC2	0.107	0.107	0.001
PC3	-0.165	-0.165	0.001
PC4	0.103	0.102	0.001
PC5	-0.099	-0.099	0.002
PC6	0.011	0.011	0.003
PC7	0.060	0.060	0.003
PC8	0.062	0.063	0.004
PC9	0.020	0.021	0.004
PC10	0.034	0.034	0.005
$\text{HC}_3\text{N } v7 = 1 (11_1-10_{-1})$			
PC1	0.068	0.066	0.000
PC2	0.094	0.092	0.002
PC3	0.149	0.146	0.003
PC4	0.068	0.067	0.005
PC5	0.246	0.247	0.005
PC6	0.019	0.019	0.008
PC7	0.052	0.057	0.012
PC8	-0.061	-0.070	0.016
PC9	0.073	0.082	0.014
PC10	0.053	0.072	0.029
$\text{CH}_2\text{NH}(4_{1,3}-3_{1,2})$			
PC1	0.085	0.084	0.000
PC2	0.069	0.068	0.001
PC3	0.090	0.089	0.002
PC4	0.006	0.006	0.003
PC5	0.029	0.030	0.003
PC6	0.053	0.054	0.005
PC7	0.103	0.105	0.006
PC8	-0.007	-0.007	0.008
PC9	-0.001	-0.002	0.007
PC10	0.013	0.013	0.010
OCS(8–7)			
PC1	0.063	0.063	0.000
PC2	-0.162	-0.162	0.000
PC3	0.071	0.071	0.001
PC4	0.187	0.187	0.001
PC5	-0.024	-0.023	0.001
PC6	0.079	0.079	0.002
PC7	-0.046	-0.045	0.003
PC8	0.003	0.002	0.004
PC9	0.097	0.099	0.003
PC10	0.012	0.011	0.005

Note. Transitions with strong emission such as $^{13}\text{CO}(1-0)$ and $\text{HCN}(1-0)$ did not show any significant difference between the original and bootstrapped cases, with very little standard deviation from the errors. Therefore, these transitions are not shown.

ORCID iDs

- Nanase Harada <https://orcid.org/0000-0002-6824-6627>
- David S. Meier <https://orcid.org/0000-0001-9436-9471>
- Sergio Martín <https://orcid.org/0000-0001-9281-2919>
- Sebastien Muller <https://orcid.org/0000-0002-9931-1313>
- Kazushi Sakamoto <https://orcid.org/0000-0001-5187-2288>
- Toshiki Saito <https://orcid.org/0000-0002-2501-9328>
- Mark D. Gorski <https://orcid.org/0000-0001-9300-354X>
- Christian Henkel <https://orcid.org/0000-0002-7495-4005>

- Kunihiko Tanaka <https://orcid.org/0000-0001-8153-1986>
- Jeffrey G. Mangum <https://orcid.org/0000-0003-1183-9293>
- Susanne Aalto <https://orcid.org/0000-0002-5828-7660>
- Rebeca Aladro <https://orcid.org/0000-0002-1316-1343>
- Mathilde Bouvier <https://orcid.org/0000-0003-0167-0746>
- Laura Colzi <https://orcid.org/0000-0001-8064-6394>
- Kimberly L. Emig <https://orcid.org/0000-0001-6527-6954>
- Rubén Herrero-Illana <https://orcid.org/0000-0002-7758-8717>
- Ko-Yun Huang <https://orcid.org/0000-0002-1227-8435>
- Kotaro Kohno <https://orcid.org/0000-0002-4052-2394>
- Sabine König <https://orcid.org/0000-0001-6174-8467>
- Kouichiro Nakanishi <https://orcid.org/0000-0002-6939-0372>
- Yuri Nishimura <https://orcid.org/0000-0003-0563-067X>
- Shuro Takano <https://orcid.org/0000-0001-6788-7230>
- Víctor M. Rivilla <https://orcid.org/0000-0002-2887-5859>
- Serena Viti <https://orcid.org/0000-0001-8504-8844>
- Yoshimasa Watanabe <https://orcid.org/0000-0002-9668-3592>
- Paul P. van der Werf <https://orcid.org/0000-0001-5434-5942>
- Yuki Yoshimura <https://orcid.org/0000-0002-1413-1963>

References

- Aladro, R., Martín, S., Riquelme, D., et al. 2015, *A&A*, **579**, A101
- Ando, R., Nakanishi, K., Kohno, K., et al. 2017, *ApJ*, **849**, 81
- Astropy Collaboration, Price-Whelan, A. M., Sipőcz, B. M., et al. 2018, *AJ*, **156**, 123
- Astropy Collaboration, Robitaille, T. P., Tollerud, E. J., et al. 2013, *A&A*, **558**, A33
- Behrens, E., Mangum, J. G., Holdship, J., et al. 2022, *ApJ*, **939**, 119
- Bellochi, E., Martín-Pintado, J., Rico-Villas, F., Martín, S., & Jiménez-Serra, I. 2023, *MNRAS*, **519**, L68
- Bendo, G. J., Beswick, R. J., D'Cruze, M. J., et al. 2015, *MNRAS*, **450**, L80
- Böker, T., Falcón-Barroso, J., Schinnerer, E., Knapen, J. H., & Ryder, S. 2008, *AJ*, **135**, 479
- Bolatto, A. D., Warren, S. R., Leroy, A. K., et al. 2013, *Natur*, **499**, 450
- Bouvier, M., Viti, S., Behrens, E., et al. 2024, *A&A*, submitted
- Butterworth, J., Viti, S., & Van der Werf, P. P. 2024, *A&A*, in press, (arXiv:2402.10721)
- Cernicharo, J., Agúndez, M., Cabezas, C., et al. 2022, *A&A*, **657**, L16
- Chidac, C. 2020, PhD thesis, Rheinische Friedrich Wilhelms University of Bonn
- Churchwell, E., Wood, D., Myers, P. C., & Myers, R. V. 1986, *ApJ*, **305**, 405
- Costagliola, F., Aalto, S., Rodriguez, M. I., et al. 2011, *A&A*, **528**, A30
- Costagliola, F., Sakamoto, K., Müller, S., et al. 2015, *A&A*, **582**, A91
- Das, M., Anantharamaiah, K. R., & Yun, M. S. 2001, *ApJ*, **549**, 896
- Fontani, F., Colzi, L., Redaelli, E., Sipilä, O., & Caselli, P. 2021, *A&A*, **651**, A94
- Fukushima, H., & Yajima, H. 2021, *MNRAS*, **506**, 5512
- Gao, Y., & Solomon, P. M. 2004, *ApJ*, **606**, 271
- García-Burillo, S., Viti, S., Combes, F., et al. 2017, *A&A*, **608**, A56
- Gorski, M. D., Aalto, S., König, S., et al. 2023, *A&A*, **670**, A70
- Gratier, P., Bron, E., Gerin, M., et al. 2017, *A&A*, **599**, A100
- Grudić, M. Y., Hopkins, P. F., Faucher-Giguère, C.-A., et al. 2018, *MNRAS*, **475**, 3511
- Haasler, D., Rivilla, V. M., Martín, S., et al. 2022, *A&A*, **659**, A158
- Harada, N., Martín, S., Mangum, J. G., et al. 2021, *ApJ*, **923**, 24
- Harada, N., Martín, S., Mangum, J. G., et al. 2022, *ApJ*, **938**, 80
- Harada, N., Sakamoto, K., Martín, S., et al. 2018, *ApJ*, **855**, 49
- Harada, N., Sakamoto, K., Martín, S., et al. 2019, *ApJ*, **884**, 100
- Henkel, C., Mühlé, S., Bendo, G., et al. 2018, *A&A*, **615**, A155
- Holdship, J., Mangum, J. G., Viti, S., et al. 2022, *ApJ*, **931**, 89
- Holdship, J., Viti, S., Martín, S., et al. 2021, *A&A*, **654**, A55
- Huang, K. Y., Viti, S., Holdship, J., et al. 2023, *A&A*, **675**, 151
- Humire, P. K., Henkel, C., Hernández-Gómez, A., et al. 2022, *A&A*, **663**, A33
- Jolliffe, I. T. 2002, Principal Component Analysis (New York: Springer)
- Kauffmann, J., Goldsmith, P. F., Melnick, G., et al. 2017, *A&A*, **605**, L5
- Kennicutt, R. C., Jr. 1998, *ApJ*, **498**, 541

- Krieger, N., Bolatto, A. D., Leroy, A. K., et al. 2020, *ApJ*, **897**, 176
- Krieger, N., Bolatto, A. D., Walter, F., et al. 2019, *ApJ*, **881**, 43
- Leroy, A. K., Bolatto, A. D., Ostriker, E. C., et al. 2015, *ApJ*, **801**, 25
- Leroy, A. K., Bolatto, A. D., Ostriker, E. C., et al. 2018, *ApJ*, **869**, 126
- Levy, R. C., Bolatto, A. D., Leroy, A. K., et al. 2021, *ApJ*, **912**, 4
- Levy, R. C., Bolatto, A. D., Leroy, A. K., et al. 2022, *ApJ*, **935**, 19
- Liszt, H. S., & Turner, B. E. 1978, *ApJL*, **224**, L73
- Lupton, R., Blanton, M. R., Fekete, G., et al. 2004, *PASP*, **116**, 133
- MacQueen, J. 1967, in Proc. Fifth Berkeley Symp. on Mathematical Statistics and Probability, ed. L. M. Le Cam & J. Neyman (Berkeley, CA: Univ. California Press), 281
- Martín, S., Kohno, K., Izumi, T., et al. 2015, *A&A*, **573**, A116
- Martín, S., Krips, M., Martín-Pintado, J., et al. 2011, *A&A*, **527**, A36
- Martín, S., Mangum, J. G., Harada, N., et al. 2021, *A&A*, **656**, A46
- Martín, S., Martín-Pintado, J., Blanco-Sánchez, C., et al. 2019, *A&A*, **631**, A159
- Martín, S., Martín-Pintado, J., & Viti, S. 2009, *ApJ*, **706**, 1323
- Martín, S., Mauersberger, R., Martín-Pintado, J., García-Burillo, S., & Henkel, C. 2003, *A&A*, **411**, L465
- Martín, S., Mauersberger, R., Martín-Pintado, J., Henkel, C., & García-Burillo, S. 2006, *ApJS*, **164**, 450
- McMullin, J. P., Waters, B., Schiebel, D., Young, W., & Golap, K. 2007, in ASP Conf. Ser. 376, Astronomical Data Analysis Software and Systems XVI, ed. R. A. Shaw, F. Hill, & D. J. Bell (San Francisco, CA: ASP), **127**
- Meier, D. S., & Turner, J. L. 2005, *ApJ*, **618**, 259
- Meier, D. S., & Turner, J. L. 2012, *ApJ*, **755**, 104
- Meier, D. S., Walter, F., Bolatto, A. D., et al. 2015, *ApJ*, **801**, 63
- Mills, E. A. C., Gorski, M., Emig, K. L., et al. 2021, *ApJ*, **919**, 105
- Müller, H. S. P., Schlöder, F., Stutzki, J., & Winnewisser, G. 2005, *JMoSt*, **742**, 215
- Müller, H. S. P., Thorwirth, S., Roth, D. A., & Winnewisser, G. 2001, *A&A*, **370**, L49
- Müller, S., Beelen, A., Black, J. H., et al. 2013, *A&A*, **551**, A109
- Nakajima, T., Takano, S., Kohno, K., Harada, N., & Herbst, E. 2018, *PASJ*, **70**, 7
- Nishimura, Y., Watanabe, Y., Harada, N., et al. 2017, *ApJ*, **848**, 17
- Pearson, K. 1901, *PMag*, **2**, 559
- Pedregosa, F., Varoquaux, G., Gramfort, A., et al. 2011, *JMLR*, **12**, 2825
- Pety, J., Gratier, P., Guzmán, V., et al. 2012, *A&A*, **548**, A68
- Pety, J., Guzmán, V. V., Orkisz, J. H., et al. 2017, *A&A*, **599**, A98
- Quan, D., Herbst, E., Osamura, Y., & Roueff, E. 2010, *ApJ*, **725**, 2101
- Rekola, R., Richer, M. G., McCall, M. L., et al. 2005, *MNRAS*, **361**, 330
- Rico-Villas, F., Martín-Pintado, J., González-Alfonso, E., Martín, S., & Rivilla, V. M. 2020, *MNRAS*, **491**, 4573
- Saito, T., Takano, S., Harada, N., et al. 2022, *ApJ*, **935**, 155
- Sakamoto, K., Mao, R.-Q., Matsushita, S., et al. 2011, *ApJ*, **735**, 19
- Sakamoto, K., Martín, S., Wilner, D. J., et al. 2021, *ApJ*, **923**, 240
- Schinnerer, E., Hughes, A., Leroy, A., et al. 2019, *ApJ*, **887**, 49
- Shirley, Y. L. 2015, *PASP*, **127**, 299
- Sorai, K., Nakai, N., Kuno, N., Nishiyama, K., & Hasegawa, T. 2000, *PASJ*, **52**, 785
- Suutarinen, A. N., Kristensen, L. E., Mottram, J. C., Fraser, H. J., & van Dishoeck, E. F. 2014, *MNRAS*, **440**, 1844
- Tafalla, M., Usero, A., & Hacar, A. 2021, *A&A*, **646**, A97
- Takano, S., Nakajima, T., & Kohno, K. 2019, *PASJ*, **71**, S20
- Takano, S., Nakajima, T., Kohno, K., et al. 2014, *PASJ*, **66**, 75
- Takeuchi, T. T., Yata, K., Aoshima, M., et al. 2022, arXiv:2203.04535
- Tanaka, K., Mangum, J., Viti, S., et al. 2024, *ApJ*, **961**, 18
- Tanaka, K., Nagai, M., Kamegai, K., Iino, T., & Sakai, T. 2018, *ApJS*, **236**, 40
- Taniguchi, K., Tanaka, K. E. I., Zhang, Y., et al. 2022, *ApJ*, **931**, 99
- Tercero, B., Cernicharo, J., Cuadrado, S., de Vicente, P., & Guélin, M. 2020, *A&A*, **636**, L7
- Thaddeus, P., Guelin, M., & Linke, R. A. 1981, *ApJL*, **246**, L41
- Turner, B. E. 1985, *ApJ*, **299**, 312
- Turner, J. L., & Ho, P. T. P. 1985, *ApJ*, **299**, L77
- Ulvestad, J. S., & Antonucci, R. R. J. 1997, *ApJ*, **488**, 621
- Ungerechts, H., Bergin, E. A., Goldsmith, P. F., et al. 1997, *ApJ*, **482**, 245
- Veilleux, S., Maiolino, R., Bolatto, A. D., & Aalto, S. 2020, *A&ARv*, **28**, 2
- Walter, F., Bolatto, A. D., Leroy, A. K., et al. 2017, *ApJ*, **835**, 265
- Watanabe, Y., Nishimura, Y., Harada, N., et al. 2017, *ApJ*, **845**, 116
- Wernli, M., Wiesenfeld, L., Faure, A., & Valiron, P. 2007, *A&A*, **464**, 1147
- Wu, J., Evans, N. J., II, Shirley, Y. L., & Knez, C. 2010, *ApJS*, **188**, 313